Low–Mach number asymptotic analysis of fluid–structure-interaction (FSI) pressure waves inside an elastic tube

A. Bayle, Franck Plouraboué

Low–Mach number asymptotic analysis of fluid-structure-interaction (FSI) pressure waves inside an elastic tube

A. Bayle, F. Plouraboué

Institut de Mécanique des Fluides de Toulouse, IMFT, Université de Toulouse, CNRS, Toulouse, France

Abstract

We consider the pressure wave having velocity c_p inside an elastic tube of internal radius R_0, thickness e, length L, shear modulus $\mathcal{G}$ and density ρ_{s_0}, filled with a fluid with kinematic viscosity ν_f. We theoretically analyze the fluid–structure coupling between: (i) the elastic sheath, (ii) the fluid boundary layer, and (iii) the core acoustic pressure and velocity fields. Our analysis provides an asymptotic derivation of the fluid–structure–interactions (FSI) model that recovers known pulse–wave velocities and provides a new theoretical prediction for the exponential time decay of the wave longitudinal attenuation envelope. Taking advantage of highly distinct time–scales between the viscous radial diffusion $\tau_d = R_0^2/\nu_f$ compared with wave–convective time $\tau_c = L/c_p$ as well as the elastic relaxation time $\tau_e = e\sqrt{\rho_s/\mathcal{G}}$, such that $\tau_e \sim \tau_c \ll \tau_d$ we perform a two time–scale asymptotic analysis based on a small parameter $\delta = \sqrt{\tau_c/\tau_d}$. Said parameter is obtained by balancing the momentum acceleration and the viscous damping rate in the inner unsteady boundary layer, the thickness of which being δR_0. The resulting asymptotic sequence provides a unique consistent scaling for solid deformation and velocity fields, with the secularity condition associated with the leading-order slow-time scale envelope attenuation obtained by extending the analysis to investigate the first-order corrections.

On the one hand our approach reconciles both predictions for the precursive elastic wave and the pulse velocities obtained when considering solid deformation only, and, on the other hand, predictions for the longitudinal attenuation

resulting from the effect of boundary layers only. Our analysis also permits the derivation of a new convoluted model for the wall shear stress, which is (FSI)–consistent. The theoretical results are successfully compared with experimental measurements.
Keywords: , fluid–structure–interactions, acoustic waves in pipes, multiple time–scale analysis, asymptotic matching, water hammer, blood hammer, Lamé–Clapeyron equations

1. Introduction

The propagation of water–hammer pulsed pressure waves is a well–known, long–standing topic that arises in various practical contexts, such as hydraulic pipes. Examples include gas and petroleum transmission lines [1, 2, 3, 4, 5, 6], blood vessels [7, 8], fluidic system response [9, 10] compressor dynamics and hydroelectric power generation, etc... Reviews of this topic are available from [11, 12, 13, 14, 15], the contents of which are not repeated here. Water–hammer waves are associated with the following three classes of coupling effects: (i) Poisson coupling, (ii) friction coupling, (iii) junction coupling.

Poisson coupling is related to the pipe's successive radial expansion–compression phases (also called pipe's breathing) induced by the fluid overpressure propagation in the solid. This not only generates hoop stress in the tube, but also axial deformation through Poisson's modulus ν_s, thus producing elastic longitudinal compression waves or so–called precursor waves, which have been analyzed by [16, 17, 18, 19, 20] for thin–walled pipes and by [21, 22] for thick–walled pipes. These contributions leads to the derivation of four fluid–structure–interactions (FSI) equations for hyperbolic coupled systems [14]. Additional vibrating modes may occur depending on the considered tube's degree of freedom (e.g. rolling, yawing and swaying; [23, 15]), but these are not consider in this analysis.

When, one considers, in addition to Poisson coupling the influence of junction couplings, i.e. couplings from dead–end tube connections, these four–(FSI) equations are most often solved numerically and more rarely in the frequency

domain. The numerical methods are mainly based on the method of characteristics (MOC) in [24, 25, 26, 27, 28], whilst frequency domain analyses are performed using the transfer matrix method (TMM) framework [29, 30, 31], which displays Fourier peaks associated with the response of specific discrete modes. Time domain solutions of these four–(FSI) equations in simple configurations [32, 33] display a discrete but infinite set of intrinsic vibrating modes that have distinct and specific wavelengths and frequencies (i.e. a discrete spectrum). On the contrary, when considering infinite, or semi–infinite tubes, then ignoring the junction coupling effects, the continuous propagation of modes with any wavelength and frequency arises (i.e. a continuum spectrum as in [34, 35, 9, 10]).

As with Poisson coupling, friction coupling occurs over the entire length of a pipe from boundary layer dissipation within the fluid. The transient response of boundary layer, i.e. the near–wall fluid velocity response to a transient solicitation, was studied by [36], who considered an axial momentum conservation equation that resulted in a history–dependent shear rate with a time–convolution with the longitudinal pressure gradient. [36] also provided an analytical approximation of the convolution kernel. Zielke's model exhibited excellent agreement with experiments by [37, 38]. This fluid friction influence was analyzed in greater depth within a boundary layer theory moving at wave–front speed by [39, 40, 41, 42], who matched it with the outer fluid region. Furthermore, realizing that the time scale for viscous diffusion within the boundary layer is comparable with the propagation time of the wave, [43, 41, 42] have proposed a two–time scale asymptotic expansion. This led to the deduction of a slow–time, mode–dependent exponentially amplitude decay of the pulse pressure wave. This approach accounts for the long–time damping of a liquid–filled pipe system.

This overview of various contributions illustrates that although many studies have been performed on the topic, which have provided deep insights into this complex subject as well as reliable predictions compared with measurements, no global and rational theoretical framework exists for re–conciliating the various aspects of water–hammer wave propagation.

This paper presents a systematic asymptotic analysis of classical water–hammer pulsed pressure waves for an elastic tube that exploits the following assumptions: (a) small displacements, (b) weak fluid compressibility, (c) long–wavelengths and (d) a thin viscous boundary layer. The novelty of this study lies into providing a comprehensive and exhaustive analysis of the various couplings established from first principles, using a dimensionless formulation associated with a complete set of dimensionless numbers. Some of them are small, and their relative smallness is clarified.

The aforementioned four assumptions (a–b–c and d) are associated with the following four dimensionless parameters: the tube aspect ratio ϵ, the tube thickness to radius ratio α, the pulse wave Mach number $\mathcal{M}$ and the inverse of the pulse wave–speed Reynolds number $1/Re_p$. From these, a useful dimensionless parameter $\delta = 1/\sqrt{\epsilon Re_p}$ (which is also the square root of the convective to diffusive time–scale as well as the dimensionless boundary layer thickness) is defined, the relative smallness of which is of special interest in our analysis (i.e. $\delta^2 \gg \mathcal{M}$, $\delta \gg \epsilon^2$, $\delta \gg \alpha\mathcal{M}$, and $1 \gg \epsilon \gg \alpha\mathcal{M}$). As discussed in many studies (e.g. ([19, 10, 22])), the correction to the long–wavelength approximation is $O(\epsilon^2)$. During the course of the derivation this long–wavelength assumption will be seen to also imply negligible radial acceleration of the pipe breathing motion, as well as radially uniform longitudinal displacement inside the solid similar to a planar elastic wave propagation at leading–order. Also, this derivation will show the conditions for which *unsteady* boundary layer effects dominate over *steady* ones, leading to a complete decoupling between the wave propagation from the pre-existing steady flow. This leading–order planar elastic wave in the solid is coupled with the fluid pressure wave, leading to a set of two coupled propagating waves with two specific propagating velocities, equivalently described by the four aforementioned (FSI) equations. The solution to these leading–order propagating wave problems can be found analytically using an orthogonal base decomposition, as in the study of [33]. It depends on the applied boundary conditions from the vibrating (FSI) up to some slowly varying (undefined at this order) amplitudes, which are specific for each mode. Conducting an eval-

uation of the corrections to these leading–order solutions while considering a two–time–scale asymptotic analysis leads to determining the amplitude decay, which depends on viscous effects that arise in boundary layers. Hence, the presented derivation is not only interesting for the asymptotic derivation of the four–(FSI) equations associated with fluid pressure/solid elastic wave coupled propagation. It also permits to determine how viscous effects damp this propagation, generalizing [41, 42] from including (FSI) effects. Although applicable to general junction coupling conditions, the hereby derived (FSI) damping is explicitly provided for a specific set of boundary conditions and compared with experimental observations.

The remainder of this paper is organized as follows. Section §2 describes the fundamental dimensionless equations in the three considered distinct regions, namely the fluid bulk, fluid boundary layer, and elastic solid. A consistency condition for small elastic deformation is found, which motivates a more systematic analysis of the asymptotic framework developed in §3. Through defining the various corrections associated with three small parameters, namely the dimensionless thickness of the viscous boundary layer, Mach number, and tube aspect ratio, a systematic asymptotic analysis is presented in §3 and coupled with a two–time scale one. Section §3 involves the derivation of coupled (FSI) leading– and first–order corrections associated with the small parameter of the dimensionless viscous boundary layer thickness δ, as well as the resolution of their coupling using asymptotic matching. The analysis finally permits the establishment of the (FSI) wave model with two–coupled propagative equations with additional dissipative terms included as corrections. In §4 the (FSI) waves model is solved (both at leading– and first–orders) so as to find the secularity condition for the slow–time amplitude of the leading–order, thus providing the (FSI) wave system's attenuation. Finally §5 compares the proposed low–Mach theory with experimental measurements, considering longitudinal damping predictions in particular.

2. Fundamental equations

A pressure wave having typical velocity c_p propagating on top of a non-zero steady flow, inside a fluid-filled elastic-walled tube is considered. Dimensional fields will be denoted with the superscript *.

2.1. Definitions overview and problem setting

We consider an initially circular tube of length L, inner radius R_0, wall thickness e, density ρ_{s_0}, Young's modulus E and Poisson's ratio ν_s. The tube is supposed elastic and isothermal. It is filled with a Newtonian, weakly compressible, and isothermal fluid, having possibly varying density ρ_f^*, isentropic bulk modulus $\mathcal{K}_f$, kinematic viscosity ν_f, dynamic viscosity μ_f, volume viscosity λ_f, and the viscosity ratio $\Gamma = \lambda_f/\mu_f \sim O(1)$. The fluid is supposed initially flowing at the velocity W_{st}^*, under the steady–state pressure P_{st}^*, condition. The constant fluid reference density is denoted ρ_{f_0} and gravity effects are neglected. The dimensionless tube thickness and aspect ratio are defined as

$$\alpha = \frac{e}{R_0}, \quad \& \quad \epsilon = \frac{R_0}{L} \ll 1. \tag{1}$$

Thereafter, α is considered to be an order one quantity, but the thin–wall limit $\alpha \ll 1$ is sometimes discussed in comparison with thin–shell theory. A more precise condition for large α values will be discussed in section 3. In the following, inner region refers to the near–wall viscous boundary layer whereas outer region stands for the core inviscid flow one. The dimensionless thickness of the boundary layer is referred to as δ, being a central small parameter of the study. Capital letters refer to outer fields in the fluid core, while lowercase letters are associated with the inner boundary layer. The fluid–filled pipe system is axisymmetric and described by cylindrical radial/axial coordinates (r, z), having basis vectors $(\mathbf{e}_r, \mathbf{e}_z)$, and dimensionless counterparts $(R = r/R_0, Z = z/L)$. A dimensionless *fast* time $\tau = c_p\, t/L$, is build upon the wave speed advective time-scale L/c_p. As the pressure waves propagate, the elastic tube deforms and solid material points are transported by solid displacement vector

$$\boldsymbol{\xi}^*(r, z, t) = \xi^*(r, z, t)\mathbf{e}_r + \zeta^*(r, z, t)\mathbf{e}_z, \tag{2}$$

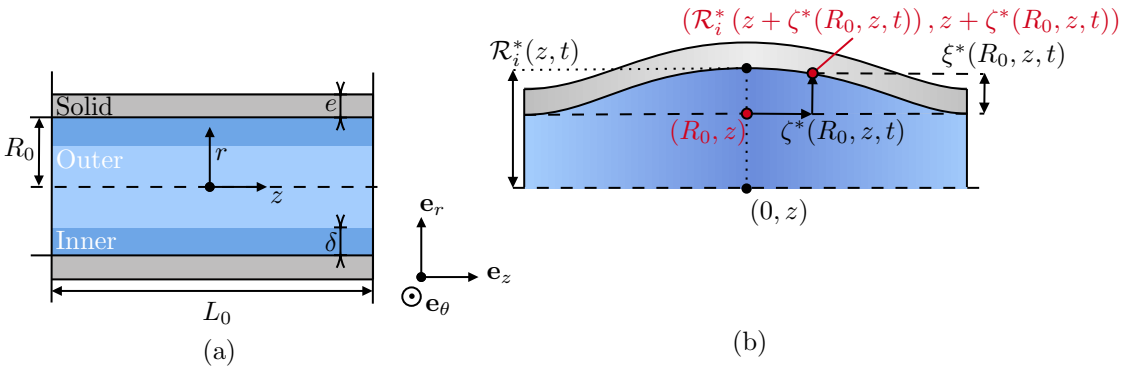

Figure 1: (a) Geometrical and coordinate variables. (b) Tube's deformation, i.e. pipe *breathing*, induced by the local fluid over-pressure. The initial material point vector (R_0, z), is transported by the solid displacement vector (ξ^*, ζ^*)

where (ξ^*, ζ^*) are the radial and axial solid displacement components, respectively. We then define $(\mathbf{n}_i, \mathbf{n}_o)$ and $(\mathbf{t}_i, \mathbf{t}_o)$ as the unit normal and tangential vectors associated with the inner $\mathcal{R}_i^*(z,t) = R_0\mathcal{R}_i(Z,\tau)$ and outer, $\mathcal{R}_o^*(z,t) = R_0\mathcal{R}_o(Z,\tau)$, tube radius. The tube inner radius depends on the displacement components as

$$\mathcal{R}_i^*(z+\zeta^*(R_0,z,t),t) = R_0 + \xi^*(R_0,z,t). \tag{3}$$

All variables are depicted in Figure 1. The outer/inner fluid pressure P_f^*/p_f^*, axial velocity W_f^*/w_f^*, and radial velocity U_f^*/u_f^*, are splitted into steady, denoted with subscript st, and unsteady components (without subscript) following the classical acoustic approach, [44]

$$\begin{aligned} P_f^* &= P^*(r,z,t) + P_{st}^*(r,z), & p_f^* &= p^*(r,z,t) + p_{st}^*(r,z), \\ W_f^* &= W^*(r,z,t) + W_{st}(r,z), & w_f^* &= w^*(r,z,t) + w_{st}^*(r,z), \\ U_f^* &= U^*(r,z,t), & u_f^* &= u^*(r,z,t). \end{aligned} \tag{4}$$

As the steady–state is assumed unidirectional, the outer/inner radial velocity components U_f^*/u_f^*, are only unsteady. Finally, the fluid inner stress tensor, unsteady shear stress and unsteady wall shear rate are defined, following a

Newtonian rheology, as $\boldsymbol{\sigma}_f^* = \boldsymbol{\sigma}_{st}^* + \boldsymbol{\sigma}^*$, τ_f^*, τ_w^*

$$\boldsymbol{\sigma}_{st}^* = (-P_{st}^* + \lambda_f \partial_z W_{st}^*)\,\mathbf{I} + \mu_f \begin{pmatrix} 0 & \cdots & \partial_r W_{st}^* \\ \cdots & 0 & \cdots \\ \partial_r W_{st}^* & \cdots & 0 \end{pmatrix}, \tag{5}$$

$$\boldsymbol{\sigma}^* = \left(-p^* + \lambda_f \left[\frac{\partial_r}{r}(ru^*) + \partial_z w^*\right]\right)\mathbf{I} + 2\mu_f \begin{pmatrix} \partial_r u^* & \cdots & \frac{\partial_r w^* + \partial_z u^*}{2} \\ \cdots & \frac{u^*}{r} & \cdots \\ \frac{\partial_r w^* + \partial_z u^*}{2} & \cdots & \partial_z w^* \end{pmatrix} \tag{6}$$

$$\tau_f^* = -\rho_{f_0} \nu_f \partial_r w^*, \quad \& \quad \tau_w^* = \tau_f^*\left(\mathcal{R}_i^*, z, t\right). \tag{7}$$

2.2. Dimensionless numbers set and hypothesis framework

When an unsteady fluid velocity perturbation of magnitude W_0, is applied to a liquid–filled pipe system, an acoustic pressure pulse with velocity c_p then propagate, the magnitude of which denoted ΔP_0 is given by [5]'s law

$$\Delta P_0 = \rho_{f_0} c_p W_0. \tag{8}$$

The longitudinal wave speed propagation in the fluid, c_p, and in the solid, c_s, has been provided by [14, 22]

$$c_0 = \sqrt{\frac{\mathcal{K}_f}{\rho_{f_0}}}, \quad \& \quad c_p = \frac{c_0}{\sqrt{1 + \frac{2\mathcal{K}_f}{\alpha E}\left(\frac{2(1-\nu_s^2)}{2+\alpha} + \alpha(1+\nu_s)\right)}}, \quad \& \quad c_s = \sqrt{\frac{E}{\rho_{s_0}}}, \tag{9}$$

where c_0 is the speed of sound of acoustic waves into an infinite fluid and α is the dimensionless tube thickness provided in (1). The ratios of these speeds are denoted

$$\mathcal{C} = \frac{c_0}{c_p}, \quad \& \quad \mathcal{C}_s = \frac{c_s}{c_p}. \tag{10}$$

Since the elastic–walled tube offers resistance to the fluid overpressure, two dimensionless numbers (similar to Cauchy's number) are introduced to compare the wave dynamic pressure, i.e. $\rho_{f_0} c_p^2$, with the tube elastic resistance

$$\mathcal{C}_{\mathcal{G}} = \frac{\rho_{f_0} c_p^2}{\mathcal{G}} \equiv \frac{2\rho_{f_0} c_p^2 (1+\nu_s)}{E}, \quad \& \quad \mathcal{C}_{\lambda_s} = \frac{\rho_{f_0} c_p^2}{\lambda_s} \equiv \frac{\mathcal{C}_{\mathcal{G}}(1-2\nu_s)}{2\nu_s}, \tag{11}$$

where

$$\mathcal{G} = \frac{E}{2(1+\nu_s)}, \quad \& \quad \lambda_s = \frac{\nu_s E}{(1+\nu_s)(1-2\nu_s)}, \tag{12}$$

are the solid shear modulus and the second Lamé-Clapeyron coefficient, respectively. The overpressure wave velocity c_p, given in (9), is thus a corrective formulation of c_0 due to the tube elastic constraints. By introducing parameter

$$\chi = \frac{2\mathcal{K}_f}{\alpha E \mathcal{C}^2}\left(\frac{2(1-\nu_s^2)}{2+\alpha} + \alpha(1+\nu_s)\right) \equiv \frac{2\nu_s \mathcal{C}_{\lambda_s} + (1+\alpha)^2 \mathcal{C}_{\mathcal{G}}}{\alpha(2+\alpha)}, \tag{13}$$

the pulse wave speed (9) becomes

$$c_p^2 = \frac{c_0^2}{1+\chi\mathcal{C}^2}, \tag{14}$$

where $1+\chi\mathcal{C}^2$ is a corrective fluid pulse–wave speed factor. Regarding the definition of c_p in (9), it is relevant to highlight that $\mathcal{C}^2 > 1$ which follows from $c_p < c_0$ [4, 16, 21, 45]. The (FSI) behavior is finally impacted by the fluid to solid density ratio, [14]

$$\mathcal{D} = \frac{\rho_{f_0}}{\rho_{s_0}}. \tag{15}$$

Finally, a set of dimensionless parameters associated with boundary layer thickness δ, Reynolds number Re, pulsed Reynolds number Re_p and Mach number $\mathcal{M}$ is introduced yielding to

$$Re_p = \frac{c_p R_0}{\nu_f} \gg 1, \qquad Re = \frac{W_0 R_0}{\nu_f} = \mathcal{M} Re_p, \tag{16}$$

$$\delta^2 = \frac{\nu_f L}{c_p R_0^2} = \frac{1}{\epsilon Re_p} \ll 1, \qquad \mathcal{M} = \frac{W_0}{c_p} \ll 1. \tag{17}$$

Low–Mach number [25, 27], along with the long–wavelength, i.e. $\epsilon \ll 1$ [46, 17, 19, 22], asymptotic analyses are simultaneously used in the forthcoming. The following asymptotic framework is assumed, for which boundary layer dissipation effects are dominant compare to compressible and radial solid inertial ones

$$\delta^2 \gg \mathcal{M} > \frac{\mathcal{M}}{\mathcal{C}^2}, \qquad \delta \gg \epsilon^2, \qquad \delta \gg \alpha\mathcal{M}, \qquad 1 \gg \epsilon \gg \alpha\mathcal{M}. \tag{18}$$

The hereby asymptotic ordering is in depth discussed and justified in §3, the relevance of which will be shown to provide an asymptotic derivation for known

four–(FSI) equations model [22]. Hence parameter δ being the ratio of viscosity diffusion time–scale ν_f/R_0^2, to advection one L/c_p, is the cornerstone small parameter of the proposed two–times–scale asymptotic analysis [47, 41]. It will be shown later-on that the physical mechanisms behind the chosen asymptotic framework (18) lies in (i) negligible steady-flow boundary-layer effects compared to unsteady ones (ii) dominating radial diffusion transport of viscous shear (iii) FSI coupling in the boundary-layer arising from wall-shear stress. It is important to stress that the asymptotic framework validity only depends of dimensionless parameters relative values fulfilling condition (18) (and not their intrinsic value) provided these parameters being large or small as stated in (16) and (17). In the inner region a rescaled radial coordinates y, scaling as $O\left(1/\delta\right)$, is set up

$$y = \frac{1-R}{\delta}, \tag{19}$$

to account for the influence of the radial gradient contributions in the boundary layer. The fluid and solid constitutive, dimensionless, equations are thereafter derived.

2.3. Dimensionless Navier–Stokes equations

The unsteady pressure component P^*, is scaled upon [5]'s overpressure (8), whereas the unsteady fluid axial velocity is scaled on the steady–state one, i.e. W_0. In the radial direction, the unsteady fluid velocity is assumed ϵ smaller than the axial one, resulting from long–wavelength assumption, so that

$$P^*_{st} = \rho_{f_0} W_0^2 P_{st}(R,Z), \qquad W^*_{st} = W_0 W_{st}(R,Z), \tag{20}$$

$$P^* = \rho_{f_0} c_p W_0 P(R,Z,\tau), \qquad p^* = \rho_{f_0} c_p W_0 p(y,Z,\tau), \tag{21}$$

$$W^* = W_0 W(R,Z,\tau), \qquad w^* = W_0 w(y,Z,\tau), \tag{22}$$

$$U^* = \epsilon W_0 U(R,Z,\tau), \qquad u^* = \epsilon W_0 u(y,Z,\tau), \tag{23}$$

where unsteady outer/inner pressure and velocity field components are identically scaled to match at the boundary layer interface. Relevant at the fluid/solid interface, i.e. inside the boundary layer, the unsteady wall shear stress and wall

shear rate responses, defined in (5)–(7), are scaled as follows

$$\tau_f^* = -\frac{\rho_{f_0}\nu_f W_0}{\delta R_0}\tau_f(y,Z,\tau), \qquad \tau_f = \partial_y w(y,Z,\tau), \tag{24}$$

$$\boldsymbol{\sigma}^* = \rho_{f_0} c_p W_0 \boldsymbol{\sigma}, \qquad \boldsymbol{\sigma}_{st}^* = \rho_{f_0} W_0^2 \boldsymbol{\sigma}_{st}, \tag{25}$$

130

$$\boldsymbol{\sigma}_{st} = \left(-P_{st} + \Gamma\frac{(\epsilon\delta)^2}{\mathcal{M}}\partial_Z W_{st}\right)\mathbf{I} + \frac{\epsilon\delta}{\mathcal{M}}\begin{pmatrix} 0 & \cdots & -\partial_y W_{st} \\ \cdots & 0 & \cdots \\ -\partial_y W_{st} & \cdots & \epsilon\delta\partial_Z W_{st}\end{pmatrix}, \tag{26}$$

$$\boldsymbol{\sigma} = \left(-p + \Gamma(\epsilon\delta)^2\left(-\frac{\partial_y\left[(1-\delta y)\,u\right]}{\delta(1-\delta y)} + \partial_Z w\right)\right)\mathbf{I} + \epsilon\delta\begin{pmatrix} -2\epsilon\partial_y u & \cdots & -\partial_y w + \epsilon^2\partial_Z u \\ \cdots & 2\epsilon\delta\frac{u}{1-\delta y} & \cdots \\ -\partial_y w + \epsilon^2\partial_Z u & \cdots & 2\epsilon\delta\partial_Z w\end{pmatrix} \tag{27}$$

Using the fluid isentropic compression law, i.e. $\partial_{P_f^*}\left(\rho_f^*\right) = \rho_f^*/\mathcal{K}_f$, the fluid density is subjected to pressure variations following

$$\rho_f^*(r,z,t) = \rho_{f_0} e^{\frac{P_f^*(r,z,t)}{\mathcal{K}_f}} = \rho_{f_0} e^{\frac{P^*(r,z,t)+P_{st}^*(r,z)}{\mathcal{K}_f}}, \tag{28}$$

so that by introducing the dimensionless density $\rho_f = \rho_f^*/\rho_{f_0}$, and regarding the scalings provided in (20)–(23), it yields to

$$\left[1, \boldsymbol{\nabla}, \partial_\tau\right]\rho_f = e^{\frac{\mathcal{M}}{\mathcal{C}^2}(P+\mathcal{M}P_{st})}\left[1, \frac{\mathcal{M}}{\mathcal{C}^2}\boldsymbol{\nabla}\left(P+\mathcal{M}P_{st}\right), \frac{\mathcal{M}}{\mathcal{C}^2}\partial_\tau P\right], \tag{29}$$

with $\boldsymbol{\nabla}$ the dimensionless Nabla operator, $\mathcal{C}^2$ defines in (10) and $\mathcal{M}/\mathcal{C}^2 \ll 1$. Obviously, in the inner region (29) holds from replacing P by the inner pressure p. The Navier–Stokes equations, which follows from fluid mass and momentum conservations, yield

$$\left(\partial_t + W_f^*\partial_z + U^*\partial_r\right)\rho_f^* + \rho_f^*\left(\partial_z W_f^* + \frac{1}{r}\partial_r\left(r\partial_r U^*\right)\right) = 0, \tag{30}$$

$$\begin{aligned}\rho_f^*\left(\partial_t + W_f^*\partial_z + U^*\partial_r\right)W_f^* &= -\partial_z P_f^* \\ &+ \rho_{f_0}\nu_f\left(\left(1+\Gamma\right)\partial_z\left[\partial_z W_f^* + \frac{\partial_r}{r}\left(rU^*\right)\right] + \left(\frac{\partial_r}{r}\left(r\partial_r\right) + \partial_z^2\right)W_f^*\right),\end{aligned} \tag{31}$$

$$\begin{aligned}\rho_f^*\left(\partial_t + W_f^*\partial_z + U^*\partial_r\right)U^* &= -\partial_r P_f^* \\ &+ \rho_{f_0}\nu_f\left(\left(1+\Gamma\right)\partial_r\left[\partial_z W_f^* + \frac{\partial_r}{r}\left(rU^*\right)\right] + \left(\frac{\partial_r}{r}\left(r\partial_r\right) - \frac{1}{r^2} + \partial_z^2\right)U^*\right),\end{aligned} \tag{32}$$

131 and are now investigated though dimensionless variables.

132 *2.3.1. Dimensionless steady–state fluid equations*

At steady–state, the fluid unsteady components vanish in (30)–(32), it thus yields

$$\left(\frac{\mathcal{M}}{\mathcal{C}}\right)^2 W_{st}\partial_Z P_{st} + \partial_Z W_{st} = 0, \tag{33}$$

$$\mathcal{M}e^{\left(\frac{\mathcal{M}}{\mathcal{C}}\right)^2 P_{st}} W_{st}\partial_Z W_{st} = -\mathcal{M}\partial_Z P_{st} + (\epsilon\delta)^2 (2+\Gamma)\partial_Z^2 W_{st} + \delta^2 \frac{\partial_R}{R}\left(R\partial_R\right) W_{st}, \tag{34}$$

$$\frac{\mathcal{M}}{\epsilon^2}\partial_R P_{st} = (1+\Gamma)\delta^2 \partial_R \partial_Z W_{st}, \tag{35}$$

133 Where $(\epsilon Re)^{-1} = \delta^2/\mathcal{M}$ have been used.

134 *2.3.2. Dimensionless unsteady bulk fluid equations*

Regarding the relations (30)–(32) but subtracting the steady–state relations (33)–(35), it follows regarding the fluid scalings (20)–(23), the outer dimensionless mass and momentum conservation equations

$$\partial_\tau P + \mathcal{M}\left(\left[W\partial_Z + U\partial_R\right](P + \mathcal{M}P_{st}) + W_{st}\partial_Z P\right) + \mathcal{C}^2\left[\partial_Z W + \frac{1}{R}\partial_R\left(RU\right)\right] = 0, \tag{36}$$

$$\begin{aligned} e^{\frac{\mathcal{M}}{\mathcal{C}^2}(P+\mathcal{M}P_{st})}&\left(\partial_\tau W + \mathcal{M}\left(\left[W\partial_Z + U\partial_R\right](W + W_{st}) + W_{st}\partial_Z W\right)\right) \\ &+ \mathcal{M}e^{\left(\frac{\mathcal{M}}{\mathcal{C}}\right)^2 P_{st}}\left(e^{\frac{\mathcal{M}}{\mathcal{C}^2}P} - 1\right) W_{st}\partial_Z W_{st} = \\ -\partial_Z P + (\epsilon\delta)^2 (1+\Gamma)\partial_Z&\left[\partial_Z W + \frac{1}{R}\partial_R\left(RU\right)\right] + \delta^2\left(\frac{\partial_R}{R}R\partial_R + \epsilon^2\partial_Z^2\right) W, \end{aligned} \tag{37}$$

$$\begin{aligned} &e^{\frac{\mathcal{M}}{\mathcal{C}^2}(P+\mathcal{M}P_{st})}\left(\partial_\tau + \mathcal{M}\left[\left(W + W_{st}\right)\partial_Z + U\partial_R\right]\right) U = -\frac{1}{\epsilon^2}\partial_R P \\ &+ \delta^2(1+\Gamma)\partial_R\left[\partial_Z W + \frac{1}{R}\partial_R\left(RU\right)\right] + \delta^2\left(\frac{\partial_R}{R}\left(R\partial_R\right) - \frac{1}{R^2} + \epsilon^2\partial_Z^2\right) U, \end{aligned} \tag{38}$$

135

136 *2.3.3. Dimensionless unsteady fluid boundary layer equations*

In the inner viscous zone, using rescaled coordinate y defined in (19) dimensionless Navier–Stokes equations are

$$\partial_\tau p + \mathcal{M}\left(\left[w\partial_Z - \frac{u}{\delta}\partial_y\right](p + \mathcal{M}P_{st}) + W_{st}\partial_Z p\right) + \mathcal{C}^2\left[\partial_Z w - \frac{1}{\delta}\frac{1}{1-\delta y}\partial_y\left((1-\delta y)u\right)\right] = 0, \tag{39}$$

$$\begin{aligned} e^{\frac{\mathcal{M}}{\mathcal{C}^2}(p+\mathcal{M}P_{st})}&\left(\partial_\tau w + \mathcal{M}\left(\left[w\partial_Z - \frac{u}{\delta}\partial_y\right](w + W_{st}) + W_{st}\partial_Z w\right)\right) \\ &+ \mathcal{M}e^{\left(\frac{\mathcal{M}}{\mathcal{C}}\right)^2 P_{st}}\left[e^{\frac{\mathcal{M}}{\mathcal{C}^2}p} - 1\right]W_{st}\partial_Z W_{st} \\ = -\partial_Z p &+ (\epsilon\delta)^2(1+\Gamma)\partial_Z\left[\partial_Z w - \frac{1}{\delta}\frac{1}{1-\delta y}\partial_y\left((1-\delta y)u\right)\right] \\ &+ \left(\frac{\partial_y}{1-\delta y}\left((1-\delta y)\partial_y\right) + (\epsilon\delta)^2\partial_Z^2\right)w, \end{aligned} \tag{40}$$

$$\begin{aligned} e^{\frac{\mathcal{M}}{\mathcal{C}^2}(p+\mathcal{M}P_{st})}&\left(\partial_\tau + \mathcal{M}\left[(w + W_{st})\partial_Z - \frac{u}{\delta}\partial_y\right]\right)u = \frac{1}{\delta\epsilon^2}\partial_y p \\ &- (1+\Gamma)\partial_y\left[\delta\partial_Z w - \frac{1}{1-\delta y}\partial_y\left((1-\delta y)u\right)\right] \\ &+ \left(\frac{\partial_y}{1-\delta y}\left((1-\delta y)\partial_y\right) - \frac{\delta^2}{(1-\delta y)^2} + (\epsilon\delta)^2\partial_Z^2\right)u. \end{aligned} \tag{41}$$

137 The fluid steady and unsteady constitutive dimensionless equations are now
138 derived, the solid dynamic is then investigated.

139 *2.4. The dimensionless Lamé-Clapeyron equations*

From the linearity of the solid elastic rheology, only the unsteady responses of strains and stresses are considered (i.e. the pre–existing steady–state stress–strain does not influence the unsteady one). Furthermore, axial fluid velocity predominance produces a very similar order of magnitude hierarchy within the solid displacement field from kinematic boundary conditions. Consequently, the dimensional unsteady solid displacement vector, $\boldsymbol{\xi}^*$ in (2), fulfills as in [48]

$$\boldsymbol{\xi}^* = \xi_0\xi\mathbf{e}_r + \frac{\xi_0}{\epsilon}\zeta\mathbf{e}_z, \tag{42}$$

with ξ_0 the solid radial displacement order of magnitude. The stress $\boldsymbol{\sigma}_s^*$, displacement $\boldsymbol{\xi}^*$, relationships is provided by Hooke's law

$$\boldsymbol{\sigma}_s^* \equiv \begin{pmatrix} \sigma_{rr}^* & \dots & \sigma_{rz}^* \\ \dots & \sigma_{\theta\theta}^* & \dots \\ \sigma_{rz}^* & \dots & \sigma_{zz}^* \end{pmatrix} = \lambda_s \left(\boldsymbol{\nabla}^* \cdot \boldsymbol{\xi}^*\right) \mathbf{I} + \mathcal{G}\left(\boldsymbol{\nabla}^* \boldsymbol{\xi}^* + \boldsymbol{\nabla}^* \boldsymbol{\xi}^{*^T}\right), \tag{43}$$

where the superscript T refers to the transpose operation and $\boldsymbol{\nabla}^*$ stands for the dimensional Nabla operator. The solid stress tensor diagonal terms are all identically scaled so as to match with the pulse overpressure, i.e. $O\left(\rho_{f_0} c_p W_0\right)$, thereby ensuring volumetric stress components of $\mathrm{Tr}\left(\boldsymbol{\sigma}_{\mathrm{s}}^*\right)$ to uniformly respond to this overpressure

$$[\sigma_{rr}^*, \sigma_{\theta\theta}^*, \sigma_{zz}^*] = \rho_{f_0} c_p W_0 \left[\sigma_{rr}, \sigma_{\theta\theta}, \sigma_{zz}\right]. \tag{44}$$

From (43), the radial and axial deformations then scale as

$$\xi_0 = \alpha R_0 \mathcal{M}. \tag{45}$$

The solid displacement magnitudes must ensure the assumptions of small strains and displacements, i.e. $\xi_0 \ll e$ & $\xi_0/\epsilon \ll R_0$. The former condition is met in the considered low–Mach number framework, i.e. $\mathcal{M} \ll 1$, whereas the latter necessitates

$$\epsilon \gg \alpha \mathcal{M}. \tag{46}$$

At this stage, the as–yet unknown order of magnitude of the solid shear stresses, σ_{rz}^* remains. The latter follows from the axial component of the momentum conservation, or the solid Lamé-Clapeyron equation

$$\rho_{s_0} \partial_t^2 \boldsymbol{\xi}^* = \left(\lambda_s + \mathcal{G}\right) \boldsymbol{\nabla}^* \left(\boldsymbol{\nabla}^* \cdot \boldsymbol{\xi}^*\right) + \mathcal{G} \nabla^{*^2} \boldsymbol{\xi}^* = \boldsymbol{\nabla}^* \cdot \boldsymbol{\sigma}_s^*. \tag{47}$$

Thus, relying on (42)–(44), one finds the solid stress deviatoric component to be

$$\sigma_{rz}^* = \epsilon \rho_{f_0} c_p W_0 \sigma_{rz}. \tag{48}$$

This completes the non–dimensionalisation of the solid stress tensor (43),

$$\boldsymbol{\sigma}_s^* = \rho_{f_0} c_p W_0 \boldsymbol{\sigma}_s \quad \text{, where, } \quad \boldsymbol{\sigma}_s = \begin{pmatrix} \sigma_{rr} & \dots & \epsilon\sigma_{rz} \\ \dots & \sigma_{\theta\theta} & \dots \\ \epsilon\sigma_{rz} & \dots & \sigma_{zz} \end{pmatrix}, \tag{49}$$

with deviatoric and diagonal components

$$\epsilon^2 \frac{\mathcal{C}_{\mathcal{G}}}{\alpha}\sigma_{rz} = \partial_R\zeta + \epsilon^2\partial_Z\xi, \tag{50}$$

$$[\sigma_{rr}, \sigma_{\theta\theta}, \sigma_{zz}] = \frac{\alpha}{\mathcal{C}_{\lambda_s}}\left(\frac{\partial_R}{R}(R\xi) + \partial_Z\zeta\right)[1,1,1] + \frac{2\alpha}{\mathcal{C}_{\mathcal{G}}}\left[\partial_R\xi, \frac{\xi}{R}, \partial_Z\zeta\right]. \tag{51}$$

From (49) dimensionless Lamé-Clapeyron equations (47) read as follows

$$\epsilon^2\frac{\alpha}{\mathcal{D}}\left(\partial_\tau^2\xi - \partial_Z\sigma_{rz}\right) = \frac{\partial_R}{R}(R\sigma_{rr}) - \frac{\sigma_{\theta\theta}}{R}, \tag{52}$$

$$\frac{\alpha}{\mathcal{D}}\partial_\tau^2\zeta = \partial_Z\sigma_{zz} + \frac{\partial_R}{R}(R\sigma_{rz}), \tag{53}$$

or using (50)–(51)

$$\epsilon^2\left(\partial_\tau^2 - \frac{\mathcal{D}}{\mathcal{C}_{\mathcal{G}}}\partial_Z^2\right)\xi = \mathcal{D}\frac{2\mathcal{C}_{\lambda_s} + \mathcal{C}_{\mathcal{G}}}{\mathcal{C}_{\mathcal{G}}\mathcal{C}_{\lambda_s}}\partial_R\left(\frac{\partial_R}{R}(R\xi)\right) + \mathcal{D}\frac{\mathcal{C}_{\mathcal{G}} + \mathcal{C}_{\lambda_s}}{\mathcal{C}_{\mathcal{G}}\mathcal{C}_{\lambda_s}}\partial_R\partial_Z\zeta, \tag{54}$$

$$\epsilon^2\left(\partial_\tau^2 - \mathcal{D}\frac{2\mathcal{C}_{\lambda_s} + \mathcal{C}_{\mathcal{G}}}{\mathcal{C}_{\mathcal{G}}\mathcal{C}_{\lambda_s}}\partial_Z^2\right)\zeta = \frac{\mathcal{D}}{\mathcal{C}_{\mathcal{G}}}\frac{\partial_R}{R}(R\partial_R\zeta) + \epsilon^2\mathcal{D}\frac{\mathcal{C}_{\mathcal{G}} + \mathcal{C}_{\lambda_s}}{\mathcal{C}_{\mathcal{G}}\mathcal{C}_{\lambda_s}}\partial_Z\left(\frac{\partial_R}{R}(R\xi)\right). \tag{55}$$

Whilst fluid dynamics is governed by the boundary layer dimensionless parameter δ, the solid one is controlled by small parameter ϵ. Neglecting $O(\epsilon^2)$ terms leads to radially time–invariance fields, since a zero (52)'s RHS leads to a steady radial stress which is identical with the one found within an elastic tube subjected to a steady internal overpressure. Hence, up to order $O\left(\epsilon^2\right)$ corrections the solid radial deformation quasi–steadily responds to the fluid pressure load, while the axial dynamics are free to propagate as a radially uniform planar wave [16, 19, 22]. Furthermore, since the outer radial fluid pressure derivative in (38) displays a $O\left(\epsilon^{-2}\right)$ correction, the fluid pressure remains uniform per section within the long–wavelength approximation.

2.5. Axial boundary conditions

To set up an axially enclose the problem, a specific set boundary conditions have to be prescribed at the tube's dead ends. The hereby analysis focus on

the reservoir–pipe–anchored valve configuration, a very standard study case in hydraulic and biological communities [22, 41]. These boundary conditions influence both the fluid and the solid dynamic as the problem involves (FSI) considerations. Upstream a homogeneous Dirichlet condition is assumed for unsteady pressure, then impeding any pressure fluctuation at this point, whereas downstream an unsteady fluid velocity variation, i.e. a time–dependent–Dirichlet condition, is imposed

$$P\big|_{Z=0} = 0 \quad \text{, and,} \quad W\big|_{Z=1} = -H_{eav}(\tau), \tag{56}$$

where H_{eav} is the time–dependent Heaviside distribution. For the steady–state, the upstream and downstream pressure conditions are assumed known and constant. On the other hand, the tube is supposed perfectly anchored at its dead ends, i.e. a homogeneous Dirichlet conditions upon the solid axial displacement field ζ, so that no motion occurs at these specific locations

$$\zeta\big|_{Z=0\&1} = 0. \tag{57}$$

The hereby boundary conditions will be clarified in the analysis forthcoming in §4.1.

2.6. Fluid matching and fluid–solid interface continuity conditions

The radial boundary conditions in the boundary layer and at the fluid–solid interface are now considered. No additional stress contributions at the external edges is supposed, so that dimensionless stresses and kinematic continuity conditions read

$$\mathbf{n}_i \left(\mathcal{M}\boldsymbol{\sigma}_{s,st}\big|_{\mathcal{R}_i} + \boldsymbol{\sigma}_s\big|_{\mathcal{R}_i} \right) \mathbf{n}_i = \mathbf{n}_i \left(\mathcal{M}\boldsymbol{\sigma}_{st}\big|_{y=\frac{1-\mathcal{R}_i}{\delta}} + \boldsymbol{\sigma}\big|_{y=\frac{1-\mathcal{R}_i}{\delta}} \right) \mathbf{n}_i, \tag{58}$$

$$\mathbf{n}_o \left(\mathcal{M}\boldsymbol{\sigma}_{s,st}\big|_{\mathcal{R}_o} + \boldsymbol{\sigma}_s\big|_{\mathcal{R}_o} \right) \mathbf{n}_o = \mathbf{0}, \tag{59}$$

$$\mathbf{n}_i \left(\mathcal{M}\boldsymbol{\sigma}_{s,st}\big|_{\mathcal{R}_i} + \boldsymbol{\sigma}_s\big|_{\mathcal{R}_i} \right) \mathbf{t}_i = \mathbf{n}_i \left(\mathcal{M}\boldsymbol{\sigma}_{st}\big|_{y=\frac{1-\mathcal{R}_i}{\delta}} + \boldsymbol{\sigma}\big|_{y=\frac{1-\mathcal{R}_i}{\delta}} \right) \mathbf{t}_i, \tag{60}$$

$$\mathbf{n}_o \left(\mathcal{M}\boldsymbol{\sigma}_{s,st}\big|_{\mathcal{R}_o} + \boldsymbol{\sigma}_s\big|_{\mathcal{R}_o} \right) \mathbf{t}_o = \mathbf{0}, \tag{61}$$

$$\mathbf{e}_r\boldsymbol{\sigma}_{s,st}\big|_{R=1}\mathbf{e}_r = \mathbf{e}_r\boldsymbol{\sigma}_{st}\big|_{y=0}\mathbf{e}_r, \qquad \mathbf{e}_r\boldsymbol{\sigma}_{s,st}\big|_{R=1+\alpha}\mathbf{e}_r = \mathbf{0}, \tag{62}$$

$$\mathbf{e}_r\boldsymbol{\sigma}_{s,st}\big|_{R=1}\mathbf{e}_z = \mathbf{e}_r\boldsymbol{\sigma}_{st}\big|_{y=0}\mathbf{e}_z, \qquad \mathbf{e}_r\boldsymbol{\sigma}_{s,st}\big|_{R=1+\alpha}\mathbf{e}_z = \mathbf{0}, \tag{63}$$

$$\mathbf{u}\big|_{\mathcal{R}_i} = \alpha \partial_\tau \boldsymbol{\xi}\big|_{\mathcal{R}_i}, \tag{64}$$

where $\boldsymbol{\sigma}_{s,st} = \boldsymbol{\sigma}^*_{s,st}/\rho_{f_0} W_0^2$ is the solid pre–stress tensor associated with the steady–state condition. The solid pre–existing stress tensor is not explicitly defined has it will not impact the solid unsteady dynamic due to the linearity of the solid constitutive equations (52)–(55) . On the other hand, the unsteady boundary layer inner fields, (p, w, u), are matched to outer ones (P, W, U) using stretched coordinate η

$$\eta = \frac{1-R}{\delta^\gamma} = \frac{y}{\delta^{\gamma-1}} \sim O(1), \tag{65}$$

associated with stretching parameter $0 < \gamma < 1$, [49], giving matching conditions

$$(P, W, U)\,\big|_{R=1-\delta^\gamma \eta} = (p, w, u)\,\big|_{y=\delta^{\gamma-1}\eta}. \tag{66}$$

The asymptotic analysis of the constitutive fluid and solid equations is now carried out.

3. Asymptotic analysis

3.1. Boundary layer forcing terms and asymptotic framework

Considering the fluid shear stress (25), and expanding (40) yields to

$$\begin{aligned} e^{\frac{\mathcal{M}}{\mathcal{C}^2}(p+\mathcal{M}P_{st})}\left(\partial_\tau w + \mathcal{M}\left((w+W_{st})\,\partial_Z w - \frac{u}{\delta}\left(\tau_f + \partial_y W_{st}\right) + w\partial_Z W_{st}\right)\right) \\ +\mathcal{M}e^{\left(\frac{\mathcal{M}}{\mathcal{C}}\right)^2 P_{st}}\left[e^{\frac{\mathcal{M}}{\mathcal{C}^2}p} - 1\right] W_{st}\partial_Z W_{st} = -\partial_Z p + (\epsilon\delta)^2\,(1+\Gamma)\partial_Z\left[\partial_Z w - \frac{1}{\delta}\left(\partial_y u - \delta\frac{u}{1-\delta y}\right)\right] \\ + \partial_y^2 w - \delta\frac{\tau_f}{1-\delta y} + (\epsilon\delta)^2\,\partial_Z^2 w. \end{aligned} \tag{67}$$

The resulting forced diffusion equation for longitudinal velocity component w provides crucial informations to understand the damping mechanisms. (67)'s terms leading to the wave's energy loss are

- $O\left(\frac{\mathcal{M}}{\mathcal{C}^2}\right)$ and $O\left(\left(\frac{\mathcal{M}}{\mathcal{C}}\right)^2\right)$ fluid density compressibility effects (29);
- $O\left(\epsilon^2\delta\right)$ radial flow compressibility effects within the inner region;

- $O\left(\epsilon^2\delta^2\right)$ and $O\left(\epsilon^2\delta\right)$ axial diffusion and radial flow compressibility;
- $O\left(\mathcal{M}\right)$ axial inertial corrections;
- $O\left(\frac{\mathcal{M}}{\delta}\right)$ radial inertial transport of viscous shear;
- $O\left(\delta\right)$ radial diffusion transport of viscous shear.

Energy losses in the (FSI) problem are thus related to two distinct phenomena: diffusion and inertia, which may, or may not, simultaneously contribute regarding their respective orders of magnitude. The presented low–Mach number asymptotic framework, i.e. neglecting inertial over viscous contributions, applies when

$$\delta \gg \frac{\mathcal{M}}{\delta} \gg \mathcal{M}, \tag{68}$$

which is consistent with (18). The dimensionless numbers ordering spelled out in (18) is herein clarified regarding (46) and (79). The radial diffusion transport of viscous shear is thus the damping mechanism under focus. Further investigations could be conducted out to analyze the impact of distinct asymptotic regimes on the long–time dynamics. A high–Mach number case was asymptotically considered by [50] for a practical case of a hydroelectric power plant. Ignoring (FSI), the low–Mach boundary layer theory has been brilliantly investigated by [41, 42].

3.2. Multiple time–scale approach

Next, the time variations of all considered fields are decomposed into fast–time associated with wave propagation and slow–time associated with the damping envelope as well as a phase-shift that arises from friction dissipation, [49]. Let us note the slow-time scale T. Since the corrections of interest in the axial momentum conservation equation (67) are of order $O\left(\delta\right)$, this slow time-scale should scale as follows

$$T = \delta\tau, \quad \text{so} \qquad \text{that} \quad \partial_t \equiv \frac{c_p}{L}\left(\partial_\tau + \delta\partial_T\right). \tag{69}$$

In this multiple time-scale approach, all previous time–derivatives fulfill a chain-rule correction given by $\partial_\tau + \delta\partial_T$. For the framework being established, one must consider the coupling conditions between the solid and fluid given by stress and kinematic continuity at the fluid–solid interface within this asymptotic scheme.

3.3. Asymptotic sequence

In the herein δ–driven asymptotic framework, a regular asymptotic sequence for solid displacement components (ξ, ζ), inner/outer velocity fields $(u, w)\,, (U, W)$, inner/outer pressures $[p, P]$, fluid shear stresses $[\tau_f, \tau_w]$, and solid stress tensor components $[\sigma_{rz}, \sigma_{rr}, \sigma_{\theta\theta}, \sigma_{zz}]$ is searched for

$$[\xi, \zeta] = [\xi, \zeta]^0 + \delta\,[\xi, \zeta]^1 + O\,(X)\,, \tag{70}$$

$$[u, w, U, W] = [u, w, U, W]^0 + \delta\,[u, w, U, W]^1 + O\,(X)\,, \tag{71}$$

$$[p, P] = [p, P]^0 + \delta\,[p, P]^1 + O\,(X)\,, \tag{72}$$

$$[\tau_f, \tau_w] = [\tau_f, \tau_w]^0 + \delta\,[\tau_f, \tau_w]^1 + O\,(X)\,, \tag{73}$$

$$[\sigma_{rz}, \sigma_{rr}, \sigma_{\theta\theta}, \sigma_{zz}] = [\sigma_{rz}, \sigma_{rr}, \sigma_{\theta\theta}, \sigma_{zz}]^0 + \delta\,[\sigma_{rz}, \sigma_{rr}, \sigma_{\theta\theta}, \sigma_{zz}]^1 + O\,(X)\,, \tag{74}$$

with $X \equiv \max\left(\delta^2, \mathcal{M}/\delta, \epsilon^2, \delta\epsilon, \alpha\mathcal{M}\right)$. In the following, the influence of the steady-state flow is dicarded, since irrelevant up to the considered $O(\delta)$ corrections, as shown in Appendix A.

3.4. Correction on the inner tube radius position, $\mathcal{R}_i^*$

The fluid–solid interface position, which is characterized by $\mathcal{R}_i^*$ defined in (3), is expected to vary as the fluid overpressure wave propagates. Using solid displacement scalings (45), one finds

$$\mathcal{R}_i(Z + \alpha\mathcal{M}\zeta(1, Z, \tau), \tau) = 1 + \alpha\mathcal{M}\xi(1, Z, \tau). \tag{75}$$

Taylor-expanding (75) leads to

$$\mathcal{R}_i(Z+\alpha\mathcal{M}\zeta(1, Z, \tau) = \mathcal{R}_i(Z, \tau)+\alpha\mathcal{M}\zeta(1, Z, \tau)\partial_Z\mathcal{R}_i(Z, \tau)+O\left(\left(\alpha\mathcal{M}\right)^2\right), \tag{76}$$

so that combining (75) and (76), one finally gets

$$\mathcal{R}_i(Z, \tau, T) = 1 + O\,(\alpha\mathcal{M})\,. \tag{77}$$

By following the same footsteps, an equivalent relation is achieved for $\mathcal{R}_o^*(z,t)$. The dimensionless normal and tangential vectors, $(\mathbf{n}_i, \mathbf{n}_o)$ and $(\mathbf{t}_i, \mathbf{t}_o)$ respectively then fulfills

$$\mathbf{n}_i = \mathbf{n}_o = \mathbf{e}_r + O\left(\alpha\epsilon\mathcal{M}\right), \qquad \mathbf{t}_i = \mathbf{t}_o = \mathbf{e}_z + O\left(\alpha\epsilon\mathcal{M}\right). \tag{78}$$

Thus, in the considered low–Mach number asymptotic framework, the response of the inner and outer tube's radius to overpressure is irrelevant as long as

$$\delta \gg \alpha\mathcal{M} \gg \alpha\epsilon\mathcal{M}. \tag{79}$$

These asymptotically unperturbed normal and tangent vectors, combined with the order of magnitudes of the steady–state radial gradient contribution (A.5) into the deviatoric part of $\boldsymbol{\sigma}_{st}$ in (26), thus justifies continuity condition (58)-(61) to be applied to unsteady fluid and solid fields only, i.e. without coupling with steady–state. The stress and velocity continuity conditions in (58)-(64) thus finally reads

$$\begin{aligned}
\sigma_{rr}\big|_{R=1+O(\alpha\mathcal{M})} &= -p\big|_{y=O\left(\frac{\alpha\mathcal{M}}{\delta}\right)} + O\left(\alpha\epsilon\mathcal{M}\right), \\
\sigma_{rr}\big|_{R=1+\alpha+O(\alpha\mathcal{M})} &= O\left(\alpha\epsilon\mathcal{M}\right), \\
\sigma_{rz}\big|_{R=1+O(\alpha\mathcal{M})} &= -\delta\tau_w\big|_{y=O\left(\frac{\alpha\mathcal{M}}{\delta}\right)} + O\left(\alpha\epsilon\mathcal{M}\right), \\
\sigma_{rz}\big|_{R=1+\alpha+O(\alpha\mathcal{M})} &= O\left(\alpha\epsilon\mathcal{M}\right), \\
\alpha\left(\partial_\tau + \delta\partial_T\right)\xi\big|_{R=1+O(\alpha\mathcal{M})} &= u\big|_{y=O\left(\frac{\alpha\mathcal{M}}{\delta}\right)} + O\left(\alpha\epsilon\mathcal{M}\right), \\
\alpha\left(\partial_\tau + \delta\partial_T\right)\zeta\big|_{R=1+O(\alpha\mathcal{M})} &= w\big|_{y=O\left(\frac{\alpha\mathcal{M}}{\delta}\right)} + O\left(\alpha\epsilon\mathcal{M}\right),
\end{aligned} \tag{80}$$

where $[\sigma_{rr}, \sigma_{rz}]$ are provided in (50)–(51), respectively. Thus, in the considerd asymptotic low–Mach framework, the unsteady fluid and solid components decouple each other. In the forthcoming, only the system unsteadiness response will be investigated.

3.5. Fluid structure interaction equations

3.5.1. Stress and kinematic continuity at the tube wall

The stress and kinematic continuity relationships (58)-(64) hold at the fluid–solid interface, where $\boldsymbol{\sigma}$ and $\boldsymbol{\sigma}_s$ are defined in (27) and (49), respectively. Re-

garding the tangential stress continuity in (60)–(61) it is noteworthy that the deviatoric dimensionless fluid stress tensor $\boldsymbol{\sigma}$ components scales as $O(\epsilon\delta)$. Moreover, since from (48) the dimensionless solid deviatoric part scales as $O(\epsilon)$, there is a $O(\delta)$ mismatch between them. It then result that the boundary layer influence on the solid shear stress is not sensible at leading–order. It only arises at order $O(\delta)$. The leading– and first– orders kinematic and stress continuity conditions (58)-(64) thus finally simplify to

$$\sigma^0_{rr}\big|_{R=1} = -p^0\big|_{y=0}, \qquad \sigma^1_{rr}\big|_{R=1} = -p^1\big|_{y=0}, \tag{81}$$

$$\sigma^0_{rr}\big|_{R=1+\alpha} = 0, \qquad \sigma^1_{rr}\big|_{R=1+\alpha} = 0, \tag{82}$$

$$\sigma^0_{rz}\big|_{R=1} = 0, \qquad \sigma^1_{rz}\big|_{R=1} = -\tau^0_w\big|_{y=0}, \tag{83}$$

$$\sigma^0_{rz}\big|_{R=1+\alpha} = 0, \qquad \sigma^1_{rz}\big|_{R=1+\alpha} = 0, \tag{84}$$

$$\alpha\partial_\tau\xi^0\big|_{R=1} = u^0\big|_{y=0}, \qquad \alpha\left(\partial_\tau\xi^1\big|_{R=1} + \partial_T\xi^0\big|_{R=1}\right) = u^1\big|_{y=0}, \tag{85}$$

$$\alpha\partial_\tau\zeta^0\big|_{R=1} = w^0\big|_{y=0}, \qquad \alpha\left(\partial_\tau\zeta^1\big|_{R=1} + \partial_T\zeta^0\big|_{R=1}\right) = w^1\big|_{y=0}. \tag{86}$$

3.5.2. Solid equations

The Lamé–Clapeyron equations (52)–(53), or more explicitly (54)–(55), along with dimensionless Hooke's law (50)–(51), provide information on the R-dependence of the solid's fields

$$\partial_R\left(\frac{\partial_R}{R}\left(R\left[\xi^0+\delta\xi^1\right]\right)\right) = -\frac{\mathcal{C}_\mathcal{G}+\mathcal{C}_{\lambda_s}}{\mathcal{C}_\mathcal{G}\mathcal{C}_{\lambda_s}}\partial_R\partial_Z\left[\zeta^0+\delta\zeta^1\right], \tag{87}$$

$$\partial_R\left[\zeta^0+\delta\zeta^1\right] = 0, \tag{88}$$

$$\sigma^0_{rz} - \frac{\sigma^0_{rz}|_{R=1}}{R} = \frac{1}{R}\int_1^R R\left[\frac{\alpha}{\mathcal{D}}\partial^2_\tau\zeta^0 - \partial_Z\sigma^0_{zz}\right]dr, \tag{89}$$

$$\sigma^1_{rz} - \frac{\sigma^1_{rz}|_{R=1}}{R} = \frac{1}{R}\int_1^R R\left[\frac{\alpha}{\mathcal{D}}\left(\partial^2_\tau\zeta^1 + 2\partial_T\partial_\tau\zeta^0\right) - \partial_Z\sigma^1_{zz}\right]dr, \tag{90}$$

$$\sigma^0_{zz} + \delta\sigma^1_{zz} = \alpha\frac{2\mathcal{C}_{\lambda_s}+\mathcal{C}_\mathcal{G}}{\mathcal{C}_\mathcal{G}\mathcal{C}_{\lambda_s}}\partial_Z\left[\zeta^0+\delta\zeta^1\right] + \frac{\alpha}{\mathcal{C}_{\lambda_s}}\frac{\partial_R}{R}\left(R\left[\xi^0+\delta\xi^1\right]\right). \tag{91}$$

Equation (88) highlights the radial uniformity of solid axial displacement at leading– and first–orders. This uniformity along R follows from the long–wavelength assumptions, that is, the irrelevance of radial inertia when discarding $O(\epsilon^2)$ as already discussed in §3.1. This also implies a simplification of (87) by enforcing its RHS to equal zeros. After defining six R–invariant functions,

namely $H_1^{0,1}$, $H_2^{0,1}$ and $H_3^{0,1}$, the leading– and first–orders displacement fields fulfill

$$\zeta^0 + \delta\zeta^1 = H_1^0(Z,\tau,T) + \delta H_1^1(Z,\tau,T), \tag{92}$$

$$\xi^0 + \delta\xi^1 = \frac{H_2^0(Z,\tau,T) + \delta H_2^1(Z,\tau,T)}{2} R + \frac{H_3^0(Z,\tau,T) + \delta H_3^1(Z,\tau,T)}{R} \tag{93}$$

The relation (92) is the first integral of (88) and (93) the first integral of (87)'s LHS. This similarly ensures the uniform behavior of the integrands of both (89) and (90). The shear continuity conditions in (83) and (84) then yield to

$$\frac{\alpha}{\mathcal{D}}\left(\partial_\tau^2\left[\zeta^0 + \delta\zeta^1\right] + 2\delta\partial_T\partial_\tau\zeta^0\right) - \partial_Z\left[\sigma_{zz}^0 + \delta\sigma_{zz}^1\right] = \frac{2\delta\tau_w^0}{\alpha(2+\alpha)}. \tag{94}$$

The as–yet–unknown functions $H_2^{0,1}$ and $H_3^{0,1}$ are prescribed by the normal–stress continuity conditions (81)–(82)

$$H_2^0 + \delta H_2^1 = \frac{\mathcal{C}_{\lambda_s}\mathcal{C}_{\mathcal{G}}}{\mathcal{C}_{\mathcal{G}} + \mathcal{C}_{\lambda_s}}\left(\frac{p^0 + \delta p^1}{\alpha^2(2+\alpha)} - \frac{1}{\mathcal{C}_{\lambda_s}}\partial_Z\left[\zeta^0 + \delta\zeta^1\right]\right), \tag{95}$$

$$H_3^0 + \delta H_3^1 = \frac{\mathcal{C}_{\mathcal{G}}}{\alpha}\frac{(1+\alpha)^2}{2\alpha(2+\alpha)}\left[p^0 + \delta p^1\right]. \tag{96}$$

Using that $\mathcal{C}_{\mathcal{G}}/(\mathcal{C}_{\mathcal{G}} + \mathcal{C}_{\lambda_s}) = 2\nu_s$, $H_2^{0,1}$ and $H_3^{0,1}$ reduce to

$$H_2^0(Z,\tau,T) + \delta H_2^1(Z,\tau,T) = 2\nu_s\left(\frac{\mathcal{C}_{\lambda_s}}{\alpha}\frac{p^0 + \delta p^1}{\alpha(2+\alpha)} - \partial_Z\left[\zeta^0 + \zeta^1\right]\right), \tag{97}$$

$$H_3^0(Z,\tau,T) + \delta H_3^1(Z,\tau,T) = \frac{\mathcal{C}_{\mathcal{G}}}{\alpha}\frac{(1+\alpha)^2}{2\alpha(2+\alpha)}\left[p^0 + \delta p^1\right], \tag{98}$$

thus fulfilling the radial displacement expression in (93) at each order

$$\xi^0 + \delta\xi^1 = \frac{2\nu_s\mathcal{C}_{\lambda_s}R + \frac{(1+\alpha)^2\mathcal{C}_{\mathcal{G}}}{R}}{\alpha(2+\alpha)}\frac{p^0 + \delta p^1}{2\alpha} - \nu_s R\partial_Z(\zeta^0 + \delta\zeta^1) \tag{99}$$

$$\xi^0\big|_{R=1} + \delta\xi^1\big|_{R=1} = \frac{\chi(p^0 + \delta p^1)}{2\alpha} - \nu_s\partial_Z(\zeta^0 + \delta\zeta^1), \tag{100}$$

with χ given in (13). Noting that $2\alpha/\mathcal{C}_{\mathcal{G}} + \alpha(1-2\nu_s)/\mathcal{C}_{\lambda_s} = \alpha\mathcal{C}_s^2/\mathcal{D}$, and considering the dimensionless Hooke stress tensor (50)–(51), direct relations between the normal solid stress components, p^0 and $\partial_Z\zeta^0$ are found

$$\sigma_{rr}^0(R,Z,\tau,T) + \delta\sigma_{rr}^1(R,Z,\tau,T) = \left[1 - \frac{(1+\alpha)^2}{R^2}\right]\frac{p^0 + \delta p^1}{\alpha(2+\alpha)}, \tag{101}$$

$$\sigma_{\theta\theta}^0(R,Z,\tau,T) + \delta\sigma_{\theta\theta}^1(R,Z,\tau,T) = \left[1 + \frac{(1+\alpha)^2}{R^2}\right]\frac{p^0 + \delta p^1}{\alpha(2+\alpha)}, \tag{102}$$

$$\sigma_{zz}^0(Z,\tau,T) + \delta\sigma_{zz}^1(Z,\tau,T) = 2\nu_s\frac{p^0 + \delta p^1}{\alpha(2+\alpha)} + \frac{\alpha\mathcal{C}_s^2}{\mathcal{D}}\partial_Z\left[\zeta^0 + \delta\zeta^1\right] \tag{103}$$

Thus, (101) and (102) recover the known radial dependence of stresses in thick pipes [51]. In the $\alpha \ll 1$ limit, (101) also provides the thin–wall shell theory for which the radial stress linearly varies along the radial direction, that is $\sigma^0_{rr} = p^0(r-(R_0+e))/e+O(\alpha^2)$, from the applied fluid pressure at the inner pipe radius to the zero external pressure at the outer one. Furthermore, as $\alpha \ll 1$, the hoop stress $\sigma_{\theta\theta}$ is found to be constant and thin-wall shell theory (more often named circumferential tension) is recovered (i.e $\sigma_{\theta\theta} = p^0/\alpha+O(\alpha^2)$) since $1/\alpha$ is approximately the ratio of the average radius over the pipe wall thickness up to $O(\alpha^2)$ corrections. It is also interesting to note that σ^0_{zz} does not exhibit a radial dependence, a feature known in thin-wall shell theory (where σ^0_{zz} is called longitudinal tension), which extends to thick walls. Finally, the dependence of σ^0_{zz} with R is found consistent with thin–wall shell theory [10].

3.5.3. Fluid equations in the bulk outer region

The outer leading– and first–orders fluid behaviors are governed by mass and momentum conservation equations (36)–(38). Using the asymptotic sequence given in §3.3 along with the multi–time scale decomposition discussed in §3.2 leads to the following

$$\partial_\tau \left[P^0 + \delta P^1\right] + \delta\partial_T P^0 + \mathcal{C}^2 \partial_Z \left[W^0 + \delta W^1\right] = -\mathcal{C}^2 \frac{\partial_R}{R}\left(R\left[U^0 + \delta U^1\right]\right), \quad (104)$$

$$\partial_\tau \left[W^0 + \delta W^1\right] + \delta\partial_T W^0 = -\partial_Z \left[P^0 + \delta P^1\right], \quad (105)$$

$$\partial_R \left[P^0 + \delta P^1\right] = 0. \quad (106)$$

At leading–order since $\partial_R P^0 = 0$ from (106), and, from the R derivative of (105), $\partial_\tau \partial_R W^0 = 0$. If $\partial_R W^0 = 0$ is initially set at $\tau = 0$, then $\partial_R W^0 = 0$ for all times. The same applies for P^1 and W^1. The radial uniformity of both outer pressure and axial velocity thus arises at leading– and first–orders, so that the LHS of (104) does not depend on R. We therefore introduce functions $\mathcal{F}^0(Z,\tau,T)$ and $\mathcal{F}^1(Z,\tau,T)$ so that

$$U^0 + \delta U^1 = -\frac{R}{2}\left[\mathcal{F}^0(Z,\tau,T) + \delta\mathcal{F}^1(Z,\tau,T)\right], \quad (107)$$

and consequently from (104), it yields

$$\partial_\tau \left[P^0 + \delta P^1\right] + \delta\partial_T P^0 + \mathcal{C}^2 \partial_Z \left[W^0 + \delta W^1\right] = \mathcal{C}^2 \left[\mathcal{F}^0 + \delta\mathcal{F}^1\right]. \quad (108)$$

3.5.4. Fluid equations in the inner boundary layer region

The inner flow is driven by the boundary layer's rescaled mass and momentum conservation equations, (39)–(41). Up to first–order, one obtains the following

$$\delta\left(\partial_\tau p^0 + \mathcal{C}^2\partial_Z w^0\right) = \mathcal{C}^2\partial_y\left[u^0 + \delta u^1\right] - \delta\mathcal{C}^2 u^0, \tag{109}$$

$$\left(\partial_\tau - \partial_y^2\right)\left[w^0 + \delta w^1\right] = -\partial_Z\left[p^0 + \delta p^1\right] - \delta\left(\partial_T w^0 + \tau_f^0\right), \tag{110}$$

$$\partial_y\left[p^0 + \delta p^1\right] = 0. \tag{111}$$

As in the outer region (106), the inner pressure in (111) is uniform upon the radial re–scaled variable y, leading to pressure continuity per section at both orders

$$p^0 = P^0, \quad p^1 = P^1. \tag{112}$$

At leading–order, the inner mass equation (109) gives $\partial_y u^0 = 0$, so that the normal kinematic continuity condition (85) reads

$$u^0 = \alpha\partial_\tau \xi^0|_{R=1}, \tag{113}$$

or, equivalently, invoking (100)

$$u^0 = \frac{\chi}{2}\partial_\tau P^0 - \alpha\nu_s\partial_Z\partial_\tau\zeta^0. \tag{114}$$

Furthermore, re–arranging the $O(\delta)$ terms in (109) along with the kinematic continuity condition (85) leads to

$$u^1 = \frac{y}{\mathcal{C}^2}\partial_\tau P^0 + \partial_Z\int_0^y w^0 dy' + y\alpha\partial_\tau\xi^0\big|_{R=1} + \alpha\left[\partial_\tau\xi^1 + \partial_T\xi^0\right]_{R=1}. \tag{115}$$

3.6. Outer and inner fluid velocity matching

The as–yet–unknown velocity functions $\mathcal{F}^0(Z,\tau,T)$ and $\mathcal{F}^1(Z,\tau,T)$, defined in (107), are fully determined by the asymptotic matching of radial velocities between the inner boundary layer and the outer region, as presented in §2.6. This matching nevertheless requires the knowledge of $\int_0^y w^0 dy'$ accordingly to (115). For the sake of simplicity, the analysis is handled in the Laplace domain.

The Laplace transform $\mathcal{L}$ with respect to the fast time τ is denoted by a tilde. So far any dependent variable $f(Z,\tau,T)$, we write

$$\tilde{f}(Z,s,T)=\mathcal{L}\left(f(Z,\tau,T)\right)=\int_0^\infty f(Z,\tau^{'},T)e^{-s\tau^{'}}d\tau^{'}. \tag{116}$$

With all unsteady fields initially at rest, the Laplace transform will map time derivatives into factors of the transform variable s. The inner leading–order axial velocity, w^0, is governed by a diffusion equation (86), so that its Laplace transform is

$$\tilde{w}^0=s\alpha\tilde{\zeta}^0e^{-\sqrt{s}y}-\frac{1}{s}\partial_Z\tilde{P}^0\left[1-e^{-\sqrt{s}y}\right], \tag{117}$$

where the axial kinematic continuity condition at the tube wall have been used. The Laplace transform of (105)'s leading–order produces

$$\tilde{W}^0=-\frac{1}{s}\partial_Z\tilde{P}^0, \tag{118}$$

which implies

$$\lim_{y\to\infty}\tilde{w}^0=\tilde{W}^0+E.S.T, \tag{119}$$

where E.S.T="exponentially small terms". The asymptotic matching of axial velocities is directly guaranteed since they are far from the wall (i.e. for $y=\frac{1-R}{\delta}\gg 1$). The leading–order shear rate $\tilde{\tau}_f^0$ and wall shear rate $\tilde{\tau}_w^0$ can be deduced from (117)

$$\tilde{\tau}_f^0 = \partial_y\tilde{w}^0=-\sqrt{s}\left[\frac{1}{s}\partial_Z\tilde{P}^0+s\alpha\tilde{\zeta}^0\right]e^{-\sqrt{s}y}, \tag{120}$$

$$\tilde{\tau}_w^0 = -\sqrt{s}\left[\frac{1}{s}\partial_Z\tilde{P}^0+s\alpha\tilde{\zeta}^0\right]. \tag{121}$$

As expected, the leading–order wall shear rate is a linear combination of the leading–order pressure P^0 and solid axial displacement ζ^0 from tangential velocity continuity at the tube wall (86). The derived parietal shear rate appears to be a combination of the $s\to 0$ leading contribution of the theoretical parietal shear rate found by [36], namely $-\partial_Z\tilde{P}^0/\sqrt{s}$, which provides a convolution kernel in time space as well as a new (FSI) shear rate contribution $(-\alpha s\sqrt{s}\tilde{\zeta}^0)$. Noteworthy, [36] found other corrective contributions in his Laplace shear rate, which were related to the fact that his analysis did not consider an asymptotic

boundary layer. However, neglecting the (FSI) corrections leads to an inconsistency regarding the velocity continuity condition. The wall shear rate expressed within the time domain falls from a classical solution to the diffusion equation, yielding the following

$$\tau_w^0(Z,\tau,T) = \frac{1}{\sqrt{\pi}} \int_0^\tau \frac{\partial_{\tau'} \left[W^0(Z,\tau',T) - \alpha \partial_{\tau'} \zeta^0(Z,\tau',T) \right]}{\sqrt{\tau - \tau'}} d\tau'. \tag{122}$$

The convolution kernel derived herein (i.e. $1/\sqrt{\pi t}$), is identical to the leading–order contribution of [36]'s kernel while also sharing the same form as that of [52]. On the other hand, our analysis reveals that the relevant acceleration to be considered in the convolution product must be the *relative* acceleration of the fluid to that of the pipe's wall, for ensuring asymptotic consistency. Suggested by [20], the solid contribution to the fluid wall shear rate is hereby rigorously established. The matching condition upon the radial fluid velocities, spelled out in (66), reads

$$\left(\tilde{U}^0 + \delta \tilde{U}^1 \right) \big|_{R=1-\delta^\gamma \eta} = \left(\tilde{u}^0 + \delta \tilde{u}^1 \right) \big|_{y=\delta^{\gamma-1}\eta}, \tag{123}$$

where η is the stretched coordinates defined in (65). The matching procedure thus constrains the expression of the unknown velocity functions $\mathcal{F}_1^0(Z,\tau,T)$ in (107), yielding to

$$\mathcal{F}^0(Z,\tau,T) = -\chi \partial_\tau P^0 + 2\alpha \nu_s \partial_Z \partial_\tau \zeta^0, \tag{124}$$

$$\mathcal{F}^1(Z,\tau,T) = -\chi \partial_\tau P^1 + 2\alpha \nu_s \partial_Z \partial_\tau \zeta^1 + \int_0^\tau \left(\partial_T \mathcal{F}^0 + 2 \partial_Z \tau_w^0 \right) dt. \tag{125}$$

The full derivation of these expressions can be found in Appendix B.

3.7. Discussion on the fluid–filled pipe asymptotic (FSI) scheme

Based on many relations involved, it seems critical to focus on relations (100) and (103) as they reveal the radial–axial and axial stress–pressure Poisson coupling discussed many times in the literature (e.g. [13, 14, 22]). The Poisson's modulus indeed converts the radial displacement (i.e. pipe breathing and overpressure) into axial displacement and axial stress, respectively. In the

limit $\nu_s \to 0$, this coupling vanishes and the only remaining coupling comes from the radial term. In this zero Poisson coupling limit the pipe can consequently be regarded as successive elastic cylindrical rings independent of each other, as proposed by [4]. Figure 2 depicts the various couplings that occur in this asymptotic framework, thus providing a comprehensive description and detailed inventory. This scheme is completed by Table 1 that provides the related mechanical couplings as well as the associated relations in the derivation.

Table 1: Description of the asymptotic scheme for the fluid–structure–interaction that occur within a fluid–filled elastic tube system.

Relation	**Mechanical coupling**	**Asymptotic sequence**
[1,13]	Normal stress continuity	(81) + (82)
[2,14]	Radial Hooke's law	(43) + [1,13] + (93) = (100)
[3], [15]-[15] & [21]	Normal velocity continuity	(85) + (109) = (113) + (115)
[4,16]	Radial fluid velocity matching	(123) + Appendix B
[5], [17]-[17]	Outer fluid mass conservation	(107) + (108)
[6], [18]-[18]	Outer fluid axial momentum conservation	(105)
[7],[19]-[19]	Solid axial momentum conservation	(83) + (84) + (89) = (94)
[8,20]	Axial Hooke's law	(91) + (93) = (103)
[9]	Tangential velocity continuity	(86) + (103)
[10]	Fluid pressure matching	(106) + (111) + (112)
[11]	Inner fluid axial momentum conservation	(110)
[12]	Definition of the fluid shear stress	(120)
[22]	Tangential stress continuity	(83) + (84) + (89) + (90)
[23]	Axial fluid velocity matching	(119)

The red loops, (i.e. arrows [1]–[6] and [13]–[18]), in Figure 2 are related to (FSI), resulting in the pulse–wave speed c_p modification occurring from the presence of the surrounding elastic tube. Its mechanism is detailed as follows. First, the pressure pulse is radially transmitted to the solid through stress continuity [1]. Then, the elastic Hooke's rheology transforms this radial stress into solid deformations [2]. The resulting radial velocity displacement should ensure velocity continuity conditions at the tube wall and thus match the inner fluid velocity [3]. A second matching on radial fluid velocity occurs at the boundary layer's interface [4], and the mass conservation equation in the outer region allows one to relate these radial velocity perturbations to the initial pressure pulse and axial velocity [5]. The axial momentum conservation equation [6] provides an outer relation between acceleration and the pressure gradient, which is necessary for closing the model. The red loop is nevertheless slaved to an unknown longitudinal displacement ζ^0 according to [2] which is a consequence of the Poisson coupling effects. Identical successive couplings also apply at first–order, resulting in the second loop (see arrows [13]–[18]).

The green relations, (i.e. [7]–[8] and [19]–[20]), result from the combination of both the axial momentum-conservation equation and elastic Hooke's rheology. This combination produces a hyperbolic system upon ζ^0 and σ^0_{zz} enslaved by the fluid overpressure p^0. Both hyperbolic systems arising from the red and green loops are consequently coupled through ν_s parameter.

The leading–order fluid shear stress follows from a combination of a pressure uniformity and continuity argument [10], an inner axial momentum conservation equation [11], an axial velocity conservation equation expressed on the axial shear stress, [9], and the fluid shear stress definition [12]. While most damping models [53], [52], [54], [55], consider near–wall fluid friction, an additional fluid shear stress occurring from the solid axial dynamic has to be considered. This additional term is nevertheless required in terms of the axial velocity continuity

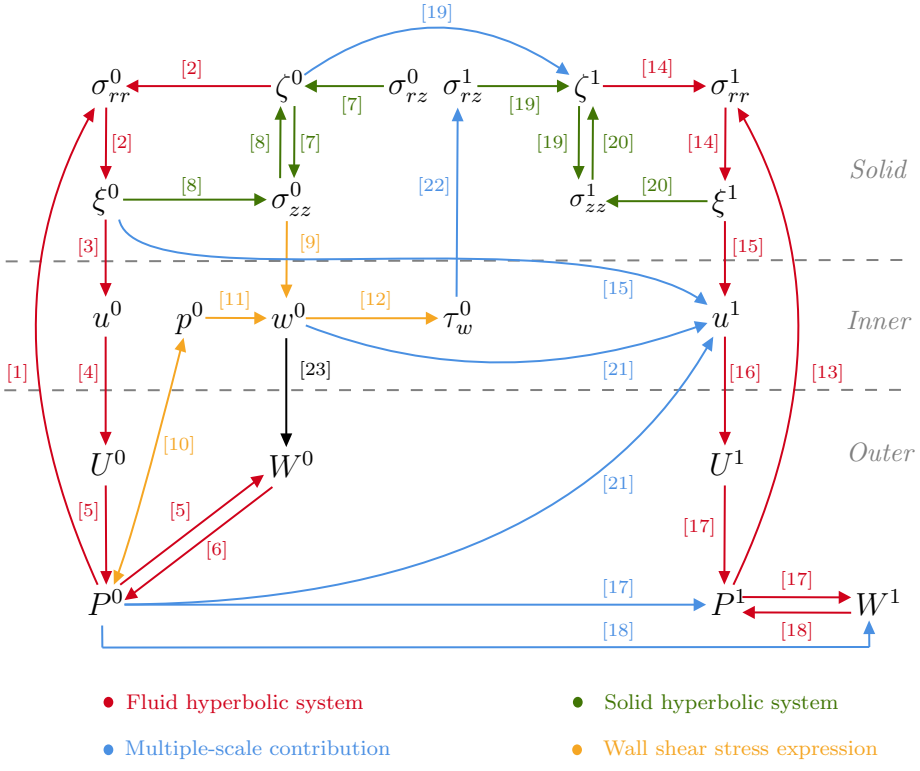

Figure 2: Asymptotic scheme for fluid–structure–interaction in a fluid–filled elastic tube.

conditions. As the axial velocity matching [23] does not introduce any further information to the coupling scheme, it is omitted from the discussion as a secondary by-product of the analysis.

At first–order, the slow–time contribution and $O(\delta)$ corrections provide additional contributions that must be considered to evaluate the damping of the leading–order. The various contributions are indicated in Figure 2 with blue arrows (i.e. [15], [17], [18], [19], [21] and [22]). At this stage, however the combined effect of these various terms on damping is not easy to summarize, even if it can be re–cast into a highly compact form, as derived later in Section §4.

3.8. (FSI) coupled hyperbolic system

Appendix C shows that the resulting coupled waves equations reads

$$\left(\partial_\tau^2 - \mathbf{C}_\mathbf{P}^2 \partial_Z^2\right)\left[\mathbf{P}^0 + \delta\mathbf{P}^1\right] = -2\delta\left[\partial_T\partial_\tau\mathbf{P}^0 - \partial_Z\tau_w^0\begin{pmatrix} 1+\frac{2\nu_s\mathcal{D}}{\alpha(2+\alpha)} \\ \frac{1}{\alpha(2+\alpha)}\left[2\nu_s\mathcal{D}+\mathcal{C}_s^2+\frac{4\nu_s^2\mathcal{D}}{\alpha(2+\alpha)}\right]\end{pmatrix}\right], \tag{126}$$

where

$$\mathbf{C}_\mathbf{P}^2 = \begin{pmatrix} 1 & 2\nu_s\mathcal{D} \\ \frac{2\nu_s}{\alpha(2+\alpha)} & \frac{4\nu_s^2\mathcal{D}}{\alpha(2+\alpha)}+\mathcal{C}_s^2\end{pmatrix} \quad \text{, and,} \quad \mathbf{P}^0+\delta\mathbf{P}^1 = \begin{pmatrix} P^0+\delta P^1 \\ \sigma_{zz}^0+\delta\sigma_{zz}^1\end{pmatrix}. \tag{127}$$

The leading–order of (126) displays a parabolic form without dissipation associated with a fast time–scale wave propagation, as opposed to the additional slow–time scale damping that arises when $O(\delta)$ corrections are considered. This short–time behavior appears because the dissipation in the fluid boundary layer does not have time to develop; thus, the coupled system remains purely conservative. The eigenvalues $c_\pm$ of $\mathbf{C}_\mathbf{P}^2$ provide the (FSI)'s impact on the previously defined *intrinsic* wave speeds c_p and c_s. More precisely, since c_p is selected as the reference speed, $c_p c_-$ provides the fluid pulse pressure wave speed mode while $c_p c_+$ provides the elastic wave speed mode. The eigenvalues $c_\pm^2$ are found equal to

$$c_\pm^2 = \frac{1+\mathcal{C}_s^2+\frac{4\nu_s^2\mathcal{D}}{\alpha(2+\alpha)} \pm \sqrt{\left(1+\mathcal{C}_s^2+\frac{4\nu_s^2\mathcal{D}}{\alpha(2+\alpha)}\right)^2 - 4\mathcal{C}_s^2}}{2}. \tag{128}$$

In dimensional form, these expressions are identical to those of [22]. In the latter, and for the sake of brevity, the sum of the squared speed $\overline{c^2}$ is introduced

$$\overline{c^2} = c_+^2 + c_-^2 = 1 + \mathcal{C}_s^2 + \frac{4\nu_s^2\mathcal{D}}{\alpha(2+\alpha)}. \tag{129}$$

The asymptotic behavior with respect to the α parameter of all dimensionless (FSI) characteristic wave speeds is provided in Figure 3. As α increases or $\nu_s \to 0$, the dimensionless positive and negative wave speed mode, $c_\pm$, respectively tend to $\mathcal{C}_s$ and one according to (128), as depicted in Figures 3b, 3c and 3d. In other words, in the $\nu_s \to 0$ limit the wave-speed remains unhampered by the (FSI) and the pressure pulse propagates at c_p within the fluid while the elastic wave at c_s within the tube. For the wave speed signatures depicted here, the pulse wave speed modifications, (i.e. corrections in c_-, Cf. Figure 3c), remains low and do not exceed 6% (for $\nu_s = 0.35$).

3.9. Axial gradient of the wall shear rate, $\partial_Z \tau_w^0$

Let us now derive the previous expression of the parietal shear rate, τ_w^0 with respect to Z in (121) to enclose the 2D vector wave equation (126). Combining it with the leading–order Laplace transforms of (C.1) and (C.2) leads to

$$\partial_Z \tilde{\tau}_w^0 = -s\sqrt{s}\left(\tilde{P}^0 + \alpha(1-2\nu_s)\partial_Z\tilde{\zeta}^0\right), \tag{130}$$

while the use of (C.5) transforms it into

$$\partial_Z \tilde{\tau}_w^0 = -s\sqrt{s}\left(\left[1-(1-2\nu_s)\frac{2\nu_s\mathcal{D}}{\alpha\mathcal{C}_s^2(2+\alpha)}\right]\tilde{P}^0 + (1-2\nu_s)\frac{\mathcal{D}}{\mathcal{C}_s^2}\tilde{\sigma}_{zz}^0\right). \tag{131}$$

The axial gradient of the fluid wall shear stress appears to be a linear combination of $\tilde{P}^0$ and $\tilde{\sigma_{zz}^0}$; thus, the vector–wave equation defined in (126) ensues in the Laplace domain

$$\left(s^2 - \mathbf{C}_\mathbf{P}^2\partial_Z^2\right)\tilde{\mathbf{P}}^0 = \mathbf{0}, \tag{132}$$

$$\left(s^2 - \mathbf{C}_\mathbf{P}^2\partial_Z^2\right)\tilde{\mathbf{P}}^1 = -2s\left[\partial_T + \sqrt{s}\mathbf{E}\right]\tilde{\mathbf{P}}^0, \tag{133}$$

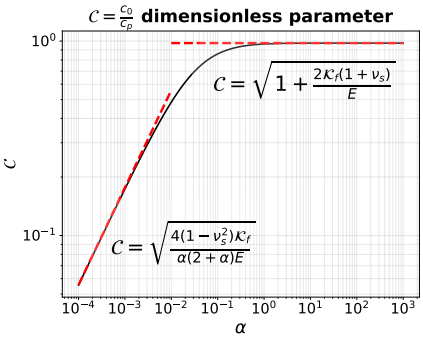

(a) Asymptotic behavior of $\mathcal{C} = \frac{c_0}{c_p}$

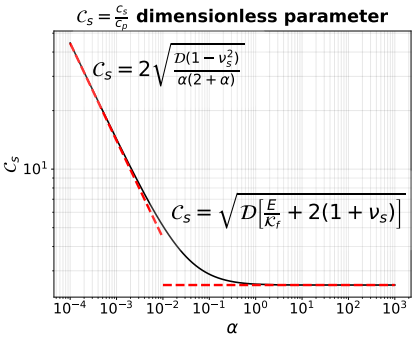

(b) Asymptotic behavior of $\mathcal{C}_s = \frac{c_s}{c_p}$

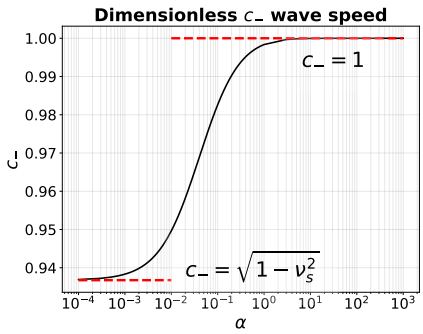

(c) Asymptotic behavior of c_-

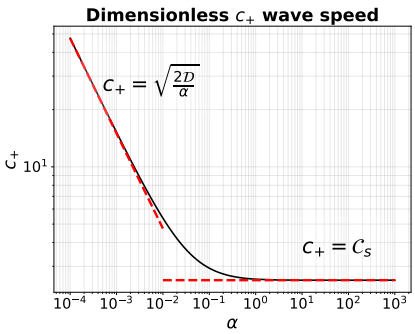

(d) Asymptotic behavior of c_+

Figure 3: α-dependence ($\alpha = \frac{e}{R_0}$) of the characteristic wave speeds of the (FSI) problem for $\nu_s = 0.35$ and $\mathcal{D} = 0.1122$, $\frac{E}{\mathcal{K}_f} = 54$. The red dashed lines provide information on the asymptotic behavior of the dimensionless wave speeds with respect to α.

where

$$\mathbf{E} = \frac{1}{2\nu_s}\begin{pmatrix} \left(1-(1-2\nu_s)\frac{\overline{c^2}-1}{\mathcal{C}_s^2}\right)\left(1+\frac{2\nu_s\mathcal{D}}{\alpha(2+\alpha)}\right) & \frac{2\nu_s\mathcal{D}(1-2\nu_s)}{\mathcal{C}_s^2}\left(1+\frac{2\nu_s\mathcal{D}}{\alpha(2+\alpha)}\right) \\ \left(1-(1-2\nu_s)\frac{\overline{c^2}-1}{\mathcal{C}_s^2}\right)\frac{\overline{c^2}-(1-2\nu_s)}{\alpha(2+\alpha)} & \frac{2\nu_s\mathcal{D}(1-2\nu_s)}{\mathcal{C}_s^2}\frac{\overline{c^2}-(1-2\nu_s)}{\alpha(2+\alpha)} \end{pmatrix}. \tag{134}$$

Supplementary details of this derivation are provided in Appendix Appendix E.

4. Pressure–stress wave equation solution and secularity condition

4.1. Leading– and first–order pressure–stress wave equations

The solutions to (132)-(133) are sought in the eigenvector basis of $\mathbf{C}_\mathbf{P}^2$, while eigenvalues of $\mathbf{C}_\mathbf{P}^2$ are defined in (128). Let us define $\mathbf{\Pi}$ the transition matrix from the canonical basis, $(\mathbf{e}_1, \mathbf{e}_2)$ to the eigenvector basis of $\mathbf{C}_\mathbf{P}^2$, $\boldsymbol{\mathcal{C}}_{\boldsymbol{\mathcal{P}}}^2$ the associated diagonal matrix, $\tilde{\boldsymbol{\mathcal{P}}}^0 = \left(\tilde{\mathcal{P}}_-^0, \tilde{\mathcal{P}}_+^0\right)$, $\tilde{\boldsymbol{\mathcal{P}}}^1 = \left(\tilde{\mathcal{P}}_-^1, \tilde{\mathcal{P}}_+^1\right)$ and $\boldsymbol{\mathcal{E}}$ respectively the expression of $\left(\tilde{\mathbf{P}}^0, \tilde{\mathbf{P}}^1\right)$ and $\mathbf{E}$ in the eigenvector basis. Then

$$\mathbf{\Pi} = \begin{pmatrix} \frac{2\nu_s\mathcal{D}}{c_-^2-1} & \frac{2\nu_s\mathcal{D}}{c_+^2-1} \\ 1 & 1 \end{pmatrix} \quad \& \quad \mathbf{\Pi}^{-1} = \frac{1}{\det(\mathbf{\Pi})}\begin{pmatrix} 1 & -\frac{2\nu_s\mathcal{D}}{c_+^2-1} \\ -1 & \frac{2\nu_s\mathcal{D}}{c_-^2-1} \end{pmatrix}, \tag{135}$$

$$\boldsymbol{\mathcal{C}}_{\boldsymbol{\mathcal{P}}}^2 = \mathbf{\Pi}^{-1}\cdot\mathbf{C}_\mathbf{P}^2\cdot\mathbf{\Pi} = \begin{pmatrix} c_-^2 & 0 \\ 0 & c_+^2 \end{pmatrix}, \tag{136}$$

$$\mathbf{E} = \mathbf{\Pi}^{-1}\cdot\boldsymbol{\mathcal{E}}\cdot\mathbf{\Pi}, \quad \tilde{\mathbf{P}}^0 = \mathbf{\Pi}\cdot\tilde{\boldsymbol{\mathcal{P}}}^0 \quad \& \quad \tilde{\mathbf{P}}^1 = \mathbf{\Pi}\cdot\tilde{\boldsymbol{\mathcal{P}}}^1. \tag{137}$$

Some additional elements regarding the axial boundary conditions, provided in §2.5, are now discussed. In the fluid, the downstream velocity variation (56), i.e. $W^0\big|_{Z=1} + \delta W^1\big|_{Z=1} = -H_{eav}(\tau)$, is equivalent, regarding the leading– and first–orders fluid momentum conservation equation (C.1), to impose Neumann condition on the pressure field, then yielding to

$$\partial_Z P^0\big|_{Z=1} = \delta(\tau) \quad \text{, and, } \quad \partial_Z P^1\big|_{Z=1} = 0, \tag{138}$$

where $\delta(\tau)$ is the Dirac distribution. Upstream, the homogeneous Dirichlet condition applied on the pressure trivially leads to

$$P^0\big|_{Z=0} = P^1\big|_{Z=0} = 0. \tag{139}$$

In the solid, the upstream and downstream homogeneous Dirichlet conditions (57), i.e. $\zeta^0\big|_{Z=0\&1} = \zeta^1\big|_{Z=0\&1} = 0$, are equivalent regarding (C.3) to

$$\partial_Z \sigma^0_{zz}\big|_{Z=0\&1} = 0 \ \text{ , and, } \ \partial_Z \sigma^1_{zz}\big|_{Z=0\&1} = -\frac{2}{\alpha(2+\alpha)} \tau^0_w\big|_{Z=0\&1}. \tag{140}$$

For the sake of simplicity and compactness let us introduce four 2×2 matrices $\boldsymbol{\mathcal{N}}$, $\boldsymbol{\mathcal{M}}$, $\boldsymbol{\mathcal{Q}}$, $\boldsymbol{\mathcal{R}}$. Boundary conditions in the diagonalization basis can formally be written as a rectangular 4×8 linear system

$$\begin{pmatrix} \boldsymbol{\mathcal{N}} & \boldsymbol{\mathcal{M}} & \mathbf{0} & \mathbf{0} \\ \mathbf{0} & \mathbf{0} & \boldsymbol{\mathcal{Q}} & \boldsymbol{\mathcal{R}} \end{pmatrix} \left[\begin{pmatrix} \tilde{\boldsymbol{\mathcal{P}}}^0\big|_{Z=0} \\ \partial_Z \tilde{\boldsymbol{\mathcal{P}}}^0\big|_{Z=0} \\ \tilde{\boldsymbol{\mathcal{P}}}^0\big|_{Z=1} \\ \partial_Z \tilde{\boldsymbol{\mathcal{P}}}^0\big|_{Z=1} \end{pmatrix} + \delta \begin{pmatrix} \tilde{\boldsymbol{\mathcal{P}}}^1\big|_{Z=0} \\ \partial_Z \tilde{\boldsymbol{\mathcal{P}}}^1\big|_{Z=0} \\ \tilde{\boldsymbol{\mathcal{P}}}^1\big|_{Z=1} \\ \partial_Z \tilde{\boldsymbol{\mathcal{P}}}^1\big|_{Z=1} \end{pmatrix} \right] =$$

$$\frac{\left(c_-^2-1\right)}{2\nu_s \mathcal{D}} \begin{pmatrix} 0 \\ 0 \\ 1 \\ 0 \end{pmatrix} + \delta \left(\frac{2}{\alpha(2+\alpha)\sqrt{s}} \begin{pmatrix} 0 \\ 0 \\ 0 \\ 1 \end{pmatrix} + \begin{pmatrix} \mathbf{0} & \boldsymbol{\mathcal{M}}\boldsymbol{\mathcal{N}} & \mathbf{0} & \mathbf{0} \\ \mathbf{0} & \mathbf{0} & \mathbf{0} & \mathbf{0} \end{pmatrix} \begin{pmatrix} \tilde{\boldsymbol{\mathcal{P}}}^0\big|_{Z=0} \\ \partial_Z \tilde{\boldsymbol{\mathcal{P}}}^0\big|_{Z=0} \\ \tilde{\boldsymbol{\mathcal{P}}}^0\big|_{Z=1} \\ \partial_Z \tilde{\boldsymbol{\mathcal{P}}}^0\big|_{Z=1} \end{pmatrix} \right), \tag{141}$$

where

$$\boldsymbol{\mathcal{N}} = \begin{pmatrix} 1 & \frac{c_-\beta}{c_+} \\ 0 & 0 \end{pmatrix}, \quad \boldsymbol{\mathcal{M}} = \begin{pmatrix} 0 & 0 \\ 1 & 1 \end{pmatrix}, \quad \boldsymbol{\mathcal{Q}} = \mathbf{0}, \quad \boldsymbol{\mathcal{R}} = \boldsymbol{\mathcal{N}} + \boldsymbol{\mathcal{M}}, \tag{142}$$

and

$$\beta = \frac{c_+\left(c_-^2-1\right)}{c_-\left(c_+^2-1\right)}. \tag{143}$$

In deriving (141), $\partial_Z \tilde{\tau}^0_w\big|_{Z=0\&1} = -\frac{1}{\sqrt{s}} \tilde{P}^0\big|_{Z=0\&1}$ has been used according to (121) and solid boundary conditions. Let us then define the operator $\mathcal{H}$ that acts on the square–integrable 2D–vector field $\boldsymbol{\Psi}(Z)$

$$\forall \boldsymbol{\Psi}(Z) \in L^2(\mathbb{R}) \times L^2(\mathbb{R}), \quad \boldsymbol{\Psi}(Z) \to \mathcal{H}\boldsymbol{\Psi}(Z) = \boldsymbol{\mathcal{C}}^2_{\boldsymbol{\mathcal{P}}} \cdot \partial_Z^2 \boldsymbol{\Psi}(Z), \tag{144}$$

with the following homogeneous associated set of spatial boundary conditions

$$\begin{pmatrix} \boldsymbol{\mathcal{N}} & \boldsymbol{\mathcal{M}} & \mathbf{0} & \mathbf{0} \\ \mathbf{0} & \mathbf{0} & \boldsymbol{\mathcal{Q}} & \boldsymbol{\mathcal{R}} \end{pmatrix} \cdot \begin{pmatrix} \boldsymbol{\Psi}(0) \\ \partial_Z \boldsymbol{\Psi}(0) \\ \boldsymbol{\Psi}(1) \\ \partial_Z \boldsymbol{\Psi}(1) \end{pmatrix} = \mathbf{0}. \tag{145}$$

The vector–wave equations system (132)&(133) then become

$$\left(s^2 - \mathcal{H}\right) \left(\tilde{\boldsymbol{\mathcal{P}}}^0 + \delta \tilde{\boldsymbol{\mathcal{P}}}^1\right) = -2s\delta \left[\partial_T + \sqrt{s}\boldsymbol{\mathcal{E}}\right] \tilde{\boldsymbol{\mathcal{P}}}^0. \tag{146}$$

4.2. Strategic decomposition of $\tilde{\boldsymbol{\mathcal{P}}}^0$ and $\tilde{\boldsymbol{\mathcal{P}}}^1$

Following Duhamel's principle, the vectors $\left(\tilde{\boldsymbol{\mathcal{P}}}^0, \tilde{\boldsymbol{\mathcal{P}}}^1\right)$ are split into homogeneous solutions $\left(\tilde{\boldsymbol{\mathcal{P}}}^0_h, \tilde{\boldsymbol{\mathcal{P}}}^1_h\right)$ (both having homogeneous boundary conditions) and particular ones $\left(\tilde{\boldsymbol{\mathcal{P}}}^0_p, \tilde{\boldsymbol{\mathcal{P}}}^1_p\right)$ taking care–off non–homogeneous boundary conditions. Both leading– and first–orders homogeneous components, $\tilde{\boldsymbol{\mathcal{P}}}^0_h$ and $\tilde{\boldsymbol{\mathcal{P}}}^1_h$, are then decomposed into the eigenvector orthonormal basis, $\boldsymbol{\Phi}_k(Z)$, of the operator $\mathcal{H}$

$$\tilde{\boldsymbol{\mathcal{P}}}^0(Z,s,T) = \sum_{\lambda_k \in \mathbb{R}} \tilde{a}^0_{\lambda_k}(s) A_{\lambda_k}(T) \boldsymbol{\Phi}_{\lambda_k}(Z) + \tilde{\boldsymbol{\mathcal{P}}}^0_p(Z,s), \tag{147}$$

$$\tilde{\boldsymbol{\mathcal{P}}}^1(Z,s) = \sum_{\lambda_k \in \mathbb{R}} \tilde{a}^1_{\lambda_k}(s) \boldsymbol{\Phi}_{\lambda_k}(Z) + \tilde{\boldsymbol{\mathcal{P}}}^1_p(Z,s), \tag{148}$$

where $A_{\lambda_k}(T)$ is for the long–time attenuation amplitude of each leading–order kth mode associated with $\mathcal{H}$'s eigenvalues, $-\lambda_k^2$. It is shown in Appendix F that the operator $\mathcal{H}$ is self–adjoint for the scalar product

$$\forall \boldsymbol{\Psi}, \boldsymbol{\Psi}^{'} \in L^2(\mathbb{R}) \times L^2(\mathbb{R}), \quad \langle \boldsymbol{\Psi}^{'}, \boldsymbol{\Psi} \rangle = \sum_{j=1}^{2} \eta_j \int_0^1 \Psi^{'}_j(Z) \Psi_j(Z) dZ, \tag{149}$$

with $\boldsymbol{\eta} \equiv [\eta_1, \eta_2] = [1, -\beta \left(c_-/c_+\right)^3]$ for a reservoir–pipe–anchored valve system, [33]. The eigenvectors $\boldsymbol{\Phi}_{\lambda_k}(Z)$ then constitute an orthogonal basis of $\mathcal{H}$. Note that (148) displays no dependence on the long–time scale T because $O(\delta T)$ corrections have been discarded. It is also interesting to mention that the choice for the particular solution $\tilde{\boldsymbol{\mathcal{P}}}^0_p(Z,s)$ is not unique even–though it has to fulfill the

prescribed non-homogeneous boundary conditions. The general solution in the RHS of (147) is thus adapted so as to provide the unique LHS $\tilde{\boldsymbol{\mathcal{P}}}^0(Z,s,T)$. The initial rest conditions of the unsteady fields along with the orthogonal behavior of $\boldsymbol{\Phi}_{\lambda_k}(Z)$ imposes

$$a_{\lambda_k}(0) = -\langle \boldsymbol{\mathcal{P}}_p^0(Z,0), \boldsymbol{\Phi}_{\lambda_k}(Z)\rangle \quad \& \quad \partial_\tau a_{\lambda_k}(0) = -\langle \partial_\tau \boldsymbol{\mathcal{P}}_p^0(Z,0), \boldsymbol{\Phi}_{\lambda_k}(Z)\rangle \quad (150)$$

The terms $\left(\tilde{\boldsymbol{\mathcal{P}}}_p^{\ 0}(Z,s), \tilde{\boldsymbol{\mathcal{P}}}_p^{\ 1}(Z,s)\right)$ are regarded as separated space–time variables functions

$$\tilde{\boldsymbol{\mathcal{P}}}_p^0(Z,s) \equiv \tilde{\boldsymbol{\mathcal{P}}}_p^0(Z) = \frac{Z}{\det(\boldsymbol{\Pi})}\begin{pmatrix}1\\-1\end{pmatrix}, \quad (151)$$

$$\tilde{\boldsymbol{\mathcal{P}}}_p^1(Z,s) = \frac{1}{\alpha(2+\alpha)\sqrt{s}}\left(\frac{Z^2}{1-\frac{c_+}{c_-\beta}}\begin{pmatrix}1\\-\frac{c_+}{c_-\beta}\end{pmatrix} - \frac{4\nu_s\mathcal{D}\left(\frac{Z^2}{2}-Z\right)}{c_-^2-1}\begin{pmatrix}1 & 0\\ 0 & \frac{c_-\beta}{c_+}\end{pmatrix}\partial_Z\tilde{\boldsymbol{\mathcal{P}}}^0|_{Z=0}\right) \quad (152)$$

the which are particular solutions for the boundary condition system (141). In the early–stage of the propagation, the fast–time τ is of order $O(1)$ such that $T \sim O(\delta)$ according to the slow–time definition (69). Thus, from a fast–time viewpoint, the attenuation function thereby remains at initial condition $A_{\lambda_k}(0) = 1$, set up to one, and leads to

$$A_{\lambda_k}(T) \equiv A_{\lambda_k}(\delta\tau) \approx 1, \quad \text{for,} \quad \tau \ll O\left(\frac{1}{\delta}\right), \text{i.e} \quad T \sim O(1). \quad (153)$$

This condition nevertheless holds as long as τ does not exceeds $O(1/\delta)$. In this limit, the attenuation plays an overcoming role, and a secularity condition is required to ensure consistency [49]. Then, this secularity condition, associated with the resonance condition of the $O(\delta)$ perturbations sets the long–time attenuation amplitude $A_{\lambda_k}(T)$, which is investigated next. Note that since $\boldsymbol{\mathcal{P}}^0$ is real, the LHS of (147) is also real when s is real from the definition of the Laplace transform (116). Hence the RHS of (147) is also real when s is real. Then, from the parity of $\boldsymbol{\Phi}_{\lambda_k} = \boldsymbol{\Phi}_{-\lambda_k}$ detailed in Appendix F, a conjugation of the amplitudes is required for each mode couple $(\lambda_k, -\lambda_k)$: $\tilde{a}^{0\star}_{\lambda_k} A^\star_{\lambda_k} = \tilde{a}^0_{-\lambda_k} A_{-\lambda_k}$ for real s. Furthermore, since this conjugate relation has to hold for every slow–time T and since at $T = 0$ $A_{\lambda_k}(0) = 1$, the conjugate condition extend to both $\tilde{a}^0_{\lambda_k}$ and A_{λ_k}, i.e., $\tilde{a}^{0\star}_{\lambda_k} = \tilde{a}^0_{-\lambda_k}$ for real s and $A^\star_{\lambda_k} = A_{-\lambda_k}$.

4.3. Solution for 2D–vector wave equation

4.3.1. Leading–order fast–time dependent amplitude $\tilde{a}^0_k(s)$

Combining $\tilde{\boldsymbol{\mathcal{P}}}^0(Z,s,T=0)$ (the $T=0$ is chosen according to condition (153)) in expression (147) with boundary conditions (150) into the constitutive vector-wave equation (146) leads to

$$\sum_{\lambda_k\in\mathbb{R}}\left(s^2-\mathcal{H}\right)\tilde{a}^0_{\lambda_k}(s)\boldsymbol{\Phi}_{\lambda_k}(Z)=-s^2\tilde{\boldsymbol{\mathcal{P}}}^0_p(Z). \tag{154}$$

Using (F.4), the orthogonality of the eigenfunction basis as well as its symmetry $\boldsymbol{\Phi}_{\lambda_k}=\boldsymbol{\Phi}_{-\lambda_k}$, one obtains the following

$$\tilde{a}^0_{\lambda_k}(s)+\tilde{a}^0_{-\lambda_k}(s)=\left[\frac{\lambda_k}{2i}\left(\frac{1}{s-i\lambda_k}-\frac{1}{s+i\lambda_k}\right)-1\right]\langle\tilde{\boldsymbol{\mathcal{P}}}^0_p(Z),\boldsymbol{\Phi}_{\lambda_k}(Z)\rangle. \tag{155}$$

An identification using the conjugate relation $\tilde{a}^{0\star}_{\lambda_k}=\tilde{a}^0_{-\lambda_k}$ (for real s) discussed above, thus leads to the following (note that this identification is not unique up to irrelevant odd functions of λ_k, canceling out in the mode summation)

$$\tilde{a}^0_{\pm\lambda_k}(s)=-\frac{1}{2}\left[\frac{\pm i\lambda_k}{s\mp i\lambda_k}+1\right]\langle\tilde{\boldsymbol{\mathcal{P}}}^0_p(Z),\boldsymbol{\Phi}_{\lambda_k}(Z)\rangle. \tag{156}$$

Finally re–injecting the $\tilde{a}^0_{\lambda_k}(s)$ found in (156) within the Laplace transform in (147) gives the following

$$\tilde{\boldsymbol{\mathcal{P}}}^0(Z,s,T)=\tilde{\boldsymbol{\mathcal{P}}}^0_p(Z)-\sum_{\lambda_k\in\mathbb{R}}\frac{A_{\lambda_k}(T)}{2}\left[\frac{i\lambda_k}{s-i\lambda_k}+1\right]\langle\tilde{\boldsymbol{\mathcal{P}}}^0_p(Z),\boldsymbol{\Phi}_{\lambda_k}(Z)\rangle\boldsymbol{\Phi}_{\lambda_k}(Z) \tag{157}$$

At this stage, the attenuation $A_{\lambda_k}(T)$ remains the only unknown.

4.3.2. First–order coupled wave equation and secularity condition

Next, let us combine the Laplace splitting form of $\tilde{\boldsymbol{\mathcal{P}}}^1(Z,s)$ in (148) within the first–order constitutive vector–wave equation (146). Regarding the derived expression of $\tilde{\boldsymbol{\mathcal{P}}}^0$ in (157), it then yields the following

$$\begin{aligned}\sum_{\lambda_k\in\mathbb{R}}\left(s^2+\lambda_k^2\right)\tilde{a}^1_{\lambda_k}(s)\boldsymbol{\Phi}_{\lambda_k}(Z)&=-\left(s^2-\mathcal{H}\right)\tilde{\boldsymbol{\mathcal{P}}}^1_p(Z,s)-2s\sqrt{s}\boldsymbol{\mathcal{E}}\tilde{\boldsymbol{\mathcal{P}}}^0_p(Z,s)\\&+s\sum_{\lambda_k\in\mathbb{R}}\left[\partial_T+\sqrt{s}\boldsymbol{\mathcal{E}}\right]A_{\lambda_k}(T)\left[\frac{i\lambda_k}{s-i\lambda_k}+1\right]\langle\tilde{\boldsymbol{\mathcal{P}}}^0_p(Z,s),\boldsymbol{\Phi}_{\lambda_k}(Z)\rangle\boldsymbol{\Phi}_{\lambda_k}(Z).\end{aligned} \tag{158}$$

A complete derivation of $\left(s^2-\mathcal{H}\right)\tilde{\boldsymbol{\mathcal{P}}}_p^1(Z,s)$ have been carried out in Appendix G, and is not repeated here. From the orthogonality of $\boldsymbol{\Phi}_{\lambda_k}(Z)$, one finds the following

$$\begin{aligned}
\tilde{a}^1_{\lambda_k}(s)+\tilde{a}^1_{-\lambda_k}(s) &= is\lambda_k\frac{\langle\tilde{\boldsymbol{\mathcal{P}}}_p^0(Z,s),\boldsymbol{\Phi}_{\lambda_k}(Z)\rangle}{(s+i\lambda_k)\,(s-i\lambda_k)^2}\left[\partial_T+\sqrt{s}\langle\boldsymbol{\mathcal{E}}\boldsymbol{\Phi}_{\lambda_k}(Z)-\frac{\boldsymbol{\mathcal{J}}_{\lambda_k}(Z,s)}{s^2},\boldsymbol{\Phi}_{\lambda_k}(Z)\rangle\right]A_{\lambda_k}(T)\\
&\quad-is\lambda_k\frac{\langle\tilde{\boldsymbol{\mathcal{P}}}_p^0(Z,s),\boldsymbol{\Phi}_{\lambda_k}(Z)\rangle}{(s-i\lambda_k)\,(s+i\lambda_k)^2}\left[\partial_T+\sqrt{s}\langle\boldsymbol{\mathcal{E}}\boldsymbol{\Phi}_{\lambda_k}(Z)-\frac{\boldsymbol{\mathcal{J}}_{\lambda_k}(Z,s)}{s^2},\boldsymbol{\Phi}_{\lambda_k}(Z)\rangle\right]A_{-\lambda_k}(T)\\
&-2s\sqrt{s}\frac{\langle\boldsymbol{\mathcal{E}}\tilde{\boldsymbol{\mathcal{P}}}_p^0(Z,s),\boldsymbol{\Phi}_{\lambda_k}(Z)\rangle}{s^2+\lambda_k^2}+s\left[\partial_T+\sqrt{s}\langle\boldsymbol{\mathcal{E}}\boldsymbol{\Phi}_{\lambda_k}(Z),\boldsymbol{\Phi}_{\lambda_k}(Z)\rangle\right]\left(A_{\lambda_k}(T)+A_{-\lambda_k}(T)\right)\frac{\langle\tilde{\boldsymbol{\mathcal{P}}}_p^0(Z,s),\boldsymbol{\Phi}_{\lambda_k}(Z)\rangle}{s^2+\lambda_k^2}\\
&\quad+s\sqrt{s}\sum_{\lambda_j\in\mathbb{R}\setminus\{-\lambda_k,\lambda_k\}}\left[\frac{i\lambda_j}{s-i\lambda_j}+1\right]\frac{\langle\tilde{\boldsymbol{\mathcal{P}}}_p^0(Z,s),\boldsymbol{\Phi}_{\lambda_j}(Z)\rangle\langle\boldsymbol{\mathcal{E}}\boldsymbol{\Phi}_{\lambda_j}(Z),\boldsymbol{\Phi}_{\lambda_k}(Z)\rangle}{(s-i\lambda_k)\,(s+i\lambda_k)}A_{\lambda_j}(T)\\
&-\frac{1}{\alpha(2+\alpha)\sqrt{s}\left(s^2+\lambda_k^2\right)}\langle\frac{s^2Z^2-2\mathcal{C}^2_{\boldsymbol{\mathcal{P}}}}{1-\frac{c_+}{c_-\beta}}\begin{pmatrix}1\\-\frac{c_+}{c_-\beta}\end{pmatrix}-\frac{s^2\left(Z^2-2Z\right)-2\mathcal{C}^2_{\boldsymbol{\mathcal{P}}}}{1-\frac{c_-\beta}{c_+}}\begin{pmatrix}1\\-\frac{c_-\beta}{c_+}\end{pmatrix},\boldsymbol{\Phi}_{\lambda_k}(Z)\rangle\\
&\quad-\sum_{\lambda_j\in\mathbb{R}\setminus\{-\lambda_k,\lambda_k\}}i\lambda_j\frac{\langle\tilde{\boldsymbol{\mathcal{P}}}_p^0(Z),\boldsymbol{\Phi}_{\lambda_j}(Z)\rangle\langle\boldsymbol{\mathcal{J}}_{\lambda_j}(Z,s),\boldsymbol{\Phi}_{\lambda_k}(Z)\rangle}{\sqrt{s}\,(s-i\lambda_j)\,(s-i\lambda_k)\,(s+i\lambda_k)}A_{\lambda_j}(T)\\
&\quad-\sum_{\lambda_j\in\mathbb{R}}\frac{\langle\tilde{\boldsymbol{\mathcal{P}}}_p^0(Z),\boldsymbol{\Phi}_{\lambda_j}(Z)\rangle\langle\boldsymbol{\mathcal{J}}_{\lambda_j}(s,Z),\boldsymbol{\Phi}_{\lambda_k}(Z)\rangle}{\sqrt{s}\,(s-i\lambda_k)\,(s+i\lambda_k)}A_{\lambda_j}(T),
\end{aligned}\tag{159}$$

with

$$\boldsymbol{\mathcal{J}}_{\lambda_k}(Z,s)=\frac{\lambda_k}{\alpha(2+\alpha)\left(1-\frac{c_-\beta}{c_+}\right)}\begin{pmatrix}\left(s^2\left(\frac{Z^2}{2}-Z\right)-c_-^2\right)\frac{\tan\left(\frac{\lambda_k}{c_-}\right)}{c_-}\\-\left(s^2\left(\frac{Z^2}{2}-Z\right)-c_+^2\right)\frac{\tan\left(\frac{\lambda_k}{c_+}\right)}{c_+}\end{pmatrix},\tag{160}$$

an even function of λ_k. The secularity contribution lies in every double–pole found in the RHS terms of $\tilde{a}^1_{\lambda_k}(s)$. These double–poles are associated with resonance conditions between the (158)'s RHS and the natural frequencies of the (158)'s LHS, i.e. $(s\pm i\lambda_k)^2$. These resonance conditions produce a linear divergence term upon the fast time τ of $\tilde{a}^1_{\lambda_k}(s)$, as found from the inverse Laplace transform of the double poles in (159), through Cauchy's residue theorem

$$\mathcal{L}^{-1}\left(\frac{1}{(s\pm i\lambda_k)^2}\right)(\tau)=\lim_{s\to\pm i\lambda_k}\left(\partial_s e^{s\tau}\right)=\tau e^{\pm i\lambda_k\tau}.\tag{161}$$

When τ reaches $O(1/\delta)$, the asymptotic approximation collapses since assumption (153) vanishes. To prevent it, the attenuation function is built to cancel the divergent double–pole contributions. In (159), double–poles are gathered within the two first RHS terms since $\lambda_j\neq\pm\lambda_k$. The secularity condition there-

fore reads as follows

$$\lim_{s\to\pm i\lambda_k}\left(\partial_T+\sqrt{s}\langle\boldsymbol{\mathcal{E}}\boldsymbol{\Phi}_{\lambda_k}(Z)-\frac{\boldsymbol{\mathcal{J}}_{\lambda_k}(Z,s)}{s^2},\boldsymbol{\Phi}_{\lambda_k}(Z)\rangle\right)A_{\pm\lambda_k}(T)=0, \tag{162}$$

361 leading to

$$A_{\lambda_k}(T) = e^{-\sqrt{i\lambda_k}\frac{T}{\mathcal{T}_{\lambda_k}}}, \tag{163}$$

$$\mathcal{T}_{\lambda_k}^{-1} = \langle\boldsymbol{\mathcal{E}}\boldsymbol{\Phi}_{\lambda_k}(Z)+\frac{\boldsymbol{\mathcal{J}}_{\lambda_k}(s=i\lambda_k,Z)}{\lambda_k^2},\boldsymbol{\Phi}_{\lambda_k}(Z)\rangle, \tag{164}$$

$$\boldsymbol{\mathcal{J}}_{\lambda_k}(Z,s=i\lambda_k)=\frac{\lambda_k}{\alpha(2+\alpha)\left(1-\frac{c_-\beta}{c_+}\right)}\begin{pmatrix}-\left(\left(\frac{Z^2}{2}-Z\right)+\left(\frac{c_-}{\lambda_k}\right)^2\right)\frac{\tan\left(\frac{\lambda_k}{c_-}\right)}{c_-}\\ \left(\left(\frac{Z^2}{2}-Z\right)+\left(\frac{c_+}{\lambda_k}\right)^2\right)\frac{\tan\left(\frac{\lambda_k}{c_+}\right)}{c_+}\end{pmatrix}. \tag{165}$$

An explicit expression of the envelope slow–time decay $\mathcal{T}_{\lambda_k}$ is provided in Appendix H. Result (164) for the deviation of our prediction from [41] given by $\mathcal{T}_{\lambda_k}$ shows that this deviation results from the interaction between (FSI) vibrations modes and dissipation. More precisely this term is the projection of vector $\boldsymbol{\mathcal{E}}\boldsymbol{\Phi}_{\lambda_k}(Z)+\frac{\boldsymbol{\mathcal{J}}_{\lambda_k}(s=i\lambda_k,Z)}{\lambda_k^2}$ which results from wall shear rate longitudinal gradient on each (FSI) modes. Note that with the conjugation conditions $A^{\star}_{\lambda_k}=A_{-\lambda_k}$ is verified. In the Laplace domain, the leading–order vector $\tilde{\boldsymbol{\mathcal{P}}}^0$ is now fully established. Combining the previous expression of $A_{\lambda_k}(T)$ within $\tilde{\boldsymbol{\mathcal{P}}}^0$ in (157) leads to the following

$$\tilde{\boldsymbol{\mathcal{P}}}^0(Z,s,T)=\tilde{\boldsymbol{\mathcal{P}}}^0_p(Z,s)-\frac{1}{2}\sum_{\lambda_k\in\mathbb{R}}e^{-\sqrt{i\lambda_k}\frac{T}{\mathcal{T}_{\lambda_k}}}\left[\frac{i\lambda_k}{s-i\lambda_k}+1\right]\langle\tilde{\boldsymbol{\mathcal{P}}}^0_p(Z,s),\boldsymbol{\Phi}_{\lambda_k}(Z)\rangle\boldsymbol{\Phi}_{\lambda_k}(Z) \tag{166}$$

362 As often required, the space–time solution associated with the previous expres-
363 sion could be deduced by performing an inverse Laplace transform.

364 *4.3.3. Laplace inversion and time–dependent solution*

The particular part of $\tilde{\boldsymbol{\mathcal{P}}}^0$, $\tilde{\boldsymbol{\mathcal{P}}}^0_p$ for the hereby reservoir–pipe–anchored valve system examined here under impulse disturbance, does not depend on s as found in (151). The inverse Laplace transform of (166) then becomes

$$\begin{aligned}\boldsymbol{\mathcal{P}}^0(Z,\tau,T)=\boldsymbol{\mathcal{P}}^0_p(Z)&-\frac{1}{2}\sum_{\lambda_k\in\mathbb{R}}e^{-\sqrt{i\lambda_k}\frac{T}{\mathcal{T}_{\lambda_k}}}\langle\boldsymbol{\mathcal{P}}^0_p(Z),\boldsymbol{\Phi}_{\lambda_k}(Z)\rangle\boldsymbol{\Phi}_{\lambda_k}(Z)\\&+\frac{1}{2i}\sum_{\lambda_k\in\mathbb{R}}\lambda_k\boldsymbol{\Phi}_{\lambda_k}(Z)\mathcal{L}^{-1}\left(\frac{e^{-\sqrt{i\lambda_k}\frac{T}{\mathcal{T}_{\lambda_k}}}}{s-i\lambda_k}\right)(\tau)\langle\boldsymbol{\mathcal{P}}^0_p(Z),\boldsymbol{\Phi}_{\lambda_k}(Z)\rangle.\end{aligned} \tag{167}$$

Applying Cauchy's residue theorem yields the following

$$\mathcal{L}^{-1}\left(\frac{e^{-\sqrt{i\lambda_k}\frac{T}{\mathcal{T}_{\lambda_k}}}}{s-i\lambda_k}\right)=e^{i\lambda_k\tau-\sqrt{i\lambda_k}\frac{T}{\mathcal{T}_{\lambda_k}}}. \tag{168}$$

Using notation $\mathrm{sgn}(\lambda_k)$ for the sign of λ_k, (i.e. $\lambda_k=\mathrm{sgn}(\lambda_k)|\lambda_k|$) and since $\sqrt{i\,\mathrm{sgn}(\lambda_k)|\lambda_k|}=(1+\mathrm{sgn}(\lambda_k)i)\sqrt{\frac{|\lambda_k|}{2}}$, (168) results by symmetry

$$\boldsymbol{\mathcal{P}}^0(Z,\tau,T)=\boldsymbol{\mathcal{P}}^0_p(Z)-\sum_{\lambda_k\in\mathcal{S}_p}e^{-\sqrt{\frac{\lambda_k}{2}}\frac{T}{\mathcal{T}_{\lambda_k}}}\cos\left(\sqrt{\frac{\lambda_k}{2}}\frac{T}{\mathcal{T}_{\lambda_k}}\right)\langle\boldsymbol{\mathcal{P}}^0_p(Z),\boldsymbol{\Phi}_{\lambda_k}(Z)\rangle\boldsymbol{\Phi}_{\lambda_k}(Z)$$
$$+\sum_{\lambda_k\in\mathcal{S}_p}\lambda_k e^{-\sqrt{\frac{\lambda_k}{2}}\frac{T}{\mathcal{T}_{\lambda_k}}}\boldsymbol{\Phi}_{\lambda_k}(Z)\sin\left(\lambda_k\tau-\sqrt{\frac{\lambda_k}{2}}\frac{T}{\mathcal{T}_{\lambda_k}}\right)\langle\boldsymbol{\mathcal{P}}^0_p(Z),\boldsymbol{\Phi}_{\lambda_k}(Z)\rangle, \tag{169}$$

Here $\mathcal{S}_p$ is the operator $\mathcal{H}$'s discrete spectrum introduced in (F.7). The leading–order pressure–stress vector $\mathbf{P}^0(Z,\tau,T)$ falls from basis change relationships (137). The wall shear stress τ^0_w, through combining of (122), (C.1), (C.3) and (151), achieves the following

$$\tau^0_w(Z,\tau,T)=-\frac{\boldsymbol{\mathcal{D}}\left[\begin{pmatrix}1\\-1\end{pmatrix}\right]}{\det(\boldsymbol{\Pi})\sqrt{\pi\tau}}$$
$$+\sum_{\lambda_k\in\mathcal{S}_p}e^{-\sqrt{\frac{\lambda_k}{2}}\frac{T}{\mathcal{T}_{\lambda_k}}}\left[\sqrt{2\lambda_k}b_{\lambda_k}(\tau,T)+\frac{\cos\left(\sqrt{\frac{\lambda_k}{2}}\frac{T}{\mathcal{T}_{\lambda_k}}\right)}{\sqrt{\pi\tau}}\right]\frac{\langle Z\begin{pmatrix}1\\-1\end{pmatrix},\boldsymbol{\Phi}_{\lambda_k}(Z)\rangle\boldsymbol{\mathcal{D}}\left[\partial_Z\boldsymbol{\Phi}_{\lambda_k}(Z)\right]}{\det(\boldsymbol{\Pi})}, \tag{170}$$

where,

$$\boldsymbol{\mathcal{D}}[\boldsymbol{\mathcal{X}}] = \left(\begin{pmatrix}1&\mathcal{D}\\1&\mathcal{D}\end{pmatrix}\boldsymbol{\Pi}\boldsymbol{\mathcal{X}}\right)\cdot\begin{pmatrix}1\\0\end{pmatrix} \tag{171}$$

$$b_{\lambda_k} = \cos\left(\lambda_k\tau-\sqrt{\frac{\lambda_k}{2}}\frac{T}{\mathcal{T}_{\lambda_k}}\right)\mathcal{F}_s\left(t_{\lambda_k}\right)-\sin\left(\lambda_k\tau-\sqrt{\frac{\lambda_k}{2}}\frac{T}{\mathcal{T}_{\lambda_k}}\right)\mathcal{F}_c\left(t_{\lambda_k}\right). \tag{172}$$

Here, $\mathcal{F}_s$, $\mathcal{F}_c$ are the sine and cosine Fresnel functions, respectively, and $t_{\lambda_k}=\sqrt{\frac{2\lambda_k\tau}{\pi}}$.

5. Comparison with experiments and previous theories ignoring FSI

In this section various quantities are compared with previous theoretical predictions ignoring (FSI) and with experimental observations. All geometrical and physical properties from experimental articles are provided in Table 2. A reservoir–pipe–anchored valve system has been studied by [41, 42], but they

did not consider (FSI), so an analytical expression for the pressure field and its spectrum has been found

$$P = 2\sum_{k\in\mathbb{N}}(-1)^k \frac{\sin(\lambda_k Z)}{\lambda_k} e^{-\sqrt{\frac{\lambda_k}{2}}T} \sin\left(\lambda_k \tau - \sqrt{\frac{\lambda_k}{2}}T\right) \quad \& \quad \lambda_k = \pi\left(\frac{1}{2}+k\right). \tag{173}$$

Noteworthy, in the $\nu_s \to 0$ limit and for the impulse response, the predicted pressure attenuation in (169) reaches that found by Mei & Jing [41, 42], which is given in (173), since $\mathcal{T}_{\lambda_k}^{-1} = 1$ (as $\nu_s \to 0$, $\boldsymbol{\mathcal{E}} \to \mathbf{I}$ and $\boldsymbol{\mathcal{J}}_{\lambda_k}(s = i\lambda_k) \to 0$, whilst the eigenmodes are orthogonal). The pressure signature is compared at

Table 2: Physical and geometrical properties for the analysis of the reservoir pipe anchored valve system. (*) refers to unavailable data in the original article. They were estimated by the authors based up available properties of pure copper tube and water.

Article	**Density** $(kg\cdot m^{-3})$	**Elasticity** $(10^9 Pa)$	ν_f $(m^2\cdot s^{-1})$	ν_s	**Geometry** (m)
[47]	$\rho^\star_{f_0} = 998.3$ $\rho^\star_{s_0} = 8935.0$	$\mathcal{K}^\star_f = 2.1$ $E^\star = 127.0$	$3.967\cdot 10^{-5}$	$0.34^\star$	$R = 0.0127$ $e = 0.001651$ $L = 36.088$
[38]	$\rho_{f_0} = 1000.0$ $\rho_{s_0} = 8890.0$	$\mathcal{K}_f = 2.1$ $E = 120.0$	$9.493\cdot 10.0^{-7.0}$	0.35	$R = 0.008$ $e = 0.001$ $L = 98.11$
[37]	$\rho^\star_{f_0} = 1000.0$ $\rho^\star_{s_0} = 8960.0$	$\mathcal{K}^\star_f = 2.1$ $E^\star = 130.0$	$1.182\cdot 10^{-6.0}$	$0.3^\star$	$R = 0.01105$ $e = 0.00163$ $L = 37.23$
[56]	$\rho^\star_{f_0} = 1000.0$ $\rho^\star_{s_0} = 8960.0$	$\mathcal{K}^\star_f = 2.1$ $E^\star = 130.0$	$10^{-6.0}$	$0.3^\star$	$R = 0.01$ $e = 0.001$ $L = 15.22$

different locations in Figure 4 from [38]'s data set. The special case $\nu_s \to 0$ or that of [41] is again depicted. Each analytical solutions exhibits excellent agreement for both amplitude and phase for every considered pipe's locations with experimental observations. No parameter fit is used.

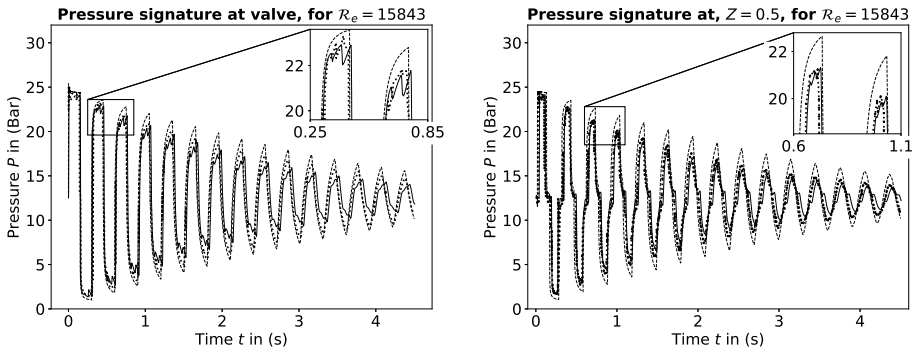

(a) (b)

Figure 4: Pressure signature compared with experimental data of [38]. Experimental data are depicted with black dotted lines while theoretical results from (169) are depicted with continuous lines. [41]'s solution (no-FSI) is provided with dashed line. Dimensionless numbers are $\mathcal{M} = 7.2 \cdot 10^{-4}$, $\epsilon = 8.2 \cdot 10^{-5}$, $\alpha = 0.125$, $\delta = 3.3 \cdot 10^{-2}$ and $\mathcal{D} = 0.11$. Neither tuned nor fitted parameters have been used.

The variety of observed patterns of the pressure signal depicted in Figure 4 and the surprisingly precise predictions provided by the theory results from the complex mode decomposition $\mathbf{\Phi}_{\lambda_k}(Z)$, each with its own phase. In Figure (4a), a deeper analysis of the pressure signature reveals that [41]'s theory leads to a better agreement with experimental data in the early times, i.e. $\tau \ll O(1/\delta)$. At longer times, both models correctly describe the attenuation, [41]'s theory under–attenuating, whist the hereby developed one slightly over–attenuating. In Figure (4b) however, the present analysis shows excellent agreement with experimental data at long time, [41]'s theory again under–attenuating. It is worth noting that these differences are minor in both configurations as the (FSI) coupling has little influences in these experimental data set.

To deepen the analysis of the new prediction for (FSI) damping, Figures (5a)–(5d) then focus on the damping envelope of the first exponential mode. A comparison with four sets of experiments is provided. For each experiment, the pressure of the envelope peaks are extracted, non–dimensionalized, and compared with the theoretical damping trend. Figures (5a)–(5d) reveal as

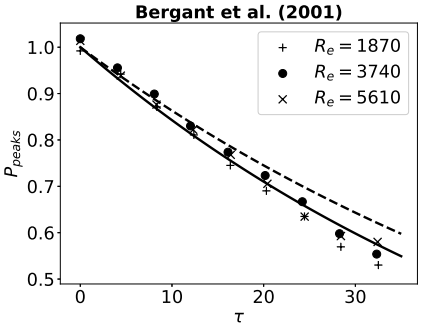

(a) $\mathcal{M} = [7.65^{(+)}, 15.3^{(\bullet)}, 23^{(\times)}] \cdot 10^{-5}$, $\epsilon = 3 \cdot 10^{-4}$, $\alpha = 0.146$, $\delta = 1.7 \cdot 10^{-2}$

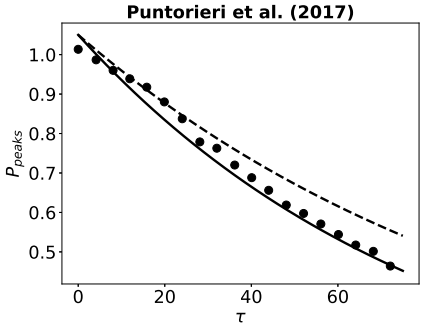

(b) $\mathcal{M} = 1.53 \cdot 10^{-4}$, $\epsilon = 6.57 \cdot 10^{-4}$, $\alpha = 0.1$, $\delta = 1.1 \cdot 10^{-2}$

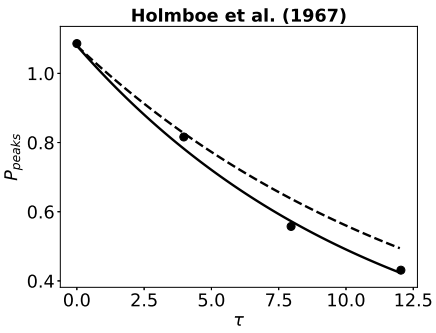

(c) $\mathcal{M} = 1.88 \cdot 10^{-4}$, $\epsilon = 3.5 \cdot 10^{-4}$, $\alpha = 0.13$, $\delta = 8.2 \cdot 10^{-2}$

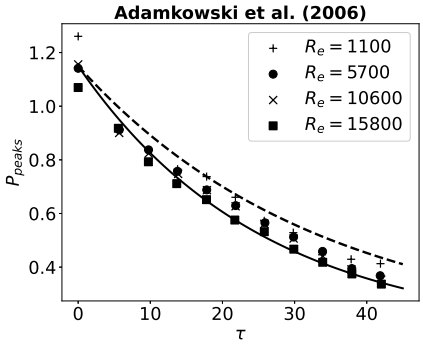

(d) $\mathcal{M} = [5.05^{(+)}, 26.0^{(\bullet)}, 48.3^{(\times)}, 72.0^{(\blacksquare)}] \cdot 10^{-5}$, $\epsilon = 8.2 \cdot 10^{-5}$, $\alpha = 0.125$, $\delta = 3.3 \cdot 10^{-2}$

Figure 5: First exponential damping mode (continuous and dotted lines) comparison with experimental dimensionless pressure peaks, P_{peaks} (crosses, bullet and rectangular symbols). The present theory is depicted with a continuous line while [41]'s theory ($\nu_s \to 0$) is depicted by a dashed line.

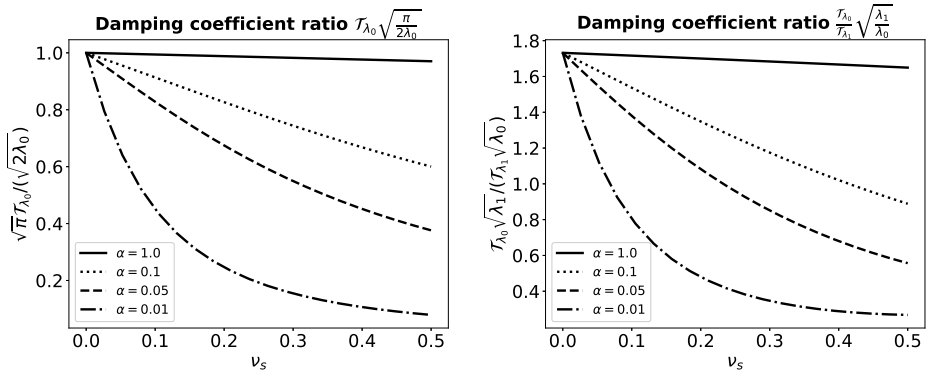

(a) (b)

Figure 6: Exponential damping coefficient analysis: (a) Analysis of $\mathcal{T}_0\sqrt{\frac{\pi}{2\lambda_0}}$, (b) Analysis of $\frac{\mathcal{T}_0}{\mathcal{T}_1}\sqrt{\frac{\lambda_1}{\lambda_0}}$. Iso–$\alpha$ lines are represented based on [38]'s data from Table 2.

very good agreement between the predictions and experiments for laminar and transitional Reynolds numbers. As the first mode damping is dominant over others at long time, the match between predictions and observations becomes better with time, as expected. Furthermore, to more accurately quantify how much this preferential damping dominates others, Figure (6a) and (7a) depict and compare the ratio of [41] first damping mode (i.e. $\sqrt{\pi/4}$) with the present asymptotic theory (i.e. $\sqrt{\lambda_0}/\sqrt{2}\mathcal{T}_{\lambda_0}$) for a various set of iso–α and iso–E. This ratio appears to be less than unity within the entire ν_s range between zero and one–half, which demonstrates that (FSI) liquid–filled pipe systems attenuate faster than those where no–(FSI) is considered, which is an expected effect. It is also interesting to note that the thinner the pipe (i.e. the lower the α), the stronger the damping, which is also expected due to the increasing importance of (FSI) effects in thin–shell. In Figure (6b) and (7b), the ratio of the second to first exponential damping rate (i.e. $\frac{\mathcal{T}_{\lambda_0}}{\mathcal{T}_{\lambda_1}}\sqrt{\frac{\lambda_1}{\lambda_0}}$) is analyzed. Whereas no–(FSI) modes gradually attenuate, liquid–filled pipe systems that incorporate (FSI) do not necessarily follow this pattern. Depending on the dimensionless numbers' relative values, the second attenuation mode could attenuates slower than the first, possibly leading to a distinct long–time behavior. This can be

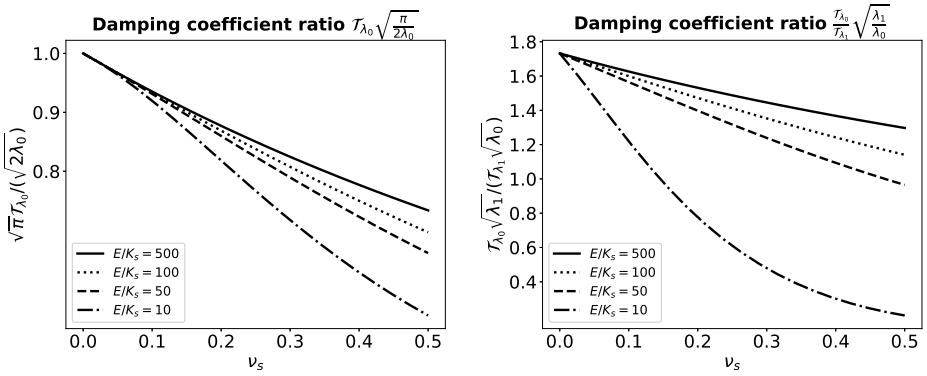

(a) (b)

Figure 7: Exponential damping coefficient analysis: (a) Analysis of $\mathcal{T}_0\sqrt{\frac{\pi}{2\lambda_0}}$, (b) Analysis of $\frac{\mathcal{T}_0}{\mathcal{T}_1}\sqrt{\frac{\lambda_1}{\lambda_0}}$. Iso–$E$ lines are represented based on [38]'s data from Table 2.

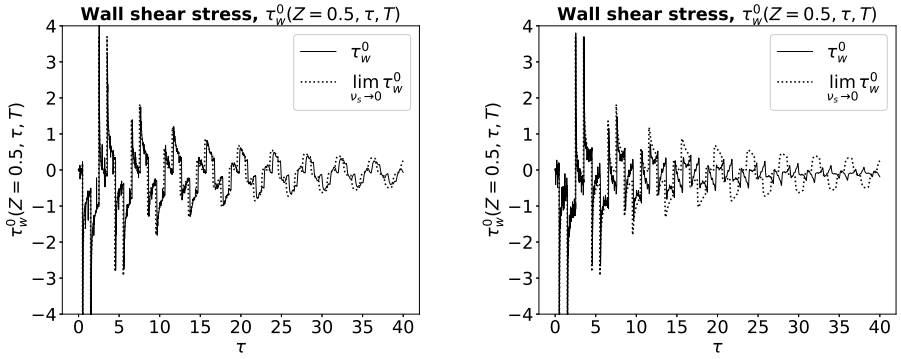

(a) $\alpha = 0.125$, $\mathcal{D} = 0.11$ (b) $\alpha = 0.125$, $\mathcal{D} = 1$

Figure 8: Dimensionless fluid wall shear stress τ_w^0 at middle's pipe location. [38]'s data from Table 2 are used with (a) unmodified density ratio $\mathcal{D}$, (b) modified density ratio $\mathcal{D} = 1$.

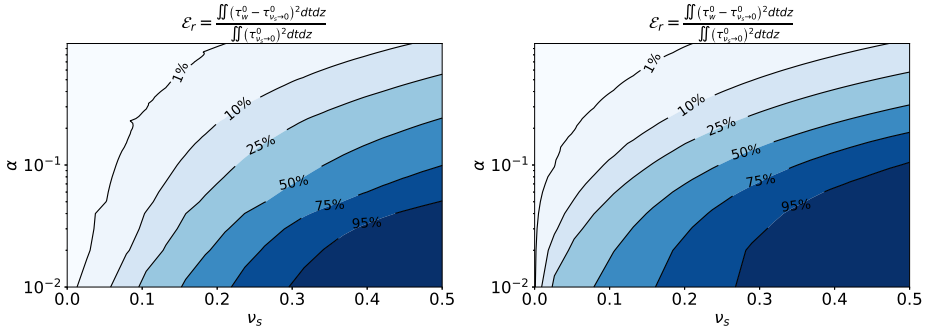

(a) $\mathcal{D} = 0.11$ (b) $\mathcal{D} = 1$

Figure 9: Relative difference $\mathcal{E}_r$ between (FSI) and no–(FSI) ($\nu_s \to 0$) fluid wall shear rate. [38]'s data from Table 2 are used with (a) unmodified density ratio $\mathcal{D}$, (b) modified density ratio $\mathcal{D} = 1$.

observed for the chosen parameters in Figure (6b) and (7b) when the computed ratio is smaller than one for increasing ν_s values; thus, in this special case, the second mode drives the long–time dynamics. For extremely thin tubes (i.e. $\alpha \sim 10^{-2}$), lying within a shell theory framework, such behaviors should therefore be expected.

The wall shear stress (170) is provided in Figure 8 and 9 using [38]'s experimental parameters. The solution in the $\nu_s \to 0$ limit is again depicted to illustrate the possible contribution of the solid axial displacement acceleration in the convolution term (121), i.e. $\partial_\tau[W - \alpha\dot{\zeta}]$. Since Figure 8 and 9 consider the wall shear stress under impulse disturbance, one can observe the successive peaks associated with the back–and–forth pulse propagating wave at a given position. Obviously, these peaks should be smoothed by convolution with the applied valve closure law for non–impulse disturbances. The observed difference between the (FSI) wall shear stress and the one computed without including (FSI) effects are rising with time, but also increasing for larger density ratio $\mathcal{D}$. This difference is systematically investigated in Figure (9a) and (9b) where the influence of the thickness of the tube wall and the Poisson coefficient are provided. These plots permit to realize that the prediction of the (FSI) wall shear stress differ by a factor two or more from the one omitting (FSI), for ν_s

larger than 0.25 for usual relative wall thickness (i.e. $\alpha < 0.1$). From this, one can infer that this very important quantity in the blood–hammer context (for which $\mathcal{D} \approx 1$, $\alpha \in [0.05 - 0.2]$, $\nu_s \in [0.45 - 0.5]$) deserves to be examined from an (FSI) viewpoint. Since many studies have demonstrated the importance of the wall shear stress in bio–mechanics (e.g., [57]) this theoretical prediction is thus worth considering.

Conclusion

This contribution investigates a low–Mach number theory of (FSI) pulsed waves in a pipe. The asymptotic analysis includes three small parameters, namely the dimensionless viscous boundary layer thickness $\delta = 1/\sqrt{\epsilon Re_p}$, the Mach number $\mathcal{M}$, and the tube aspect ratio ϵ, which are chosen within the framework of $\delta^2 \gg \mathcal{M},\ \delta \gg \epsilon^2,\ \delta \gg \alpha\mathcal{M}$ (or equivalently $1/Re_p \gg \max\left(\epsilon\mathcal{M}, \epsilon^5, \alpha^2\epsilon\mathcal{M}^2\right)$) and $1 \gg \epsilon \gg \alpha\mathcal{M}$, consistent with the parameter ranges of many relevant studies. The resulting (FSI) problem is then analyzed considering three distinct and coupled regions, namely the elastic solid, inner boundary layer, and outer pipe region, as well as two time scales, namely a fast one associated with wave propagation along the tube and a slow one associated with momentum diffusion within the boundary layer. The couplings between the various pressures, velocity components, stress components, and elastic displacement fields is studied in detail to produce a complete asymptotic understanding, as depicted in Figure 2.

Within this framework, the leading–order four–(FSI) equations are recovered, exhibiting a pulsed velocity consistent with [22]'s average analysis predictions. Furthermore, at this leading–order, the resulting shear stress is found to be equally consistent with the leading–order long time behavior found by [36], except for a missing (FSI) coupling term, which is small in the limit of thick–wall, but can be significantly different for thin–wall and solid/fluid density ratio close to one. Seeking a prediction for the slow–time damping of the leading–order wave propagation, a secularity condition is developed from the analysis of first–

order perturbations. The resulting longitudinal, mode–dependent, exponential damping generalizes the $\nu_s \to 0$ theory of Mei & Jing [41, 42], now including (FSI). This damping not only depends on the fluid and solid properties through a newly defined tensor $\boldsymbol{\mathcal{E}}$ associated with dissipation but also on the considered boundary conditions though a damping vector $\boldsymbol{\mathcal{J}}_{\lambda_k}$. This is because it is directly related to $(\boldsymbol{\mathcal{E}}, \boldsymbol{\mathcal{J}}_{\lambda_k})$'s double contraction over vibration eigenmodes as well as to the corresponding eigenvalue, both directly connected with the set of axial boundary conditions. The resulting damping predictions are successfully compared with various experimental measurements, providing convincing evidence for the presented theory without any parameter fit. This contrast with many previous models, for which, depending on the considered experimental conditions (i.e steady Reynolds number, Mach number, aspect ratio, etc...) various unsteady friction models (e.g [52, 53, 37] among others) have been proposed in order to fit experimental damping. In these previously considered experimental conditions the Mach number and the Reynolds numbers might not necessarily match with the hereby asymptotic framework. This might perhaps explain the need for specific additional parameters in their models. Nevertheless, to our knowledge, apart from Mei & Jing [41] and the hereby presented analysis, no other damping model without parameter fitting can be found. In both cases, an explicit exponential damping law has been derived for a single pipe configuration and specific set of boundary conditions. Alternatively, the proposed unsteady friction model (associated with a $1/\sqrt{\pi t}$ diffusive kernel) could be used in a broader context, for example using the method of characteristics, but this exceeds the scope of the present contribution. Finally including FSI effect in the unsteady friction model could also be considered from using the *relative* acceleration of the fluid to that of the pipe's wall as suggested by [20] and provided in (121) for asymptotic consistency.

Appendix A. Steady–state fluid axial velocity leading–order solution

The steady–state contributions into the unsteady fluid equations (36)–(41) appear to be driven by the Mach number. Despite the asymptotic framework is $\delta \gg \mathcal{M}$, it is crucial to ensure that no steady–state contributions arise into the unsteady boundary layer (40). The leading–order dimensionless steady solution refers to as $\left(W_{st}^0, P_{st}^0\right)$. Steady–state mass conservation (33), follows steady incompressible condition

$$\partial_Z W_{st}^0 = 0. \tag{A.1}$$

On the other hand, $\epsilon^2\delta^2/\mathcal{M} = \epsilon/R_e \ll 1$ follows from the definition of δ, ϵ and $\mathcal{M}$ in (16)–(17) so that using (33), the steady–state leading–order pressure field is found uniform per section

$$\partial_R P_{st}^0 = 0. \tag{A.2}$$

Finally, the steady–state leading–order axial mass conservation equation (34) results in equalizing a R–dependent function to a Z–dependent one

$$\mathcal{M}\partial_Z P_{st}^0 = \delta^2 \frac{\partial_R}{R}\left(R\partial_R W_{st}^0\right), \tag{A.3}$$

yielding to

$$W_{st}^0 = \frac{\mathcal{M}}{4\delta^2}\partial_Z P_{st}^0\left[R^2-1\right] = \frac{\mathcal{M}}{4\delta}\partial_Z P_{st}^0\left[\delta y - 2\right] y, \tag{A.4}$$

$$\partial_y W_{st}^0 = \frac{\mathcal{M}}{4\delta}\partial_Z P_{st}^0\left[\delta y - 2\right] + \frac{\mathcal{M}}{4}\partial_Z P_{st}^0 y, \tag{A.5}$$

where the no–slip condition have been used at the fluid/solid interface. Hence the leading-order steady dimensionless velocity field in the boundary layer (A.4) is $O(\mathcal{M}/\delta)$ and thus not only smaller than one according to (18) but also smaller than both leading order $O(1)$ and $O(\delta)$ from asymptotic framework (18). Then, even if there is a (small) one–way coupling from steady flow to unsteady one in the boundary layer (40), they are not to be considered. Furthermore, since the steady-state shear stress in the boundary layer (A.5) is $O\left(\mathcal{M}\right)$ and since the deviatoric part of the steady–state stress tensor (26) is $O\left(\epsilon\delta/\mathcal{M}\right)$, the steady–state indeed contributes as $O\left(\epsilon\delta\right)$ correction to the boundary layer shear-stress,

smaller by $O(\epsilon)$ to the considered $O(\delta)$ corrections. The steady-state is thus irrelevant to the presented analysis. The dominance of unsteady boundary layer effects over steady ones, is thus based upon neglecting $O(\mathcal{M}/\delta)$ over $O(\delta)$ ones, the later being responsible for the wave damping.

Appendix B. Matching procedure for the radial velocity field

The leading–order inner axial velocity $\tilde{w}^0$ found in (117) can be y–integrated and Z–derived, such that

$$\partial_Z \int_0^y \tilde{w}^0 dy' = \alpha\sqrt{s}\left(1-e^{-\sqrt{s}y}\right)\partial_Z\tilde{\zeta}^0 - \frac{1}{s}\partial_Z^2\tilde{P}^0\left[y-\frac{1}{\sqrt{s}}\left(1-e^{-\sqrt{s}y}\right)\right] \quad \text{(B.1)}$$

The radial velocity matching procedure presented in (66) is detailed as follows. Invoking the expressions $\tilde{U}^{\,0}$, $\tilde{u}^0$, and $\tilde{u}^1$ in (107), (113) and (115), respectively, leads to the following

$$\begin{aligned}-\frac{1}{2}\tilde{\mathcal{F}}^0+\frac{1}{2}\delta^\gamma\eta\tilde{\mathcal{F}}^0+\delta\left(-\frac{1}{2}\tilde{\mathcal{F}}^1+\frac{1}{2}\delta^\gamma\eta\tilde{\mathcal{F}}^1\right) &= s\alpha\tilde{\xi}^0\big|_{R=1}+\frac{s}{\mathcal{C}^2}\tilde{P}^0\delta^\gamma\eta+s\alpha\delta^\gamma\tilde{\xi}^0\big|_{R=1}\\ &+\alpha\delta\left(s\tilde{\xi}^1\big|_{R=1}+\partial_T\tilde{\xi}^0\big|_{R=1}\right)+\alpha\sqrt{s}\partial_Z\tilde{\zeta}^0\big|_{\mathcal{R}_i}(\delta-E.S.T)\\ &-\frac{1}{s}\partial_Z^2\tilde{P}^0\left[\delta^\gamma\eta-\frac{1}{\sqrt{s}}(\delta-E.S.T)\right], \quad \text{(B.2)}\end{aligned}$$

or, reorganising terms

$$\begin{aligned}-\frac{1}{2}\tilde{\mathcal{F}}^0+\frac{1}{2}\delta^\gamma\eta\tilde{\mathcal{F}}^0-\frac{\delta}{2}\tilde{\mathcal{F}}^1 &= s\alpha\tilde{\xi}^0\big|_{R=1}+\frac{s}{\mathcal{C}^2}\tilde{P}^0\delta^\gamma\eta+s\alpha\delta^\gamma\eta\tilde{\xi}^0\big|_{R=1}\\ &+\alpha\delta\left(s\tilde{\xi}^1\big|_{R=1}+\partial_T\tilde{\xi}^0\big|_{R=1}\right)+\delta\alpha\sqrt{s}\partial_Z\tilde{\zeta}^0\big|_{R=1}\\ &-\frac{1}{s}\partial_Z^2\tilde{P}^0\left[\delta^\gamma\eta-\frac{\delta}{\sqrt{s}}\right]+O\left(\delta^{\gamma+1}\right). \quad \text{(B.3)}\end{aligned}$$

The asymptotic sequence reads as follows

- $O(1)$

$$\tilde{\mathcal{F}}^0 = -2s\alpha\tilde{\xi}^0\big|_{R=1}, \quad \text{(B.4)}$$

- $O(\delta^\gamma)$

$$\frac{1}{2}\tilde{\mathcal{F}}^0 = s\alpha\xi^0\big|_{R=1} + \frac{1}{s\mathcal{C}^2}\left(s^2 - \mathcal{C}^2\partial_Z^2\right)\tilde{P}^0. \tag{B.5}$$

Combining (C.1) and (C.2) considered at leading–order and in the Laplace domain yields

$$\left(s^2 - \mathcal{C}^2\partial_Z^2\right)\tilde{P}^0 = s\mathcal{C}^2\tilde{\mathcal{F}}^0, \tag{B.6}$$

such that

$$\tilde{\mathcal{F}}^0 = -2s\alpha\xi^0\big|_{R=1}, \tag{B.7}$$

which is identical to (B.4).

- $O(\delta)$

$$-\frac{1}{2}\tilde{\mathcal{F}}^1 = s\alpha\tilde{\xi}^1\big|_{R=1} + \alpha\partial_T\tilde{\xi}^0\big|_{R=1} + \frac{1}{\sqrt{s}}\left[\frac{1}{s}\partial_Z^2\tilde{P}^0 + \alpha s\partial_Z\tilde{\zeta}^0\big|_{R=1}\right]. \tag{B.8}$$

Using the definition of the parietal shear rate in (121) leads to the following

$$\tilde{\mathcal{F}}^1 = -2s\alpha\tilde{\xi}^1\big|_{R=1} - 2\alpha\partial_T\tilde{\xi}^0\big|_{R=1} + \frac{2}{s}\partial_Z\tilde{\tau}_w^0. \tag{B.9}$$

Through using (100), the matching functions $\mathcal{F}^0(Z,\tau,T)$ and $\mathcal{F}^1(Z,\tau,T)$ are fully determined from the inverse Laplace transform of (B.4) and (B.9)

$$\mathcal{F}^0(Z,\tau,T) = -\chi\partial_\tau P^0 + 2\alpha\nu_s\partial_Z\partial_\tau\zeta^0, \tag{B.10}$$

$$\mathcal{F}^1(Z,\tau,T) = -\chi\partial_\tau P^1 + 2\alpha\nu_s\partial_Z\partial_\tau\zeta^1 + \int_0^\tau\left(\partial_T\mathcal{F}^0 + 2\partial_Z\tau_w^0\right)d\tau^{'} \tag{B.11}$$

Appendix C. Derivation of FSI coupled hyperbolic system

The liquid–filled pipe dynamic, at both leading– and first–orders, coupled with (FSI) is governed by a set of two coupled hyperbolic problem systems. The first is related to an elastic solid wave propagation, whereas the second accounts for pulse pressure acoustic wave propagation. Each hyperbolic system is enslaved by either a pressure component for the solid elastic system or the solid axial stress for the fluid acoustic system. The fluid hyperbolic system is built upon a combination of the axial momentum and the mass conservation equations, or (105) and (108) respectively, with the expression of the asymptotic

matching functions $\mathcal{F}^0$ and $\mathcal{F}^1$ defined in (124) and (125). The axial momentum conservation equation then achieves in

$$\partial_\tau \left[W^0 + \delta W^1\right] + \delta \partial_T W^0 = -\partial_Z \left[P^0 + \delta P^1\right], \tag{C.1}$$

while the mass conservation equation leads to

$$\partial_\tau \left[P^0 + \delta P^1\right] + \partial_Z \left[W^0 + \delta W^1\right] = 2\alpha\nu_s \partial_Z \left(\partial_\tau \zeta^0 + \delta \left(\partial_\tau \zeta^1 + \partial_T \zeta^0\right)\right) - \delta \partial_T P^0 + 2\delta \int_0^\tau \partial_Z \tau_w^0 dt. \tag{C.2}$$

where the relation $(1 + \chi\mathcal{C}^2)/\mathcal{C}^2 = 1$ from (14) have been used. The solid hyperbolic system, in turn, depends on a combination of the axial momentum conservation equation and the derivation with respect to the fast time τ of the axial component of the Hooke's law through combining (94), (103)

$$\frac{\alpha}{\mathcal{D}} \left(\partial_\tau^2 \zeta^0 + \delta \left(\partial_\tau^2 \zeta^1 + 2\partial_T \partial_\tau \zeta^0\right)\right) - \partial_Z \left[\sigma_{zz}^0 + \delta \sigma_{zz}^1\right] = \frac{2\delta\tau_w^0}{\alpha(2+\alpha)}, \tag{C.3}$$

$$\partial_\tau \left(\sigma_{zz}^0 + \delta \sigma_{zz}^1\right) - \frac{\alpha \mathcal{C}_s^2}{\mathcal{D}} \partial_Z \partial_\tau \left[\zeta^0 + \delta \zeta^1\right] = \frac{2\nu_s}{\alpha(2+\alpha)} \left(P^0 + \delta P^1\right). \tag{C.4}$$

The fast time integration of (C.4)'s leading–order gives

$$-\frac{\alpha \mathcal{C}_s^2}{\mathcal{D}} \partial_Z \zeta^0 = \frac{2\nu_s}{\alpha(2+\alpha)} P^0 - \sigma_{zz}^0, \tag{C.5}$$

then yielding to

$$\partial_\tau \left[\sigma_{zz}^0 + \delta \sigma_{zz}^1\right] - \frac{\alpha \mathcal{C}_s^2}{\mathcal{D}} \partial_Z \left[\partial_\tau \zeta^0 + \delta \left(\partial_\tau \zeta^1 + 2\partial_T \zeta^0\right)\right] = \frac{2\nu_s}{\alpha(2+\alpha)} \partial_\tau \left[P^0 + \delta P^1\right] + 2\delta \partial_T \left(\frac{2\nu_s}{\alpha(2+\alpha)} P^0 - \sigma_{zz}^0\right). \tag{C.6}$$

The equations set of (C.1), (C.2), (C.3) and (C.6) provides the four–(FSI) coupled hyperbolic equations associated with the dynamic of the liquid–filled pipe problem. At leading–order, it is identical to those derived by ([58]) and ([22]). The ([22])'s derivation was based on averaging solid displacement vectors and stress along the radial direction. This approach relies on the hypothesis of no tangential shear stress in the solid (Eq. (48) demonstrates that it is indeed $O(\epsilon)$ smaller than the stress spherical components), providing radially uniform stress, which is also a basic assumption of thin–shell models ([16]). The constitutive

hyperbolic coupled system is hereby re–organized into a coupled wave equation system that acts upon the pressure and stress variables only. Let us first focus on the pressure wave equation derivation. Combining a fast–time derivative of the outer mass equation (C.2) with the spatial derivative of the outer momentum equation (C.1) leads to the following

$$\left(\partial_\tau^2 - \partial_Z^2\right)\left[P^0 + \delta P^1\right] = 2\alpha\nu_s\partial_Z\partial_\tau\left(\partial_\tau\zeta^0 + \delta\left(\partial_\tau\zeta^1 + \partial_T\zeta^0\right)\right) + \delta\partial_T\left(\partial_Z W^0 - \partial_\tau P^0\right) + 2\delta\partial_Z\tau_w^0. \quad \text{(C.7)}$$

The leading–order of (C.2) reads as follows

$$\partial_\tau P^0 + \partial_Z W^0 = 2\alpha\nu_s\partial_Z\partial_\tau\zeta^0, \quad \text{(C.8)}$$

while combining (C.8) with (C.3) results in

$$\left(\partial_\tau^2 - \partial_Z^2\right)\left[P^0 + \delta P^1\right] = 2\alpha\nu_s\partial_Z\partial_\tau\left(\partial_\tau\zeta^0 + \delta\left(\partial_\tau\zeta^1 + 2\partial_T\zeta^0\right)\right) - 2\delta\left(\partial_T\partial_\tau P^0 - \partial_Z\tau_w^0\right). \quad \text{(C.9)}$$

We now use (C.6) to substitute for $\partial_Z\left(\partial_\tau\zeta^0 + \delta\left(\partial_\tau\zeta^1 + 2\partial_T\zeta^0\right)\right)$ in (C.9). This yields

$$\left(\left[1 + \frac{4\nu_s^2\mathcal{D}}{\alpha(2+\alpha)\mathcal{C}_s^2}\right]\partial_\tau^2 - \partial_Z^2\right)\left[P^0 + \delta P^1\right] = \frac{2\nu_s\mathcal{D}}{\mathcal{C}_s^2}\partial_\tau^2\left[\sigma_{zz}^0 + \delta\sigma_{zz}^1\right] - 2\delta\left[\partial_T\partial_\tau\left(\left[1 + \frac{4\nu_s^2\mathcal{D}}{\alpha(2+\alpha)\mathcal{C}_s^2}\right]P^0 - \frac{2\nu_s\mathcal{D}}{\mathcal{C}_s^2}\sigma_{zz}^0\right) - \partial_Z\tau_w^0\right]. \quad \text{(C.10)}$$

On the other hand, the solid stress wave equation is revealed by a simple combination of the derivative with respect to τ in (C.6) with the derivative with respect to Z in (C.3), yielding the following

$$\left(\partial_\tau^2 - \mathcal{C}_s^2\partial_Z^2\right)\left[\sigma_{zz}^0 + \delta\sigma_{zz}^1\right] = \frac{2\nu_s}{\alpha(2+\alpha)}\partial_\tau^2\left[P^0 + \delta P^1\right] - 2\delta\left[\partial_T\partial_\tau\left(\sigma_{zz}^0 - \frac{2\nu_s}{\alpha(2+\alpha)}P^0\right) - \frac{\mathcal{C}_s^2}{\alpha(2+\alpha)}\partial_Z\tau_w^0\right]. \quad \text{(C.11)}$$

Both wave–equations can be re–casted into a coupled formulation

$$\left(\partial_\tau^2 - \mathbf{C}_\mathbf{P}^2\partial_Z^2\right)\left[\mathbf{P}^0 + \delta\mathbf{P}^1\right] = -2\delta\left[\partial_T\partial_\tau\mathbf{P}^0 - \partial_Z\tau_w^0\begin{pmatrix} 1 + \frac{2\nu_s\mathcal{D}}{\alpha(2+\alpha)} \\ \frac{1}{\alpha(2+\alpha)}\left[2\nu_s\mathcal{D} + \mathcal{C}_s^2 + \frac{4\nu_s^2\mathcal{D}}{\alpha(2+\alpha)}\right]\end{pmatrix}\right], \quad \text{(C.12)}$$

where

$$\mathbf{C}^2_{\mathbf{P}} = \begin{pmatrix} 1 & 2\nu_s\mathcal{D} \\ \frac{2\nu_s}{\alpha(2+\alpha)} & \frac{4\nu_s^2\mathcal{D}}{\alpha(2+\alpha)} + \mathcal{C}_s^2 \end{pmatrix} \quad \text{, and, } \quad \mathbf{P}^0 + \delta\mathbf{P}^1 = \begin{pmatrix} P^0 + \delta P^1 \\ \sigma^0_{zz} + \delta\sigma^1_{zz} \end{pmatrix}. \quad \text{(C.13)}$$

516

517 Appendix D. Comparative analysis with Tijsseling's theory

518 One starts from the four–(FSI) coupled equation system derived by ([22])

$$\begin{aligned}
\partial_t W^* + \frac{1}{\rho_{f_0}}\partial_z P^* &= 0, && \text{(D.1)}\\
\partial_z W^* + \left[\frac{1}{\mathcal{K}_f} + \frac{2}{E}\left(\frac{1}{\alpha} + \frac{1+\alpha}{2+\alpha} + \nu_s\right)\right]\partial_t P^* &= \frac{2\nu_s}{E}\partial_t\sigma^*_{zz}, && \text{(D.2)}\\
\partial_t\dot{\zeta}^* - \frac{1}{\rho_{s_0}}\partial_z\sigma^*_{zz} &= 0, && \text{(D.3)}\\
\partial_z\dot{\zeta}^* - \frac{1}{E}\partial_t\sigma^*_{zz} &= -\frac{2\nu_s}{\alpha E\,(2+\alpha)}\partial_t P^*, && \text{(D.4)}
\end{aligned}$$

519 Invoking the scaling from §2.3.2 and §2.4, leads to

$$\begin{aligned}
\partial_\tau W + \partial_Z P &= 0, && \text{(D.5)}\\
\partial_Z W + \rho_{f_0}c_p^2\left[\frac{1}{\mathcal{K}_f} + \frac{2}{E}\left(\frac{1}{\alpha} + \frac{1+\alpha}{2+\alpha} + \nu_s\right)\right]\partial_\tau P &= \frac{2\nu_s\rho_{f_0}c_p^2}{E}\partial_\tau\sigma_{zz}, && \text{(D.6)}\\
\partial_\tau\dot{\zeta} - \frac{\mathcal{D}}{\alpha}\partial_Z\sigma_{zz}, &= 0, && \text{(D.7)}\\
\frac{\alpha E}{\rho_{f_0}c_p^2}\partial_Z\dot{\zeta} - \partial_\tau\sigma_{zz} &= -\frac{2\nu_s}{\alpha\,(2+\alpha)}\partial_\tau P, && \text{(D.8)}
\end{aligned}$$

Using (9), (10), and (15), one finds

$$\frac{E}{\rho_{f_0}c_p^2} = \frac{\mathcal{C}_s^2}{\mathcal{D}}, \qquad \text{(D.9)}$$

520 and

$$\begin{aligned}
\partial_\tau W + \partial_Z P &= 0, && \text{(D.10)}\\
\partial_Z W + \rho_{f_0}c_p^2\left[\frac{1}{\mathcal{K}_f} + \frac{2}{E}\left(\frac{1}{\alpha} + \frac{1+\alpha}{2+\alpha} + \nu_s\right)\right]\partial_\tau P &= \frac{2\nu_s\mathcal{D}}{\mathcal{C}_s^2}\partial_\tau\sigma_{zz}, && \text{(D.11)}\\
\partial_\tau\dot{\zeta} - \frac{\mathcal{D}}{\alpha}\partial_Z\sigma_{zz} &= 0, && \text{(D.12)}\\
\frac{\alpha\mathcal{C}_s^2}{\mathcal{D}}\partial_Z\dot{\zeta} - \partial_\tau\sigma_{zz} &= -\frac{2\nu_s}{\alpha\,(2+\alpha)}\partial_\tau P, && \text{(D.13)}
\end{aligned}$$

One is left with an expression of the term $\rho_{f_0} c_p^2 \left[\frac{1}{\mathcal{K}_f} + \frac{2}{E}\left(\frac{1}{\alpha} + \frac{1+\alpha}{2+\alpha} + \nu_s\right)\right]$ versus dimensionless parameters. Using the definition of acoustic fluid wave speed $c_0 = \sqrt{\mathcal{K}_f/\rho_{f_0}}$ while invoking (9), (10), and (15) leads to

$$\rho_{f_0} c_p^2 \left[\frac{1}{\mathcal{K}_f} + \frac{2}{E}\left(\frac{1}{\alpha} + \frac{1+\alpha}{2+\alpha} + \nu_s\right)\right] = 1 + \frac{4\nu_s^2 \mathcal{D}}{\alpha(2+\alpha)\mathcal{C}_s^2}. \tag{D.14}$$

521 Now, combining (D.11) within (D.13) result in

$$\begin{aligned}
\partial_\tau \sigma_{zz} - \frac{\alpha \mathcal{C}_s^2}{\mathcal{D}} \partial_Z \dot{\zeta} &= \frac{2\nu_s}{\alpha(2+\alpha)} \partial_\tau P, && \text{(D.15)}\\
\partial_\tau \dot{\zeta} &= \frac{\mathcal{D}}{\alpha} \partial_Z \sigma_{zz}, && \text{(D.16)}\\
\partial_\tau P + \partial_Z W &= 2\alpha\nu_s \partial_Z \dot{\zeta}, && \text{(D.17)}\\
\partial_\tau W &= -\partial_Z P. && \text{(D.18)}
\end{aligned}$$

522 The four–(FSI) dimensionless equation system derived by ([22]) is thus identical
523 to the one asymptotically defined in §3.8.

524 Appendix E. Vector–wave system in the Laplace domain

The first–order dynamic is governed by the equations (C.10) and (C.11) expressed within the Laplace domain

$$\begin{aligned}
\left(\left[1 + \frac{4\nu_s^2 \mathcal{D}}{\alpha(2+\alpha)\mathcal{C}_s^2}\right] s^2 - \partial_Z^2\right)\left[\tilde{P}^0 + \delta \tilde{P}^1\right] &= \frac{2\nu_s \mathcal{D}}{\mathcal{C}_s^2} s^2 \left[\tilde{\sigma}_{zz}^0 + \delta \tilde{\sigma}_{zz}^1\right]\\
&\quad - 2\delta \left[s\partial_T \left(\left[1 + \frac{4\nu_s^2 \mathcal{D}}{\alpha(2+\alpha)\mathcal{C}_s^2}\right] \tilde{P}^0 - \frac{2\nu_s \mathcal{D}}{\mathcal{C}_s^2} \tilde{\sigma}_{zz}^0\right) - \partial_Z \tilde{\tau}_w^0\right], \quad \text{(E.1)}
\end{aligned}$$

and

$$\begin{aligned}
\left(s^2 - \mathcal{C}_s^2 \partial_Z^2\right)\left[\tilde{\sigma}_{zz}^0 + \delta \tilde{\sigma}_{zz}^1\right] &= \frac{2\nu_s}{\alpha(2+\alpha)} s^2 \left[\tilde{P}^0 + \delta \tilde{P}^1\right]\\
&\quad - 2\delta \left[s\partial_T \left(\tilde{\sigma}_{zz}^0 - \frac{2\nu_s}{\alpha(2+\alpha)} \tilde{P}^0\right) - \frac{\mathcal{C}_s^2}{\alpha(2+\alpha)} \partial_Z \tilde{\tau}_w^0\right]. \quad \text{(E.2)}
\end{aligned}$$

By combining the previous relations with the derived expression of $\partial_Z \tilde{\tau}_w(Z, s)$ in (131), it follows

$$\left(\mathbf{A}s^2 - \mathbf{B}\partial_Z^2\right)\left(\tilde{\mathbf{P}}^0 + \delta \tilde{\mathbf{P}}^1\right) = -2s\delta \left(\mathbf{A}s^2 + \sqrt{s}\mathbf{D}\right)\tilde{\mathbf{P}}^0, \tag{E.3}$$

with $\mathbf{A}$, $\mathbf{B}$, $\mathbf{D}$ and $\left(\tilde{\mathbf{P}}^0, \tilde{\mathbf{P}}^1\right)$ defined as

$$\mathbf{A} = \begin{pmatrix} 1 + \frac{4\nu_s^2 \mathcal{D}}{\alpha \mathcal{C}_s^2 (2+\alpha)} & -\frac{2\nu_s \mathcal{D}}{\mathcal{C}_s^2} \\ \\ -\frac{2\nu_s}{\alpha(2+\alpha)} & 1 \end{pmatrix} \ , \ \mathbf{B} = \begin{pmatrix} 1 & 0 \\ 0 & \mathcal{C}_s^2 \end{pmatrix} \ , \ \tilde{\mathbf{P}}^0 = \begin{pmatrix} \tilde{P}^0 \\ \tilde{\sigma}_{zz}^0 \end{pmatrix} \ , \ \tilde{\mathbf{P}}^1 = \begin{pmatrix} \tilde{P}^1 \\ \tilde{\sigma}_{zz}^1 \end{pmatrix}, \tag{E.4}$$

$$\mathbf{D} = \begin{pmatrix} 1 - (1 - 2\nu_s) \frac{2\nu_s \mathcal{D}}{\alpha \mathcal{C}_s^2 (2+\alpha)} & \frac{(1-2\nu_s)\mathcal{D}}{\mathcal{C}_s^2} \\ \\ \frac{\mathcal{C}_s^2}{\alpha(2+\alpha)} \left(1 - (1 - 2\nu_s) \frac{2\nu_s \mathcal{D}}{\alpha \mathcal{C}_s^2 (2+\alpha)}\right) & \frac{(1-2\nu_s)\mathcal{D}}{\alpha(2+\alpha)} \end{pmatrix}. \tag{E.5}$$

Since $\mathbf{A}$ is a unitary matrix, its inverse reads as follows

$$\mathbf{A}^{-1} = \begin{pmatrix} 1 & \frac{2\nu_s \mathcal{D}}{\mathcal{C}_s^2} \\ \\ \frac{2\nu_s}{\alpha(2+\alpha)} & 1 + \frac{4\nu_s^2 \mathcal{D}}{\alpha \mathcal{C}_s^2 (2+\alpha)} \end{pmatrix}. \tag{E.6}$$

Let us define the matrix $\mathbf{E} = \mathbf{A}^{-1} \cdot \mathbf{D}$. Noting that $\mathbf{C}_{\mathbf{P}}^2 = \mathbf{A}^{-1} \cdot \mathbf{B}$, and using the definition of $\overline{c^2}$ in (129), one yields

$$\mathbf{E} = \frac{1}{2\nu_s} \begin{pmatrix} \left(1 - (1 - 2\nu_s) \frac{\overline{c^2} - 1}{\mathcal{C}_s^2}\right) \left(1 + \frac{2\nu_s \mathcal{D}}{\alpha(2+\alpha)}\right) & \frac{2\nu_s \mathcal{D}(1-2\nu_s)}{\mathcal{C}_s^2} \left(1 + \frac{2\nu_s \mathcal{D}}{\alpha(2+\alpha)}\right) \\ \\ \left(1 - (1 - 2\nu_s) \frac{\overline{c^2} - 1}{\mathcal{C}_s^2}\right) \frac{\overline{c^2} - (1-2\nu_s)}{\alpha(2+\alpha)} & \frac{2\nu_s \mathcal{D}(1-2\nu_s)}{\mathcal{C}_s^2} \frac{\overline{c^2} - (1-2\nu_s)}{\alpha(2+\alpha)} \end{pmatrix}, \tag{E.7}$$

such that

$$\left(s^2 - \mathbf{C}_{\mathbf{P}}^2 \partial_Z^2\right) \left[\tilde{\mathbf{P}}^0 + \delta \tilde{\mathbf{P}}^1\right] = -2s\delta \left(\partial_T + \sqrt{s}\mathbf{E}\right) \tilde{\mathbf{P}}^0. \tag{E.8}$$

Appendix F. Self–adjointness of the $\mathcal{H}$ operator and eigenvector decomposition

([33]) developed a solution for the leading–order vector–wave equation (146) associated with boundary conditions (141)–(143) using the orthonormal decomposition basis arising from the eigenvectors $\mathbf{\Phi}_{\lambda_k}(Z)$ of the operator $\mathcal{H}$, whereby $\tilde{\boldsymbol{\mathcal{P}}}^0$ and $\tilde{\boldsymbol{\mathcal{P}}}^1$ were projected. To achieve this decomposition, one must set $\mathcal{H}$'s self–adjointness. Defining the scalar product

$$\forall \mathbf{\Psi}, \mathbf{\Psi}^{'} \in L^2(\mathbb{R}) \times L^2(\mathbb{R}), \quad \forall \eta_1, \eta_2 \in \mathbb{R}, \quad \langle \mathbf{\Psi}^{'}, \mathbf{\Psi} \rangle = \sum_{j=1}^{2} \eta_j \int_0^1 \Psi_j^{'}(Z) \Psi_j(Z) dZ, \tag{F.1}$$

with $\boldsymbol{\eta} \equiv (\eta_1, \eta_2) \in \mathbb{R}^2$ an as yet unknown real vector that is adapted to each specific boundary condition set. From the self–adjoint property $\langle \mathcal{H}\boldsymbol{\Psi}, \boldsymbol{\Psi}^{'} \rangle = \langle \boldsymbol{\Psi}, \mathcal{H}\boldsymbol{\Psi}^{'} \rangle$, one finds from (F.1) condition

$$\sum_{j=1}^{2} \eta_j c_j^2 \left[\partial_Z \Psi_j(Z) \Psi_j^{'}(Z) - \Psi_j(Z) \partial_Z \Psi_j^{'}(Z) \right]_0^1 = 0. \tag{F.2}$$

Denoting $-\lambda_k^2$, the k^{th} eigenvalue is real negative in accordance with the well–known Laplacian eigenvalues. Its related eigenfunction $\boldsymbol{\Phi}_{\lambda_k}$, fulfills the following eigenvalue problem

$$\mathcal{H}\boldsymbol{\Phi}_{\lambda_k}(Z) = -\lambda_k^2 \boldsymbol{\Phi}_{\lambda_k}(Z), \tag{F.3}$$

or, using (144)

$$\partial_Z^2 \boldsymbol{\Phi}_{\lambda_k}(Z) = -\lambda_k^2 \boldsymbol{\mathcal{C}}_{\boldsymbol{\mathcal{P}}}^{-2} \boldsymbol{\Phi}_{\lambda_k}(Z), \quad \text{with} \quad \boldsymbol{\mathcal{C}}_{\boldsymbol{\mathcal{P}}}^{-2} = \begin{pmatrix} c_-^{-2} & 0 \\ 0 & c_+^{-2} \end{pmatrix}. \tag{F.4}$$

The solution to (F.4) reads as follows

$$\begin{pmatrix} \boldsymbol{\Phi}_{\lambda_k}(Z) \\ \partial_Z \boldsymbol{\Phi}_{\lambda_k}(Z) \end{pmatrix} = \begin{pmatrix} \partial_Z \mathbf{T}_{\lambda_k}(Z) & \mathbf{T}_{\lambda_k}(Z) \\ -\lambda_k^2 \boldsymbol{\mathcal{C}}_{\boldsymbol{\mathcal{P}}}^{-2} \mathbf{T}_{\lambda_k}(Z) & \partial_Z \mathbf{T}_{\lambda_k}(Z) \end{pmatrix} \begin{pmatrix} \boldsymbol{\Phi}_{\lambda_k}(0) \\ \partial_Z \boldsymbol{\Phi}_{\lambda_k}(0) \end{pmatrix}, \tag{F.5}$$

where

$$\mathbf{T}_{\lambda_k}(Z) = \frac{1}{\lambda_k} \begin{pmatrix} c_- \sin\left(\frac{\lambda_k Z}{c_-}\right) & 0 \\ 0 & c_+ \sin\left(\frac{\lambda_k Z}{c_+}\right) \end{pmatrix}, \tag{F.6}$$

and $(\boldsymbol{\Phi}_{\lambda_k}(0), \partial_Z \boldsymbol{\Phi}_{\lambda_k}(0))^T$ represent the modal-dependent amplitudes of $\boldsymbol{\Phi}_{\lambda_k}(Z)$, each of which is associated with the Dirichlet or Neumann condition imposed at $Z = 0\&1$. Furthermore $\boldsymbol{\Phi}_{\lambda_k}(Z)$ should ensures the homogeneous boundary condition system (145). Finding a non trivial solution leads to the following condition

$$\begin{vmatrix} \boldsymbol{\mathcal{N}} & \boldsymbol{\mathcal{M}} \\ \boldsymbol{\mathcal{Q}} \partial_Z \mathbf{T}_k(1) - \lambda_k^2 \boldsymbol{\mathcal{R}} \boldsymbol{\mathcal{C}}_{\boldsymbol{\mathcal{P}}}^{-2} \mathbf{T}_k(1) & \boldsymbol{\mathcal{Q}} \mathbf{T}_k(1) + \boldsymbol{\mathcal{R}} \partial_Z \mathbf{T}_k(1) \end{vmatrix} = 0. \tag{F.7}$$

This transcendental equation upon λ_k fully prescribes the system's spectrum $\mathcal{S}_{\mathcal{P}}$. While the radial boundary condition (i.e., the stress and velocity continuity conditions) informs about the wave-speed propagations of pulses within both

fluid and solid, the axial boundary conditions located at the pipe's dead-end, in-turn, specify the system's spectrum

$$\mathcal{S}_{\mathcal{P}} = \{-\lambda_k^2 \ \mid \ \lambda_k \in \mathbb{R}^+\}. \tag{F.8}$$

Combining the boundary matrix expressions provided in (142) with the spectrum equation (F.7) yields the following (simplified) transcendental equation,

$$\beta \tan\left(\frac{\lambda_k}{c_-}\right) = \tan\left(\frac{\lambda_k}{c_+}\right), \tag{F.9}$$

where β was provided in (143). ([33]) found the following analytical expression for the eigenvectors $\mathbf{\Phi}_{\lambda_k}(Z)$

$$\begin{aligned}
\mathbf{\Phi}_{\lambda_k}(Z) &= \frac{\tilde{\mathbf{\Phi}}_{\lambda_k}(Z)}{\|\tilde{\mathbf{\Phi}}_{\lambda_k}(Z)\|}, & \text{(F.10)}\\
\tilde{\mathbf{\Phi}}_{\lambda_k}(Z) &= \begin{pmatrix} \cos\left(\frac{\lambda_k}{c_-}Z\right) + \tan\left(\frac{\lambda_k}{c_-}\right)\sin\left(\frac{\lambda_k}{c_-}Z\right) \\ -\frac{c_+}{\beta c_-}\left[\cos\left(\frac{\lambda_k}{c_+}Z\right) + \tan\left(\frac{\lambda_k}{c_+}\right)\sin\left(\frac{\lambda_k}{c_+}Z\right)\right] \end{pmatrix}, & \text{(F.11)}\\
\|\tilde{\mathbf{\Phi}}_{\lambda_k}(Z)\|^2 &= \frac{c_+\beta\cos^2\left(\frac{\lambda_k}{c_+}\right) - c_-\cos^2\left(\frac{\lambda_k}{c_-}\right)}{2c_+\beta\cos^2\left(\frac{\lambda_k}{c_+}\right)\cos^2\left(\frac{\lambda_k}{c_-}\right)}, & \text{(F.12)}\\
\boldsymbol{\eta} &= \begin{pmatrix}\eta_1\\ \eta_2\end{pmatrix} = \begin{pmatrix} 1 \\ -\beta\left(\frac{c_-}{c_+}\right)^3 \end{pmatrix}. & \text{(F.13)}
\end{aligned}$$

Appendix G. Simplification of $\left(s^2 - \mathcal{H}\right)\tilde{\boldsymbol{\mathcal{P}}}_p^1(s, Z)$

Let us combine the definition of the operator $\mathcal{H}$ in (144) with the expression of $\tilde{\boldsymbol{\mathcal{P}}}_p^1(s, Z)$ in (148), it follows

$$\begin{aligned}
\left(s^2 - \mathcal{H}\right)\tilde{\boldsymbol{\mathcal{P}}}_p^1(s, Z) = &\frac{s^2Z^2 - 2\boldsymbol{\mathcal{C}}_{\boldsymbol{\mathcal{P}}}^2}{\alpha(2+\alpha)\sqrt{s}\left(1 - \frac{c_+}{c_-\beta}\right)}\begin{pmatrix} 1 \\ -\frac{c_+}{c_-\beta}\end{pmatrix}\\
&- \frac{4\nu_s\mathcal{D}\left(s^2\left(\frac{Z^2}{2} - Z\right) - \boldsymbol{\mathcal{C}}_{\boldsymbol{\mathcal{P}}}^2\right)}{\alpha(2+\alpha)\sqrt{s}\left(c_-^2 - 1\right)}\begin{pmatrix} 1 & 0 \\ 0 & \frac{c_-\beta}{c_+}\end{pmatrix}\partial_Z\tilde{\boldsymbol{\mathcal{P}}}^0\big|_{Z=0}.
\end{aligned} \tag{G.1}$$

The expression of $\partial_Z \tilde{\boldsymbol{\mathcal{P}}}^0\big|_{Z=0}$, which is easily deduced from (147) and (151), then yields to

$$\left(s^2-\mathcal{H}\right)\tilde{\boldsymbol{\mathcal{P}}}_p^1(s,Z)=\frac{s^2Z^2-2\boldsymbol{\mathcal{C}}_{\boldsymbol{\mathcal{P}}}^2}{\alpha(2+\alpha)\sqrt{s}\left(1-\frac{c_+}{c_-\beta}\right)}\begin{pmatrix}1\\-\frac{c_+}{c_-\beta}\end{pmatrix}$$
$$-\frac{4\nu_s\mathcal{D}}{\alpha(2+\alpha)\sqrt{s}\left(c_-^2-1\right)}\sum_{\lambda_k\in\mathbb{R}}\tilde{a}^0_{\lambda_k}(s)A_{\lambda_k}(T)\left(s^2\left(\frac{Z^2}{2}-Z\right)-\boldsymbol{\mathcal{C}}_{\boldsymbol{\mathcal{P}}}^2\right)\begin{pmatrix}1&0\\0&\frac{c_-\beta}{c_+}\end{pmatrix}\partial_Z\boldsymbol{\Phi}_{\lambda_k}\big|_{Z=0}$$
$$-\frac{4\nu_s\mathcal{D}\left(s^2\left(\frac{Z^2}{2}-Z\right)-\boldsymbol{\mathcal{C}}_{\boldsymbol{\mathcal{P}}}^2\right)}{\alpha(2+\alpha)\sqrt{s}\det\left(\boldsymbol{\Pi}\right)\left(c_-^2-1\right)}\begin{pmatrix}1\\-\frac{c_-\beta}{c_+}\end{pmatrix},\quad\text{(G.2)}$$

or otherwise since $\det\left(\boldsymbol{\Pi}\right)=\frac{2\nu_s\mathcal{D}}{c_-^2-1}\left(1-\frac{c_-\beta}{c_+}\right)$

$$\left(s^2-\mathcal{H}\right)\tilde{\boldsymbol{\mathcal{P}}}_p^1(s,Z)=\frac{1}{\alpha(2+\alpha)\sqrt{s}}\left(\frac{s^2Z^2-2\boldsymbol{\mathcal{C}}_{\boldsymbol{\mathcal{P}}}^2}{1-\frac{c_+}{c_-\beta}}\begin{pmatrix}1\\-\frac{c_+}{c_-\beta}\end{pmatrix}-2\frac{s^2\left(\frac{Z^2}{2}-Z\right)-\boldsymbol{\mathcal{C}}_{\boldsymbol{\mathcal{P}}}^2}{1-\frac{c_-\beta}{c_+}}\begin{pmatrix}1\\-\frac{c_-\beta}{c_+}\end{pmatrix}\right)$$
$$-\frac{2}{\alpha(2+\alpha)\sqrt{s}\left(1-\frac{c_-\beta}{c_+}\right)}\sum_{\lambda_k\in\mathbb{R}}\tilde{a}^0_{\lambda_k}(s)A_{\lambda_k}(T)\left(s^2\left(\frac{Z^2}{2}-Z\right)-\boldsymbol{\mathcal{C}}_{\boldsymbol{\mathcal{P}}}^2\right)\begin{pmatrix}1&0\\0&\frac{c_-\beta}{c_+}\end{pmatrix}\partial_Z\boldsymbol{\Phi}_{\lambda_k}\big|_{Z=0}.\quad\text{(G.3)}$$

Regarding the definition of $\partial_Z\boldsymbol{\Phi}_{\lambda_k}\big|_{Z=0}$ provided in (F.11), it follows

$$\left(s^2\left(\frac{Z^2}{2}-Z\right)-\boldsymbol{\mathcal{C}}_{\boldsymbol{\mathcal{P}}}^2\right)\begin{pmatrix}1&0\\0&\frac{c_-\beta}{c_+}\end{pmatrix}\partial_Z\boldsymbol{\Phi}_{\lambda_k}\big|_{Z=0}=\frac{\lambda_k}{c_-}\begin{pmatrix}\left(s^2\left(\frac{Z^2}{2}-Z\right)-c_-^2\right)\tan\left(\frac{\lambda_k}{c_-}\right)\\-\frac{c_-}{c_+}\left(s^2\left(\frac{Z^2}{2}-Z\right)-c_+^2\right)\tan\left(\frac{\lambda_k}{c_+}\right)\end{pmatrix}.\quad\text{(G.4)}$$

whilst injecting the expression of $\tilde{a}^0_{\lambda_k}(s)$ derived in (156) into (G.3), it results

$$\left(s^2-\mathcal{H}\right)\tilde{\boldsymbol{\mathcal{P}}}_p^1(s,Z)=\frac{1}{\alpha(2+\alpha)\sqrt{s}}\left(\frac{s^2Z^2-2\boldsymbol{\mathcal{C}}_{\boldsymbol{\mathcal{P}}}^2}{1-\frac{c_+}{c_-\beta}}\begin{pmatrix}1\\-\frac{c_+}{c_-\beta}\end{pmatrix}-\frac{s^2\left(Z^2-2Z\right)-2\boldsymbol{\mathcal{C}}_{\boldsymbol{\mathcal{P}}}^2}{1-\frac{c_-\beta}{c_+}}\begin{pmatrix}1\\-\frac{c_-\beta}{c_+}\end{pmatrix}\right)$$
$$+\sum_{\lambda_k\in\mathbb{R}}\left[\frac{i\lambda_k}{s-i\lambda_k}+1\right]\frac{\langle\tilde{\boldsymbol{\mathcal{P}}}_p^0(Z),\boldsymbol{\Phi}_{\lambda_k}(Z)\rangle}{\sqrt{s}}A_{\lambda_k}(T)\boldsymbol{\mathcal{J}}_{\lambda_k}(Z,s),\quad\text{(G.5)}$$

with

$$\boldsymbol{\mathcal{J}}_{\lambda_k}(Z,s)=\frac{\lambda_k}{\alpha(2+\alpha)\left(1-\frac{c_-\beta}{c_+}\right)}\begin{pmatrix}\left(s^2\left(\frac{Z^2}{2}-Z\right)-c_-^2\right)\frac{\tan\left(\frac{\lambda_k}{c_-}\right)}{c_-}\\-\left(s^2\left(\frac{Z^2}{2}-Z\right)-c_+^2\right)\frac{\tan\left(\frac{\lambda_k}{c_+}\right)}{c_+}\end{pmatrix}.\quad\text{(G.6)}$$

531

Appendix H. Further investigation of $\mathcal{T}_{\boldsymbol{\lambda}_k}^{-1}$

Let us define $\mathcal{E}_{i,j}$, $i,j \in \{1,2\}$ as the matrix elements of $\boldsymbol{\mathcal{E}} = \boldsymbol{\Pi}^{-1} \cdot \mathbf{E} \cdot \boldsymbol{\Pi}$. Invoking the definition of $\boldsymbol{\Pi}$ and $\boldsymbol{\Pi}^{-1}$ in (135) along with that of $\mathbf{E}$ in (E.7) leads to the following

$$\mathcal{E}_{11} = \frac{\mathcal{D}\left[\frac{1-(1-2\nu_s)\frac{\overline{c^2}-1}{c_s^2}}{c_-^2-1} + \frac{1-2\nu_s}{\mathcal{C}_s^2}\right]\left[1+\frac{2\nu_s\mathcal{D}}{\alpha(2+\alpha)}\left(1-\frac{\overline{c^2}-(1-2\nu_s)}{c_+^2-1}\right)\right]}{\det\boldsymbol{\Pi}}, \quad (H.1)$$

$$\mathcal{E}_{12} = \frac{\mathcal{D}\left[\frac{1-(1-2\nu_s)\frac{\overline{c^2}-1}{c_s^2}}{c_+^2-1} + \frac{1-2\nu_s}{\mathcal{C}_s^2}\right]\left[1+\frac{2\nu_s\mathcal{D}}{\alpha(2+\alpha)}\left(1-\frac{\overline{c^2}-(1-2\nu_s)}{c_+^2-1}\right)\right]}{\det\boldsymbol{\Pi}}, \quad (H.2)$$

$$\mathcal{E}_{21} = \frac{\mathcal{D}\left[\frac{1-(1-2\nu_s)\frac{\overline{c^2}-1}{c_s^2}}{c_-^2-1} + \frac{1-2\nu_s}{\mathcal{C}_s^2}\right]\left[\frac{2\nu_s\mathcal{D}}{\alpha(2+\alpha)}\left(\frac{\overline{c^2}-(1-2\nu_s)}{c_-^2-1}-1\right)-1\right]}{\det\boldsymbol{\Pi}}, \quad (H.3)$$

$$\mathcal{E}_{22} = \frac{\mathcal{D}\left[\frac{1-(1-2\nu_s)\frac{\overline{c^2}-1}{c_s^2}}{c_+^2-1} + \frac{1-2\nu_s}{\mathcal{C}_s^2}\right]\left[\frac{2\nu_s\mathcal{D}}{\alpha(2+\alpha)}\left(\frac{\overline{c^2}-(1-2\nu_s)}{c_-^2-1}-1\right)-1\right]}{\det\boldsymbol{\Pi}} \quad (H.4)$$

where $1/\det\boldsymbol{\Pi}$ is obtained regarding (135). Invoking both the scalar product definition in (F.1) with the definition of $\mathcal{T}_{\lambda_k}^{-1}$ in (164) while introducing the 2D-function $\boldsymbol{\Phi}_{\lambda_k}(Z) = [\Phi_{\lambda_k}^-, \Phi_{\lambda_k}^+](Z)$ achieves the following

$$\int_0^1 \left[\Phi_{\lambda_k}^-\right]^2 Z dz = \frac{\lambda_k + c_- \cos\left(\frac{\lambda_k}{c_-}\right)\sin\left(\frac{\lambda_k}{c_-}\right)}{2\lambda_k \|\tilde{\boldsymbol{\Phi}}_{\lambda_k}(Z)\| \cos^2\left(\frac{\lambda_k}{c_-}\right)}, \quad (H.5)$$

$$\int_0^1 \left[\Phi_{\lambda_k}^+\right]^2 Z dz = \left(\frac{c_+}{\beta c_-}\right)^2 \frac{\lambda_k + c_+ \cos\left(\frac{\lambda_k}{c_+}\right)\sin\left(\frac{\lambda_k}{c_+}\right)}{2\lambda_k \|\tilde{\boldsymbol{\Phi}}_{\lambda_k}(Z)\|^2 \cos^2\left(\frac{\lambda_k}{c_+}\right)}, \quad (H.6)$$

$$\int_0^1 \Phi_{\lambda_k}^-(Z)\Phi_{\lambda_k}^+(Z) dz = \frac{c_+^2\left[c_+ \tan\left(\frac{\lambda_k}{c_-}\right) - c_- \tan\left(\frac{\lambda_k}{c_+}\right)\right]}{\lambda_k \|\tilde{\boldsymbol{\Phi}}_{\lambda_k}(Z)\|^2 \beta\left(c_-^2 - c_+^2\right)}. \quad (H.7)$$

Then the $\langle \boldsymbol{\mathcal{E}}\boldsymbol{\Phi}_{\lambda_k}(Z), \boldsymbol{\Phi}_{\lambda_k}(Z)\rangle$ contributes to

$$\langle \boldsymbol{\mathcal{E}}\boldsymbol{\Phi}_{\lambda_k}(Z), \boldsymbol{\Phi}_{\lambda_k}(Z)\rangle = \mathcal{E}_{11}\int_0^1 \left[\Phi_{\lambda_k}^-(z)\right]^2 dz + \eta_2\mathcal{E}_{22}\int_0^1 \left[\Phi_{\lambda_k}^+(z)\right]^2 dz + \left[\mathcal{E}_{12} + \eta_2\mathcal{E}_{21}\right]\int_0^1 \Phi_{\lambda_k}^-(z)\Phi_{\lambda_k}^+(z) dz, \quad (H.8)$$

in the expression of $\mathcal{T}_{\lambda_k}^{-1}$ in (164). Furthermore, by definition of $\boldsymbol{\mathcal{J}}_{\lambda_k}$ in (G.6)

$$\frac{\boldsymbol{\mathcal{J}}_{\lambda_k}(s=i\lambda_k,Z)}{\lambda_k^2}=\frac{\lambda_k}{\alpha(2+\alpha)\left(1-\frac{c_-\beta}{c_+}\right)}\begin{pmatrix}-\left(\left(\frac{Z^2}{2}-Z\right)+\left(\frac{c_-}{\lambda_k}\right)^2\right)\frac{\tan\left(\frac{\lambda_k}{c_-}\right)}{c_-}\\ \left(\left(\frac{Z^2}{2}-Z\right)+\left(\frac{c_+}{\lambda_k}\right)^2\right)\frac{\tan\left(\frac{\lambda_k}{c_+}\right)}{c_+}\end{pmatrix}, \quad \text{(H.9)}$$

then $\langle\frac{\boldsymbol{\mathcal{J}}_{\lambda_k}(s=i\lambda_k,Z)}{\lambda_k^2},\boldsymbol{\Phi}_{\lambda_k}(Z)\rangle$ contributes to

$$\langle\frac{\boldsymbol{\mathcal{J}}_{\lambda_k}(s=i\lambda_k,Z)}{\lambda_k^2},\boldsymbol{\Phi}_{\lambda_k}(Z)\rangle=-\frac{\lambda_k\tan\left(\frac{\lambda_k}{c_-}\right)}{\alpha(2+\alpha)c_-\left(1-\frac{c_-\beta}{c_+}\right)}\left(\int_0^1\left[\frac{Z^2}{2}-Z\right]\Phi_{\lambda_k}^-(Z)dz+\left(\frac{c_-}{\lambda_k}\right)^2\int_0^1\Phi_{\lambda_k}^-(Z)dz\right)$$
$$\frac{\eta_2\lambda_k\tan\left(\frac{\lambda_k}{c_+}\right)}{\alpha(2+\alpha)c_+\left(1-\frac{c_-\beta}{c_+}\right)}\left(\int_0^1\left[\frac{Z^2}{2}-Z\right]\Phi_{\lambda_k}^+(Z)dz+\left(\frac{c_+}{\lambda_k}\right)^2\int_0^1\Phi_{\lambda_k}^+(Z)dz\right), \quad \text{(H.10)}$$

in $\mathcal{T}_{\lambda_k}^{-1}$ with

$$\int_0^1\left[\frac{Z^2}{2}-Z\right]\Phi_{\lambda_k}^+(Z)dz = -\frac{c_+^3}{c_-\beta\lambda_k^3\|\tilde{\boldsymbol{\Phi}}_{\lambda_k}(Z)\|}\left(\lambda_k-c_+\tan\left(\frac{\lambda_k}{c_+}\right)\right), \quad \text{(H.11)}$$

$$\int_0^1\left[\frac{Z^2}{2}-Z\right]\Phi_{\lambda_k}^-(Z)dz = \frac{c_-^2}{\lambda_k^3\|\tilde{\boldsymbol{\Phi}}_{\lambda_k}(Z)\|}\left(\lambda_k-c_-\tan\left(\frac{\lambda_k}{c_-}\right)\right), \quad \text{(H.12)}$$

$$\int_0^1\Phi_{\lambda_k}^+(Z)dz = -\frac{c_+^2}{c_-\beta\lambda_k\|\tilde{\boldsymbol{\Phi}}_{\lambda_k}(Z)\|}\tan\left(\frac{\lambda_k}{c_+}\right), \quad \text{(H.13)}$$

$$\int_0^1\Phi_{\lambda_k}^-(Z)dz = \frac{c_-}{\lambda_k\|\tilde{\boldsymbol{\Phi}}_{\lambda_k}(Z)\|}\tan\left(\frac{\lambda_k}{c_-}\right). \quad \text{(H.14)}$$

Acknowledgments

This work is under a CC-BY 4.0 licence. This work was supported by the collaborative ANRT Grant CIFRE 2019/1453 co-funded by SETOM, dedicated society of Veolia for the public drinking water service of Toulouse Métropole operating under the brand Eau de Toulouse Métropole. F. P. also warmly acknowledge discussions with Pr. E. J. Hinch the influence of who whispered and possibly silently infused this work, the familiarity of which he might recognize as a modest legacy.

The authors have no competing interests to declare.

References

[1] L. F. Menabrea, Note sur les effets du choc de l'eau dans les conduites, Mallet-Bachelier, 1858.

[2] H. Résal, Note sur les petits mouvements d'un fluide incompressible dans un tuyau élastique., Journal de Mathematiques Pures et Appliquées 2 (1876) 342–344.

[3] J. Michaud, Coups de bélier dans les conduites. Étude des moyens employés pour en atténuer les effects, Bulletin de la Société Vaudoise des Ingénieurs et des Architectes 4 (3) (1878) 4.

[4] D. Korteweg, Ueber die Fortpflanzungsgeschwindigkeit des Schalles in elastischen Röhren (On the speed of sound propagation in elastic tubes), Annalen der Physik 241 (12) (1878) 525–542.

[5] N. Joukowski, Memoirs of the imperial academy society of St.–Petersburg, Proceedings of the American Water Works Association 24 (1898) 341–424.

[6] L. Allievi, Teoria del colpo d'ariete, Atti Collegio Ing. Arch.(English translation by Halmos E.E. 1929), The Theory of Waterhammer, Tipografia della R. Accademia dei Lincei (1913).

[7] T. Pedley, The Fluid Mechanics of Large Blood Vessels, Cambridge University Press, 1980.

[8] F. N. Van De Vosse, N. Stergiopulos, Pulse wave propagation in the arterial tree, Annu. Rev. Fluid Mech. 43 (2011) 467–499.

[9] G. Kuiken, Approximate dispersion equations for thin-walled liquid-filled tubes, Appl. Sci. Res. 4 (1) (1984) 37–53.

[10] G. Kuiken, Wave propagation in a thin-walled liquid-filled initially-stressed tube, J. Fluid Mech. 141 (1984) 289–308.

[11] D. C. Wiggert, F. J. Hatfield, S. Stuckenbruck, Analysis of Liquid and Structural Transients in Piping by the Method of Characteristics, J. Fluids Eng. 109 (2) (1987) 161–165. doi:10.1115/1.3242638.

[12] D. C. Wiggert, Coupled transient flow and structural motion in liquid-filled piping systems : a survey., in: Proceedings of the ASME Pressure Vessels and Piping Conference, Chicago, 1986, pp. 86–PVP–4.

[13] A. Tijsseling, C. Lavooij, Waterhammer with fluid-structure interaction, Appl. Sci. Res. 44 (1990) 273–285.

[14] A. S. Tijsseling, Fluid-Structure Interaction in liquid-filled pipe systems: a review, J. Fluids Struct. 10 (2) (1996) 109–146. doi:10.1006/jfls.1996.0009.

[15] D. Ferras, P. Manso, A. Schleiss, D. Covas, One-Dimensional Fluid–Structure Interaction Models in Pressurized Fluid-Filled Pipes: A Review, Appl. Sci. 8 (10) (2018) 1844. doi:10.3390/app8101844.

[16] R. Skalak, An extension of the theory of waterhammer, J. Fluids Eng. Trans. ASME 78 (1956) 105–116.

[17] T. Lin, G. W. Morgan, Wave propagation through fluid contained in a cylindrical, elastic shell, J. Acoust. Soc. Am. 28 (1956) 1165–1176.

[18] A. R. D. Thorley, Pressure Transients in Hydraulic Pipelines, J. Basic Eng. 91 (3) (1969) 453–460.

[19] J. S. Walker, J. W. Phillips, Pulse Propagation in Fluid-Filled Tubes, J. Appl. Mech. 44 (1) (1977) 31–35.

[20] D. D. Budny, D. C. Wiggert, F. J. Hatfield, The Influence of Structural Damping on Internal Pressure During a Transient Pipe Flow, J. Fluids Eng. 113 (3) (1991) 424–429.

[21] A. Tijsseling, Fluid-structure interaction in case of waterhammer with cavitation, Ph.D. thesis, Delft University of Technology (1993).

[22] A. Tijsseling, Water hammer with fluid-structure interaction in thick-walled pipes, Comput. Struct. 85 (2007) 844–851. doi:10.1016/j.compstruc.2007.01.008.

[23] S. Li, B. W. Karney, G. Liu, FSI research in pipeline systems – A review of the literature, J. Fluids Struct. 57 (2015) 277–297. doi:10.1016/j.jfluidstructs.2015.06.020.

[24] E. Wylie, V. Streeter, L. Suo, Fluid Transients in Systems, Vol. 1, Prentice Hall Englewood Cliffs, NJ, 1993.

[25] M. Ghidaoui, M. Zhao, D. McInnis, D. Axworthy, A review of Water Hammer Theory and Practice, Appl. Mech. Rev. 58 (01 2005). doi:10.1115/1.1828050.

[26] A. Keramat, A. Tijsseling, Q. Hou, A. Ahmadi, Fluid–structure interaction with pipe-wall viscoelasticity during water hammer, J. Fluids Struct. 28 (2011) 434–455. doi:10.1016/j.jfluidstructs.2011.11.001.

[27] M. H. Chaudhry, Applied Hydraulic Transients, 3rd Edition, Springer-Verlag, 2014. doi:10.1007/978-1-4614-8538-4.

[28] A. Ghodhbani, E. Haj Taïeb, A four-equation friction model for water hammer calculation in quasi-rigid pipelines, Int. J. Press. Vessel. Pip. 151 (2017) 54–62.

[29] L. Zhang, A. Tijsseling, A. Vardy, FSI analysis of liquid-filled pipes, J. Sound Vib. 224 (1) (1999) 69–99.

[30] Q. S. Li, K. Yang, L. Zhang, N. Zhang, Frequency domain analysis of fluid–structure interaction in liquid-filled pipe systems by transfer matrix method, Int. J. Mech. Sci. 44 (10) (2002) 2067–2087. doi:10.1016/S0020-7403(02)00170-4.

[31] H. K. Aliabadi, A. Ahmadi, A. Keramat, Frequency response of water hammer with fluid-structure interaction in a viscoelastic pipe, Mech. Syst. Signal Process. 144 (2020) 106848. doi:10.1016/j.ymssp.2020.106848.

[32] Q. Li, K. Yang, L. Zhang, Analytical Solution for Fluid-Structure Interaction in Liquid-Filled Pipes Subjected to Impact-Induced Water Hammer, J. Eng. Mech. - ASCE 129 (2003) 1408–1417. doi:10.1061/(ASCE)0733-9399(2003)129:12(1408).

[33] A. Bayle, F. Plouraboué, Spectral properties of Fluid Structure Interaction pressure/stress waves in liquid filled pipe, Wave Motion 116 (2023) 103081.

[34] P. Flaud, D. Geiger, C. Oddou, D. Quemada, Ecoulements pulsés dans les tuyaux visco-élastiques. Application à l'étude de la circulation sanguine., J. de Physique 35 (1974) 869–882.

[35] S. I. Rubinow, J. B. Keller, Wave propagation in a viscoelastic tube containing a viscous fluid, J. Fluid Mech. 88 (1) (1978) 181–203. doi:10.1017/S0022112078002049.

[36] W. Zielke, Frequency-Dependent Friction in Transient Pipe Flow, J. Basic Eng. 90 (1) (1968) 109–115.

[37] A. Bergant, A. Simpson, J. Vìtkovsky, Developments in unsteady pipe flow friction modelling, J. Hydraul. Res. 39 (3) (2001) 249–257.

[38] A. Adamkowski, M. Lewandowski, Experimental Examination of Unsteady Friction Models for Transient Pipe Flow Simulation, J. Fluids Eng. 128 (11 2006). doi:10.1115/1.2354521.

[39] D. Wood, J. Funk, A boundary-layer theory for transient viscous losses in turbulent flow, J Basic Eng, Trans ASME 92 (1970) 865–873.

[40] A. E. Vardy, K. Hwang, A characteristics model of transient friction in pipes., J. Hydraul. Res. 29 (5) (1991) 669–684.

[41] C. Mei, H. Jing, Pressure and wall shear stress in blood hammer – Analytical theory, Math. Biosci. 280 (2016) 62–70.

[42] C. C. Mei, H. Jing, Effects of thin plaque on blood hammer—An asymptotic theory, Eur. J. Mech. B Fluids 69 (2018) 62–75. doi:10.1016/j.euromechflu.2018.01.004.

[43] A. Corli, I. Gasser, M. Lukacova-Medvid'Ova, A. Roggensack, U. Teschke, A multiscale approach to liquid flows in pipes I: The single pipe, Appl. Math. Comput. 219 (3) (2012) 856–874.

[44] J. Lighthill, Waves in fluids, Cambridge university press, 2001.

[45] F. Gaultier, J. Gilbert, J. Dalmont, R. Picó, Wave propagation in a fluid filled rubber tube: Theoretical and experimental results for Korteweg's wave, Acta Acust. United Ac. 93 (2007) 333–344.

[46] H. Lamb, On the velocity of sound in a tube, as affected by the elastic of the walls., Memoirs of the Manchester Literary and Philosophical Society, Manchester, (UK) 42 (9) (1898) 1–16.

[47] E. L. Holmboe, W. T. Rouleau, The Effect of Viscous Shear on Transients in Liquid Lines, J. Basic Eng. 89 (1) (1967) 174–180.

[48] C. Boutin, K. Viverge, Generalized plate model for highly contrasted laminates, Eur. J. Mech. A/Solids 55 (2016) 149–166.

[49] E. J. Hinch, Perturbation Methods, Cambridge Texts in Applied Mathematics, Cambridge University Press, 1991. doi:10.1017/CBO9781139172189.

[50] E. Yao, G. Kember, D. Hansen, Water Hammer Analysis and Parameter Estimation in Polymer Pipes with Weak Strain–Rate Feedback, J. Eng. Mech. 142 (8) (2016) 04016052.

[51] J. F. Harvey, Theory and Design of Modern Pressure Vessels, Van Nostrand Reinhold, 1974.

[52] A. Vardy, J. Brown, Transient turbulent friction in smooth pipe flows, J. Sound Vib. 259 (5) (2003) 1011–1036.

[53] B. Brunone, U. Golia, M. Greco, Modelling of fast transients by numerical methods, in: Proceedings of the 9th International Conference on Hydraulic Transients with Water Column Separation, Valencia, Spain, 1991, pp. 273–281.

[54] A. Vardy, J. Brown, Transient turbulent friction in fully rough pipe flows, J. Sound Vib. 270 (1) (2004) 233–257.

[55] K. Urbanowicz, Fast and accurate modelling of frictional transient pipe flow, Z Angew Math Mech 98 (02 2018).

[56] P. Puntorieri, G. Barbaro, N. Martins, D. Covas, V. Fiamma, Hydraulic Transient Experimental Study in a Copper Pipe, in: Proceedings of the Multiphase Flow 2017, 2017, pp. 27–33. doi:10.2495/MPF170041.

[57] N. Duraiswamy, R. T. Schoephoerster, M. R. Moreno, J. E. Moore, Jr., Stented artery flow patterns and their effects on the artery wall, Annu. Rev. Fluid Mech. 39 (2007) 357–382.

[58] W. Bürmann, Longitudinal motion of coaxial pipes due to water hammer, 3R International 19 (1) (1980) 398 – 404.